

**A REMOTELY POWERED ELECTROLYTIC ACTUATOR WITH DOSE
CONTROL FOR IMPLANTABLE DRUG DELIVERY**

by

Ying Yi

A THESIS SUBMITTED IN PARTIAL FULFILLMENT OF
THE REQUIREMENTS FOR THE DEGREE OF

DOCTOR OF PHILOSOPHY

in

COLLEGE OF GRADUATE STUDIES

(Electrical Engineering)

THE UNIVERSITY OF BRITISH COLUMBIA

(Okanagan)

July 2016

© Ying Yi, 2016

The undersigned certify that they have read, and recommend to the College of Graduate Studies for acceptance, a thesis entitled:

A Remotely Powered Electrolytic Actuator with Dose Control for Implantable Drug Delivery

Submitted by Ying Yi in partial fulfillment of the requirements of

The degree of Doctor of Philosophy

Dr. Ian Foulds, School of Engineering

Supervisor, Professor (please print name and faculty/school above the line)

Dr. Mina Hoorfar, School of Engineering

Supervisory Committee Member, Professor (please print name and faculty/school in the line above)

Dr. Keekyoung Kim, School of Engineering

Supervisory Committee Member, Professor (please print name and faculty/school in the line above)

Dr. Boris Stoeber, Faculty of Applied Science

University Examiner, Professor (please print name and faculty/school in the line above)

Dr. Carolyn Ren, University of Waterloo

External Examiner, Professor (please print name and university in the line above)

July 8, 2016

(Date submitted to Grad Studies)

Abstract

“On demand” implantable drug delivery systems can provide optimized treatments, due to their ability to provide targeted, flexible and precise dose release. This dissertation focuses on remotely powering an implantable drug delivery system and providing a high degree of control over the released dose, addressing two important issues for “on demand” drug delivery: effective actuation stimulus and controllable dose release mechanism. This is accomplished by integration of a resonance-based wireless power transfer system, a constant voltage control circuit and an electrolytic pump. A novel actuation mechanism that is based on a cyclical actuation mode is introduced, implementing a solid drug in reservoir approach. The solid drug is partly dissolved during the initial stage, when a voltage is applied to the electrolytic pump, an electrolytic reaction occurs and the induced gas expansion drives the drug solution outwards. When the power turns off, the electrolysis bubble recombines and pressure decreases in the pump, which draws body fluids into the drug reservoir to dissolve more of the remaining solid drug. Power is repeatedly turned on and off to form a reproducible drug solution. A catalytic reformer enables the combination of the electrolytic pump and solid drug in reservoir approach as it significantly increases the electrolysis-bubble recombination rate, and is capable of fully replenishing the drug reservoir. Resonance-based wireless power transfer technology performs as the power source and a control circuit maintains a constant voltage for the actuator. Upon the application of an external alternating magnetic field, the electrolytic actuator is powered by a constant voltage regardless of movements of the device within an effective range of shift and rotation. This in turn contributes to a predictable dose release rate and greater flexibility in the positioning of external powering coils. Moreover, a thermo-responsive valve using “Poly-N-Isopropylacrylamide” hydrogel is

implemented in order to avoid the negative effect of drug diffusion. It allows actively controlled drug delivery and valving mechanism under the same input power signal. We have conducted proof-of-concept drug delivery studies using solvent blue 38 as the drug substitute, and the experimental results indicate the stability, feasibility and controllability of our system.

Preface

This dissertation is based on the works I have conducted under the supervision of Dr. Ian Foulds. I fabricated the majority of the devices, set up experiments, tested apparatus, recorded experimental data, and wrote the manuscripts for publications. Almost all of the articles are co-authored with Mr. Ulrich Buttner who provided valuable comments and technical support for some device fabrications. For the publications related to Chapter 2, Mr. Armando Carreno helped me design the electrolysis electrode; Mr. David Conchouso gave excellent comments on the electrolytic pump's assembly process. For the publications related to Chapter 3, Mr. Amir Zaher helped me fabricate the valve's micro-channel, and Dr. Omar Yassine fabricated the hydrogel materials. Dr. Jurgen Kosel helped me develop my ideas and reviewed the articles related to Chapters 3-4. The Chapters of this dissertation come from the following journals and conference papers.

Publications related to Chapter 2

- [C1]. **Yi, Y.**, Buttner, U. and Foulds, I. G. (2013). Towards an implantable pulsed mode electrolytic drug delivery system. *In 17th International Conference on Miniaturized Systems for Chemistry and Life Sciences (μ TAS)*, 527-529.
- [J1]. **Yi, Y.**, Buttner, U., Carreno, A. A., Conchouso, D., and Foulds, I. G. (2015). A pulsed mode electrolytic drug delivery device. *Journal of Micromechanics and Microengineering*, 25(10), 105011.
- [J2]. **Yi, Y.**, Buttner, U., and Foulds, I. G. (2015). A cyclically actuated electrolytic drug delivery device. *Lab on a Chip*, 15(17), 3540-3548.

Publications related to Chapter 3

[C2]. Yi, Y., Zaher, A., Yassine, O., Buttner, U., Kosel, J., and Foulds, I. G. (2015). Electromagnetically powered electrolytic pump and thermo-responsive valve for drug delivery. In *10th IEEE International Conference on Nano/Micro Engineered and Molecular Systems (NEMS)*, 5-8. **(Best Paper in Micro/Nano Fluidics Award)**.

[J3]. Yi, Y., Zaher, A., Yassine, O., Kosel, J., and Foulds, I. G. (2015). A remotely operated drug delivery system with an electrolytic pump and a thermo-responsive valve. *Biomicrofluidics*, 9(5), 052608.

Publications related to Chapter 4

[J4]. Yi, Y., Buttner, U., Fan, Y., and Foulds, I. G. (2015). Design and optimization of a 3-coil resonance-based wireless power transfer system for biomedical implants. *International Journal of Circuit Theory and Applications*, 43(10), 1379–1390.

[J5]. Yi, Y., Kosel, J., and Foulds, I. G. (2016). A remotely powered electrolytic actuator with dose control for implantable drug delivery. Submitted to *IEEE Transactions on Biomedical Circuits and Systems*.

Table of Contents

Abstract.....	ii
Preface.....	iv
Table of Contents	vi
List of Tables.....	ix
List of Figures.....	x
List of Abbreviations.....	xvi
Acknowledgements	xviii
Dedication	xx
Chapter 1 Introduction.....	1
1.1 Background and motivation	1
1.2 SDR approach applied in drug delivery systems.....	7
1.3 Literature review of micro-pump for drug delivery	12
1.3.1 Reciprocating displacement micro-pump.....	13
1.3.2 Non-reciprocating type micro-pumps	20
1.4 Introduction to microvalve	26
1.5 Introduction to WPT.....	30
1.5.1 Inductive-coupling type	31
1.5.2 Resonance-based type	32
1.6 Biological issues.....	34
1.7 Dissertation organization and contributions	37
Chapter 2 Cyclically Actuated Electrolytic Actuator	39

2.1 Electrolytic pump	40
2.1.1 Electrode design and fabrication	40
2.1.2 The pump's design	44
2.1.3 The pump's fabrication and performance.....	47
2.2 Catalytic reformer.....	54
2.2.1 Nickel foam scaffold.....	55
2.2.2 Carbon fiber scaffold.....	63
2.3 Cyclical actuation mode	69
2.3.1 Cyclical operation performance	69
2.3.2 Cumulative drug release.....	72
2.4 Summary	76
Chapter 3 Remotely Operated Thermo-responsive Valve and the Actuator	78
3.1 PNIPAM valve.....	78
3.2 Remote operation	82
3.3 Summary	91
Chapter 4 Optimization of a 3-Coil R-WPT System with Dose Control Approach for Drug Delivery	93
4.1 Coils' design model.....	94
4.1.1 Wire property	94
4.1.2 Self-inductance and parasitic capacitance.....	97
4.1.3 Q -factor calculation.....	98
4.2 Power transfer efficiency evaluation	101
4.2.1 Power transfer models.....	101
4.2.2 Design optimization	104
4.2.3 Experimental setup and measurements for PTE.....	105

4.3 Remotely operated drug delivery with dose control.....	110
4.3.1 Wireless system architecture	110
4.3.2 Liquid drug delivery performance evaluation	114
4.3.3 Cyclically operated solid drug delivery system	119
4.4 Summary	123
Chapter 5 Conclusion	125
5.1 Discussion and summary	125
5.2 Contributions for Ph.D Program (2012 May-2016 June)	128
5.3 Future directions	130
5.4 Final conclusion	132
Bibliography	134

List of Tables

Table 1.1 Reciprocating displacement micropumps	14
Table1.2: Non-reciprocating type micro-pumps.	21
Table 4.1 AWG LITZ wire property.....	99
Table 4.2 Coils' physical specification by measurements [J4].	104
Table 4.3 Comparison with previously reported works [J4].....	109

List of Figures

Figure 1.1 Illustration depicting therapeutic window and different releasing profiles [J2].....	2
Figure 1.2 Taxonomy of drug delivery outlining the major content in subsequent subchapters. Blue boxes indicate the areas of concentration in this dissertation..	7
Figure 1.3 Prototype of <i>IntelliDrug</i> device and its operation principle [17] [†]	10
Figure 1.4 (a) Conceptual illustration of the intraocular drug delivery device sutured to the posterior eyeball; (b, c) Its operation principle [65] [†]	12
Figure 1.5 Cross section of an electrostatic micro pump.....	15
Figure 1.6 Piezoelectric effects.....	16
Figure 1.7 Cross section of an electromagnetic micro pump.....	17
Figure 1.8 Cross section of a thermopneumatic micro-pump.....	18
Figure 1.9 Cross section of a SMA micro-pump.	19
Figure 1.10 Schematic illustration of a MHD micro pump.	22
Figure 1.11A schematic diagram of the osmotic type micro-pump for drug delivery application. (a) Operation principle of a single compartment pump. (b) Operation principle of a two-compartment pump.....	23
Figure 1.12 Cross section of the electrochemical micro-pump illustrating electrolysis-generated bubble pumping the liquid directly.....	25
Figure 1.13 Illustration of thermos-responsive behavior of PNIPAM [154] [†]	28
Figure 1.14 The inductive coupling based circuit model.....	30
Figure 1.15 The resonance-based circuit model of added capacitors.	32
Figure 2.1 Flow diagram of electrodes fabrication process [J1].....	41
Figure 2.2 Photograph of Ti/Pt electrode design: (a) the electrodes fabricated on silicon with Nafion coating; (b) microscope of the interdigitated electrode layout showing	

element width and spacing [J1].....	42
Figure 2.3 Exploded diagram of the electrolytic actuator based drug delivery system including: a) the actuator with major components. b) assembled drug delivery device (reproduced from [J1]).....	44
Figure 2.4 Schematic illustration of the electrolytic pump based drug delivery device and its cyclic actuation mechanism (reproduced from [J1]).....	45
Figure 2.5 Photograph of the experimental setup and structure of electrolytic pump [C1]. .	47
Figure 2.6 Electrolytic pump's I - V property [J2].....	49
Figure 2.7 Electrolytic pump flow rate vs. applied power for both Nafion coated and uncoated electrodes [C1].....	50
Figure 2.8 Periodical pumping pulses show behaviors of electrolytic bubble and gas recombination [C1].	51
Figure 2.9 The dose of released drug per pulse under the applied power of 1mW [C1].	53
Figure 2.10 Microscope of Pt-coated nickel foam fabricated by (a) sputtering, (b) electroplating [J1].	55
Figure 2.11 Schematic illustration of the assemble process of the electrolytic pump.	56
Figure 2.12 Photograph of the experimental apparatus and structure of electrolytic pump: (a) the assembled electrolytic pump for experimental measurements; (b) the photo of laser drilled-drug reservoir from PMMA board; (c) photograph of pumping chamber with a catalytic reformer and Nafion coated electrodes [J1].....	57
Figure 2.13 Pump efficiency comparisons between three different pump versions [J1].	59
Figure 2.14 Flow rates vs. applied power for three different pump versions [J1].	60
Figure 2.15 SEM images of the Pt coated Nickel mesh surface, (a)-(b) depicts the sputtered Pt mesh before and after used. (c)-(d) shows the electroplated Pt mesh before used and after used. Catalytic reformers were used for 20 actuation cycles with each actuation period of 30 seconds under a power of 4 mW [J1].	61

Figure 2.16 Profiles of bubble generation and recombination for three different pump versions; power of 3.7 mW was applied [J1].	62
Figure 2.17 Illustration and photographs of our proposed electrolytic pump: (a) Exploded view of the device showing its major components; (b) Test fixture photo; (c) Drug reservoir cut from PMMA board; (d) Photo of assembled electrolysis actuator including Pt coated carbon fiber mesh; (e) Layout of Nafion coated Pt/Ti electrodes. The scale bars are 5 mm [J2].	64
Figure 2.18 (a) Top SEM view of overall Pt coated carbon fiber mesh, showing the magnified region of the edge from (b) the top view and (c) a cross-sectional view, illustrating the details of the porous structure [J2].	65
Figure 2.19 Power controlled flow rates for the electrolytic pump with and without catalytic reformer ($Mean \pm SE, n=3$) [J2].	66
Figure 2.20 Real-time membrane displacement of the electrolytic pump with and without catalytic reformers under the same experimental conditions, power of 4 mW was applied and then removed [J2].	67
Figure 2.21 SEM images of the Pt coated carbon fiber surface after used. Catalytic reformers were used for 20 actuation cycles with each actuation period of half minute under a power of 2.4 mW [J2].	68
Figure 2.22 Cyclical displacement operated with different applied power indicating stable behaviors of electrolysis bubble generation and recombination [J2].	70
Figure 2.23 Membrane displacement operated with different actuation frequencies using a constant power of 2.4 mW [J2].	71
Figure 2.24 Experimental apparatus of drug delivery, side view of device depicts release of solvent blue into external solution upon electrolysis bubble actuation [J2].	73
Figure 2.25 Intermittent release of solvent blue 38 from the pump to the external reservoir by applied power of 4 mW. After each pumping a period of	

delivery is followed with non-actuation mode. Released solvent blue 38 was cumulated by a series of actuations [J2].	74
Figure 3.1 PNIPAm hydrogel: (a) at room temperature; (b) at LCST [C2].	80
Figure 3.2 Straight PNIPAm polymer valve [C2].	81
Figure 3.3 Throughput of the valve under different magnetic fields to demonstrate the corresponding opening time [C2].	82
Figure 3.4 Exploded view of the device showing its major components [J3].	83
Figure 3.5 Schematic illustration of the SDR based device and its cyclic operation [J3].	84
Figure 3.6 (a) photographs of the experimental apparatus and the prototypes of the major components: (b) assembled electrolytic pump; (c) image of Nafion coated Pt/Ti electrodes; (d) sputtered platinum coated carbon fiber mesh; (e) inductive coil; (f) the PNIPAM valve mixed with iron micro-particles [J3].	85
Figure 3.7 Pumping profile under an electromagnetic field of 40.5 mT when the thermo-responsive valve was used in combination with a pump with three catalytic reformer elements. The insets illustrate the states of the valve at different time points and the corresponding temperatures. Black particles are the iron micro-particles. Scale bars are 3 mm [J3].	88
Figure 3.8 Cyclic liquid displacement of the dye when a device with a pump, three catalytic reformer elements and a PNIPAM valve is operated with an electromagnetic field of 40.5 mT that is periodically turned on and off [J3].	90
Figure 4.1 Coils' cross sections. D_{in} : inner conductor loop, D_{out} : outer conductor loop, OD : outer diameter. (a) Typically wound Litz wire coil with multi-layer and multi-turn structure. (b) Cross sections of single turn with multi-strand wires [J4].	95
Figure 4.2 Proposed structures of secondary coil and load coil [J4].	96
Figure 4.3 Tendency of self-resonance frequency and Q -factor versus the number of the turns, the operating frequency $f=6.7$ MHz [J4].	100

Figure 4.4 Circuit model of the 3-coil R-WPT system [J4].....	102
Figure 4.5 Implant coils' dimensions using AWG Litz wire [J4].	103
Figure 4.6 Q -factors' curve versus operating frequency [J4].....	105
Figure 4.7 PTE versus the Q_3 and d_{23} for the 3-coil system; $Q_2=173$, $Q_4=112$, $R_L=100 \Omega$, $r_p=15\text{mm}$, $r_s=17.5\text{mm}$ [J4].	106
Figure 4.8 (a) The experimental setup for the three-coil WPT system. (b) The measurement results of the primary coil input voltage and load coil output voltage, $d_{23}=20 \text{ mm}$ [J4].	107
Figure 4.9 PTE measurement comparisons versus the coupling distance [J4].	108
Figure 4.10 Resonance-based wireless power transfer system with the constant voltage control circuit: (a) the corresponding circuit model; (b) the prototype of the control unit. V_s is the voltage output of the AC power source, R_s is the output impedance, R_{rec} is the resistance of the receiver, C_2 - C_4 denote capacitors, and L_2 - L_4 represent coils [J5].	111
Figure 4.11 System performance with and without Zener diode for voltage control [J5].	112
Figure 4.12 The performance comparison of power delivered to the load using different load resistances [J5].	113
Figure 4.13 The power delivered to different loads over different distances [J5].	114
Figure 4.14 Photograph of the experimental apparatus with system components: (a) the wirelessly powered drug delivery system with a glass capillary for output measurements; (b) The interdigitated electrodes with Nafion coating; (c) the catalytic reformer [J5].	115
Figure 4.15 The flow rate of the electrolytic pump versus the transfer distance for different load resistance values [J5].....	116
Figure 4.16 Periodic pumping pulses of the pump working at different conditions (distance and rotation), showing the impact of the load resistance on the flow rate [J5].	118

Figure 4.17 Experimental apparatus for solid drug delivery, depicting the release of solvent blue 38 into the external liquid upon the electrolytic actuation [J5].....	120
Figure 4.18 Microscope images of one cycle of drug delivery process under “power on and off” operation, illustrating the reversibility of the fluid upon the PDMS membrane’s deflection [J5].....	121
Figure 4.19 The dose of released drug per actuation for different distances between the transmitter and receiver coils as well as different rotation angles [J5].	122

List of Abbreviations

AC	alternating current
bFGF	basic fibroblast growth factor
BCNU	bis-chloroethylnitrosourea
BoE	buffered oxide etched
BRMs	biological response modifiers
BSA	bovine serum albumin
CMV	cytomegalovirus
DI	deionized
DME	diabetic macular edema
DTX	docetaxel
EAP	electro-active polymer
EO	electroosmotic
ESR	effective series resistance
EW	electrowetting
FBGCs	foreign body giant cells
H ₂	hydrogen
ISM	industrial, scientific and medical
IMDs	implantable medical devices
KPS	potassium persulfate
LCST	lower critical solution temperature
LDR	liquid drug in reservoir
LIGA	lithography, electroplating, and molding
MEMS	micro-electro-mechanical systems

MHD	magnetohydrodynamic
Ni	nickel
NIPAAM	N-Isopropylacrylamide
O ₂	oxygen
PBS	phosphate buffered saline
PCB	printed circuit boards
PDL	power delivered to the load
PDMS	polydimethylsiloxane
PLGA	Poly-lactic-co-glycolic acid
PMMA	polymethylmethacrylate
PNIPAM	poly-N-Isopropylacrylamide
PSC	printed spiral coils
Pt	platinum
PTE	power transfer efficiency
PVA	polyvinyl alcohol
PZT	lead zirconate titanate
R-WPT	resonance-based wireless power transfer
SDR	solid drug in reservoir
SEM	scanning electron microscope
SMA	shape memory alloy
TEMED	tetramethylethylenediamine
TiNi	titanium nickel
UV	ultraviolet
WPT	wireless power transfer
VEGF	vascular endothelial growth factor

Acknowledgements

First and foremost, I would like to give my whole-hearted gratitude to my supervisor, Prof. Ian Foulds, I take this opportunity to express my sincere gratefulness to him for his constant support and encouragement during my PhD studies. I am very fortunate to have met such a nice supervisor because the completion of my PhD program in the University of British Columbia (Okanagan campus) would be impossible without his proper guidance, striving mind, invaluable knowledge, and comments. I must express my gratitude to my committee members, Prof. Mina Hoorfar and Prof. Keekyoung Kim, for their valuable time on reading my dissertation and giving me insightful comments. I would also like to express my thanks to Prof. Boris Stoeber and Prof. Carolyn Ren for the time and attention invested in reviewing my dissertation.

Deep appreciation goes to King Abdullah University of Science and Technology for its generous financial support and excellent graduate education. I never forget the professors and friends I met in such a beautiful university, Prof. Mohamed Slim Alouini, Prof. Christian Claudel, Prof. Khaled Nabil Salama, Prof. Atif Shamim, Dr. Jian Sun, Dr. Bodong Li, Dr. Fuquan Li, Dr. Hao Wang, Dr. Omar Yassine, Amir Zaher, Ahmed Alfadhel, and Chengcheng Tang. I am indebted to these people for their unconditional support on various occasions during my study in Saudi Arabia. I cordially thank all of my past group members, Armando Arpys, David Conchouso, David Castro, Dr. Yiqiang Fan, and Dr. Huawei Li, who helped me a lot on many aspects of my research. Special thanks go to Prof. Kosel Jurgen and Ulrich Buttner, who cooperated with me on some primary research works, as their vigorous ideas and valuable suggestions indeed inspired my work.

Finally, I owe my greatest thankfulness to my parents, my wife, and my daughter, who are always lifting my spirit and keeping me motivated through the hard and stressful times, for their whole-hearted love and sincere encouragement.

Dedication

Dedicated to my parents

Chapter 1 Introduction

1.1 Background and Motivation

Currently, drug therapies are playing an important role for variety of biomedical applications and disease treatments. Conventional modes of drug administration including oral ingestions, eye drops, transdermal delivery and intravenous injections have been widely used [1], however, these conventional approaches have limitations in effectively delivering some special drug and new pharmaceutical agents, for example, application of protein and DNA based drugs is generally not feasible by oral ingestions [1]. In addition, conventional treatments require large overdoses to reach therapeutic levels, because more than 95% of the applied medication is obstructed by physiological barriers [2]. Some unnecessary drug ingredients, such as flavoring agents, binders, and carriers, can further reduce the medication efficiency. Chronic diseases, such as diabetes, usually require frequent injections, which lead to discomfort and trauma to patients. In case of a potent drug, dosing must be precisely controlled within an effective therapeutic concentration range, which is difficult to achieve with conventional drug delivery approaches; because it brings high drug concentration above the effective therapeutic range at the onset of release, frequently leading to overdose induced side effects, while it drops to inefficient levels overtime [3].

In contrast to conventional drug delivery methods, recently developed implantable drug delivery systems are very versatile, providing efficient, targeted and controlled dose release, in particular, showing advantages for treating chronic diseases, for example brain tumors [4] and proliferative diabetic retinopathy [5]. Once the device is implanted, additional surgical operations are not required for a long treatment period (months or even years) [6], thereby reducing medical cost

and patients' discomfort. Implantable drug delivery can optimize pharmacological effects and minimize the negative influence at the disease site, because it maintains a desired drug concentration within the therapeutic window, and reduces the possibility of concentration-induced toxicity, and improves the therapy's effectiveness [7]. The delivery methods are generally classified as two types according to their release kinetics: sustained release and “on-demand” release, the corresponding concentration profiles are illustrated in Figure 1.1, showing significant difference as that of the released drug depending on the conventional mechanism.

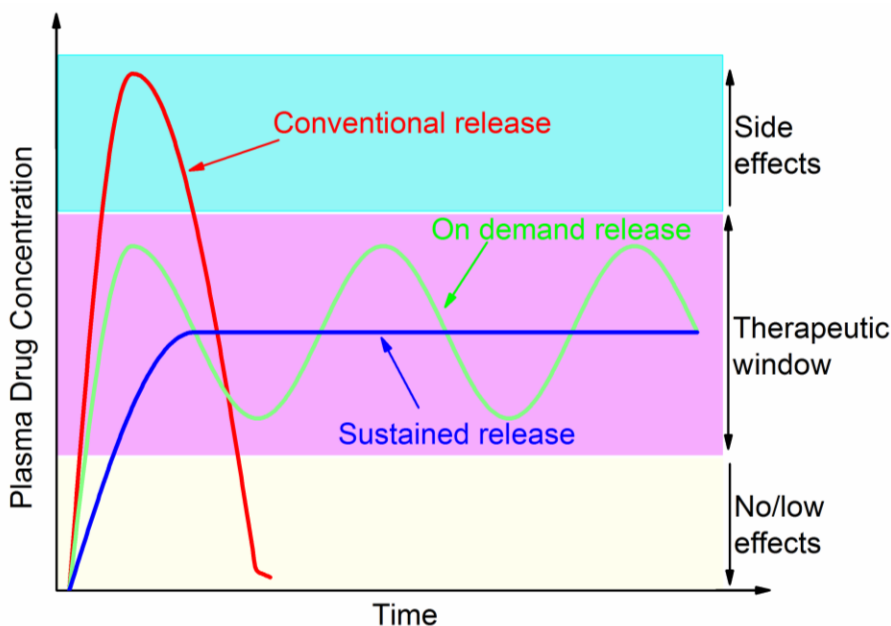


Figure 1.1 Illustration depicting therapeutic window and different releasing profiles [J2].

Sustained mechanisms can maintain a stable drug concentration within the therapeutic range, but they require constant actuation for delivering the drug continuously. Sustained release based devices usually contain a fixed volume of drug, and the release rate is constant with time. As the previous studies describe, many sustained release based implants are implemented using polymer materials with biodegradability [8], sensitivity to pH or temperature [9], and other characteristics

[10]; the delivery carriers include microspheres [11, 12], microcapsules [13, 14] and hydrogels [15, 16]; the actuation mainly comes from diffusion, absorption or osmotic pressure. For example, an osmotic pump is capable of providing continuous and constant drug infusion [17]. These devices are “passively controlled”, showing a drawback that once the device is implanted, changing the drug concentration level or the release rate is difficult; consequently, dosing is not flexible, and cannot be easily varied based on changing clinical needs. Though Cai *et al.* developed a drug release “switch on and switch off” model by changing the direction of external magnetic field, the release of DNA and vitamin B2 is still based on slow osmotic flow through a porous membrane [18], resulting in a low controllability.

Over the past two decades, micro-electro-mechanical systems (MEMS) technologies have been developed that are able to offer a variety of feasible applications for biological analysis chips [19], tissue engineering [20], and controlled drug delivery [21]. MEMS fabrication based electrolytic pump has been proven very effective for “actively” controlling implantable drug delivery by an external power stimulus [3]. The actuation of such devices comes from bubbles produced during electrolysis. Meng *et al.* optimized the design of their electrolytic pump [22] and used it for delivering liquid drug to the eyeball for treating chronic ocular disease [23]. Further, DI water was adopted as an electrolyte which can be electrolyzed into oxygen and hydrogen, the generated gases deformed an elastic membrane for delivering the anti-cancer drugs in a mouse study [24]. However, all of these devices adopted the liquid drug in reservoir (LDR) approach, which has limited long-term application due to the limited storage capacity.

Besides the limited capacity for storing drug, another issue needs to be addressed for long-term

drug delivery applications is drug diffusion. Undesired drug diffusion occurs at the outlet of the implant if the drug delivery device does not employ a valve. Therefore, adding a valve to the drug delivery device will greatly extend its functionality. Previous works have shown the opening and closing of a passive valve by a pressure difference between inside and outside of the drug delivery device, its purpose is to avoid the drug liquid dilution caused by the reverse flow from the external liquid environment [24, 25]. Unlike passive valves, active valves are controllable and capable of offering advanced functions and applications, such as drug delivery [3, 26]. In this dissertation, a phase change based valve using poly-N-Isopropylacrylamide (PNIPAM) hydrogel is proposed to prevent the drug diffusion due to its simple operation and fabrication process. PNIPAM valve can be remotely operated by inductive heating [27, 28] as PNIPAM hydrogel is a thermo-responsive substance that changes in volume by expelling or absorbing water molecules, depending on whether it is above or below a designed lower critical solution temperature (LCST), respectively [29]. It allows the body liquid from outside the device to refill the drug reservoir before the valve is fully sealed, which is required for our drug delivery system.

“On demand” controlled implantable drug delivery devices commonly provide a pulsatile dose release, which contribute to a pulsed-like drug concentration profile [6, 30]. Therefore, a suitable dose control approach is needed in order to constrain the drug concentration within the therapeutic window and maximize the therapeutic efficacy. More recently, “smart integrated microsystem technologies” have been proposed and indicated the development trend of future implantable drug delivery devices [1]. Such advanced drug delivery systems may integrate a micro-actuator with a biosensor [31, 32] or wireless control unit [33, 34] or combinations of the

above [35-37] in order to monitor the physiological conditions in a patient's body [38] and release an appropriate amount of drug in accordance with the signals detected [39]. For example, a telemetry-controlled microchip device that consisted of a wireless communication hardware, power supply, printed circuit boards (PCB) and a drug filled multi-reservoir array was implanted into the subcutaneous tissue of a dog, and remotely programmed to initiate a pulsatile release of the polypeptide leuprolide over 6 months [6]. However, this versatility comes at a cost of large size and high complexity.

Some attempts using efficient microfabrication techniques and simple operation schemes towards highly functional drug delivery systems exist [40], for example, a magnetic membrane is designed to achieve “on-demand” drug delivery upon the actuation of an external magnetic field [30, 41]. The drug dose released is directly related to the strength of the magnetic field and the duration for which the “magnetic field is turned on”. However, exposure to a strong magnetic field over an extended period may harm human health [42, 43]. Inductive coil-based wireless power transfer technology has superior power efficiency [44] than the purely magnetic force, which was proposed for powering ocular drug delivery devices [22, 34], however, their delivery kinetics is sensitive to the operation distance and rotation of the implants. Additionally, the power delivered is limited, otherwise, it may bring serious heat dissipation, resulting in tissue injury. Hence, besides the device's complexity and fabrication cost, the limitations including possible movements and power consumption of the actuator need to be addressed in novel implantable drug delivery systems.

The main task of this dissertation is to design an “on demand” drug delivery system that is easy

to fabricate and flexible to operate, combining a resonance-based wireless power transfer (R-WPT) system, which provides a high power transfer efficiency (PTE), with the lower power consumption of an electrolytic pump. The geometry of the inductive coils is carefully designed, the dimension of the receiver coil is 0.5 mm in thickness and 3 cm in diameter. It not only saves a considerable amount of space, but also is suitable to be placed under the skin or other flat epidermal organs. This system can release various dosages of drug by intermittent delivery and achieve a pulsed profile of concentration based on the release rate and time.

In order to mitigate fluctuations of the voltage received caused by different thicknesses of the tissues of different people and the movements of the wrists and joints, we further add a voltage control circuit to regulate the supply voltage of the actuator. This ensures well-defined drug release rate for a wide range of movements including shifts and rotations between transmitter and receiver. With the dose control mechanism, the induced drug concentration can be sustained within the therapeutic window and optimize the therapy efficacy. Moreover, different flow rates can be obtained to meet different application needs by changing the resistance of the load. Therefore, the released dose can be calculated by multiplying the predictable flow rate and actuation period. This kind of “on demand” release with dose control is suitable for both LDR as well as solid drug in reservoir (SDR) drug delivery systems; and it is well suited for those circumstances when the physiological conditions occasionally change, requiring varying dose during use.

The rest of this chapter is organized as indicated in Fig. 1.2; Subchapter 1.2 compares different drug storage approaches including the LDR and the SDR, and this dissertation will concentrate

on the operation mechanism of the SDR delivery system in terms of its feasibility and controllability. Subchapter 1.3 reviews the reported studies about various micro-actuators, and the electrolytic pump is adopted in this dissertation. Subchapter 1.4 introduces micro-valves, and focuses on a soft material valve called PNIPAM hydrogel. As an external power stimulus, fundamental of WPT is briefly demonstrated in subchapter 1.5. Subchapter 1.6 provides some solutions to the biological issues, like biofouling, from the literatures. Finally, the outline and contributions of the following chapters are given in subchapter 1.7.

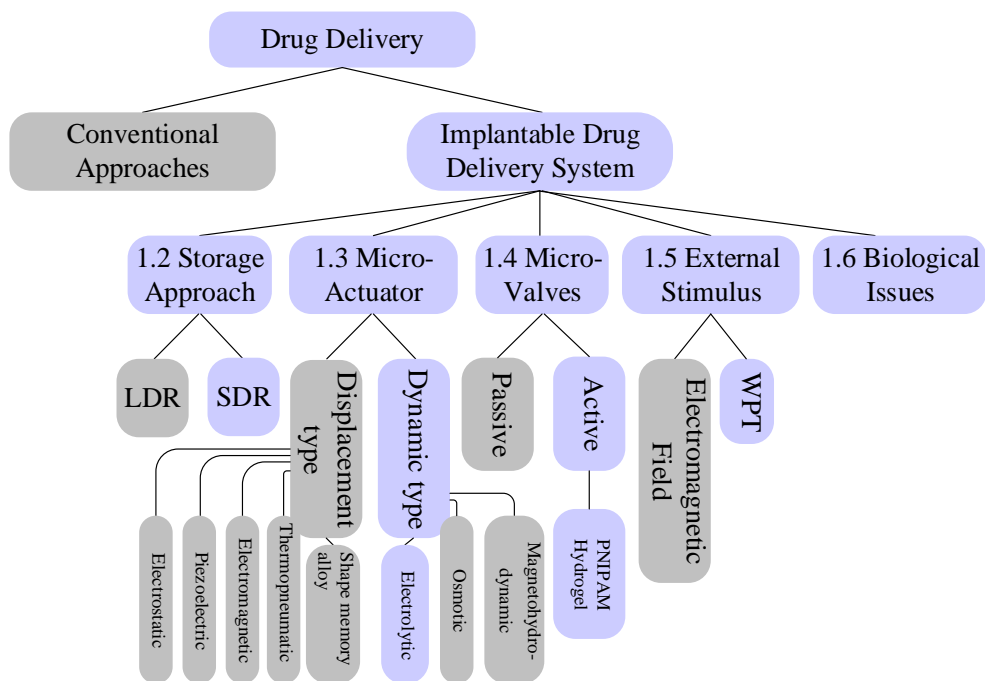


Figure 1.2 Taxonomy of drug delivery outlining the major content in subsequent subchapters. Blue boxes indicate the areas of concentration in this dissertation.

1.2 SDR Approach Applied in Drug Delivery Systems

The drug in liquid form has been adopted in many implantable drug delivery systems due to its high availability [45] and well-defined drug density, but this kind of storage approach usually brings a dosage dilemma caused by the limited space of the implants. Once the liquid drug is

depleted or the actuation diaphragm achieves its maximum deformation [22, 24], injecting more drug solution by piercing the reservoir membrane with a syringe needle or another refilling mechanism is required to extend the lifetime of the device [24, 25, 46], which in turn increases concerns about safety, medical cost, and extra surgical operations. Further, approximately 40% of new drug candidates possess low aqueous solubility [45, 47], such as docetaxel (solubility of 2.5 $\mu\text{g/L}$ in water). This low solubility limits the storage of hydrophobic drugs in liquid form, resulting in low dose availability for LDR based drug delivery systems. Moreover, for some specific drug delivery devices using the LDR approach, the biological fluids' reverse flow needs to be strictly controlled; for example, an electrolytic actuator using platinum (Pt) electrodes [22, 24, 48] required a complicated valve to control the reverse flow [24, 49] caused by electrolysis-bubble recombination due to the catalytic feature of Pt, otherwise, the liquid (outside the device) will refill the drug reservoir diluting the liquid drug concentration and affecting the dose at the disease site.

An alternative approach to LDR is to store the drug in solid form [50], which provides a solution to the dosage dilemma by increasing the capacity of the drug reservoir, permitting a long-term application (months or years), because the reproducible dose can be formed by repeatedly dissolving small amounts of the solid drug. In particular, the SDR approach is more advantageous for those drug delivery systems that use the hydrophobic drugs. Regarding the implantable drug delivery devices using solid drugs, the popular examples are based on diffusion and osmotic pressure. Diffusion based drug delivery devices, in their simplest actuation forms, can transport the drug out of or through a nano/micro-porous polymer membrane. The *pSivida* company has developed several influential ocular implants utilizing drug diffusion through a

polyvinyl alcohol (PVA) membrane, including *Vitrasert*[®] (approved in 1996) and *Retisert*[®] (approved in 2005) [51]. The *Vitrasert*[®] with a drug reservoir of 3.5 mm in length contains 4.5 mg ganciclovir for the treatment of CMV retinitis in patients with AIDS [51, 52], it releases the drug into the vitreous of the eye for approximately 5-8 months [53, 54]. The *Retisert*[®] implant (3 mm × 2 mm × 5 mm) contains 0.59 mg of fluocinolone acetonide in its 1.5 mm tablet reservoir [51, 52], which can provide a steady release rate of 0.3~0.4 µg/day over approximately 30 months [51, 52, 55]. *Alimera Sciences Inc.* used the *Iluvien*[™] ocular implant with a cylinder structure of 3.5 mm in length and 0.37 mm in diameter enclosing 190 µg fluocinolone for treating diabetic macular edema (DME) [51, 52]. The *Iluvien*[™] ocular implant has a potential lifetime of around 2-3 years. A compression molded polymer microchip (10 mm in diameter × 1 mm thick) with an array of micro-reservoir was used for treating brain tumors [56]; each reservoir was loaded with a maximum of 1.24 mg carmustine (BCNU) for targeted delivery, and drug release can be programmed by controlling the composition and thickness of the membrane cap of each micro-reservoir.

Osmotic gradient between an osmotic pump and the surrounding fluid causes an actuation force: the liquid outside the pump is drawn through a semi-permeable membrane causing pressure expansion in the osmotic chamber, which drives the drug towards the outlet of the device. A micro-osmotic actuator has been constructed for delivering the basic fibroblast growth factor (bFGF) for tissue regeneration [57], in which the PLGA sheets acted as a water-permeable membrane, and an osmotic potential drove water into the reservoir through such a semi-permeable membrane. This device is capable of providing a rate of 40 ng/day for 4 weeks. An integrated system called “*IntelliDrug*” [17] including an osmotic pump and an electro-active

polymer (EAP) valve was implanted into the human denture for delivering Naltrexone to the body through the buccal mucosa for treating drug addiction [58]. As shown in Figure 1.3, the drug was stored as a solid pill in the reservoir and dissolved by saliva that entered through a water-permeable membrane. Another osmotically driven subcutaneous implant called *Viadur*[®] (Bayer AG, Leverkusen, Germany) contains 65 mg of leuprolide (free base) and can provide a controlled drug release rate for treating advanced prostate cancer over 1 year [17].

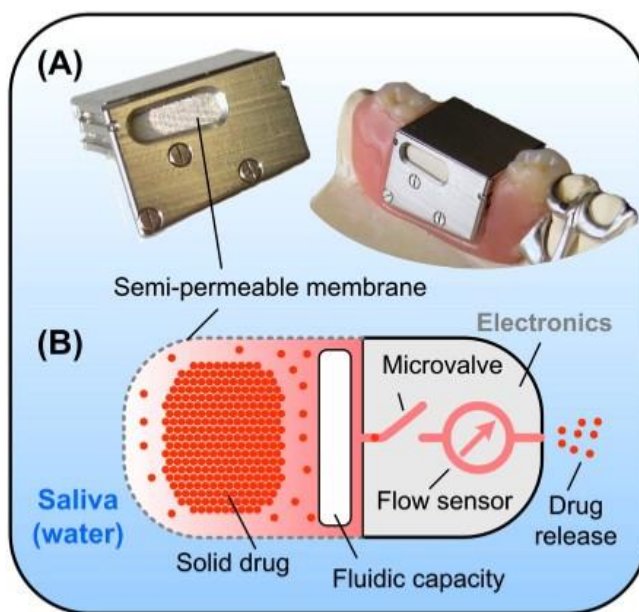


Figure 1.3 Prototype of *IntelliDrug* device and its operation principle [17][†].

To some extent, implantable drug delivery systems using diffusion or osmotic actuation are “passively controlled” [31, 59, 60], contributing to a constant release rate once the device is implanted. Mechanical actuations can provide an “actively controlled” drug delivery in which the released rate and dose are controllable. An early study investigated a shell-like implantable drug delivery system that used a shape-memory alloy (SMA) based micro-actuator [61],

[†] Reprinted with permission from Elsevier Publisher.

and the drug was enclosed in the shell as solid state. The SMA wire was adhered to a metal skeleton that was embedded in the shell's body; when the wire was heated, its deformation opened the shell, exposing the drug to the surrounding tissue, cells, and human liquid. An electrochemically activated implantable device with multiple gold membrane capped drug reservoirs was first demonstrated in [62]: when an electric potential was applied to the gold membrane that was immersed in a solution with physiological levels of saline, the thin gold caps (acting as an anode) dissolved in the solution in the presence of chloride ions due to electrochemical reactions, thereby exposing the reservoirs filled with drugs in solid, liquid or gel form to the surrounding environment, thereby releasing the drug. This design and the operation mechanism were adopted for delivering BCNU for treating brain tumors [4, 63]. Recently, Pirmoradi *et al.* introduced a magnetically controlled microfluidic device that is able to pump fluid in and out of the solid drug filled reservoir [30, 64, 65]. The reproducible drug solution can be released by cyclically refilling the reservoir and pumping the dissolved drug liquid, which maintains a constant docetaxel (DTX) release rate of about 171 ng/pulse for 35 days [30]. The corresponding actuation relies on deforming a magnetic membrane in an applied magnetic field (255 mT) as shown in Figure 1.4, providing a simplified control strategy. This device is intended to be surgically implanted behind the eye to provide a targeted delivery of DTX for the treatment of diabetic retinopathy [30, 65].

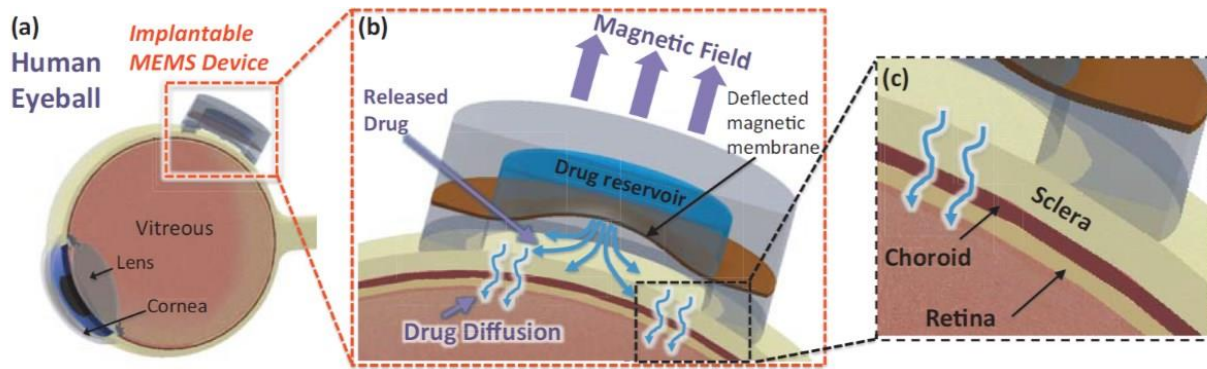


Figure 1.4 (a) Conceptual illustration of the intraocular drug delivery device sutured to the posterior eyeball; (b, c) Its operation principle [65][†].

1.3 Literature Review of Micro-Pump for Drug Delivery

The combination of MEMS with biochemical applications has attracted growing interest, especially in the field of drug delivery. MEMS fabrication technology applied in drug delivery systems can provide high release efficiency, an accurate dose, and more friendly operation [66]. MEMS based drug delivery devices usually consist of a micro-pump, a micro-fluid channel, a micro-valve and other necessary units. As an essential component of drug delivery devices, the micro-pump transfers the drug from the reservoir to body tissues or blood vessels safely and reliably. In general, MEMS fabrication-based micro-pumps require an actuator to displace the drug solution, and these come in two categories: reciprocating displacement and non-reciprocating types [19]. The reciprocating displacement actuation mechanisms are able to provide high drug release rates ($>10 \mu\text{L}/\text{min}$) [66, 67]; however compared to their non-reciprocating-type counterparts, they are larger, have more complicated structures, and have higher power consumption [3]. The working mechanism and fabrication process of different kinds of micro-pumps are described in detail below.

[†] Reprinted with permission from IEEE Publisher.

1.3.1 Reciprocating displacement micro-pump

In a reciprocating displacement micro-pump, physical actuators are required to perform a pumping function. The popular mechanisms that show potential in biomedical applications are electrostatic, piezoelectric, electromagnetic, thermopneumatic and SMA. Key features, dimensions, and performance characteristics of these micro-pumps are summarized and referenced in Table 1.1.

A. *Electrostatic*

The basic structure of an electrostatic micro-pump is shown in Figure 1.5. The primary composition of an electrostatic micro-pump involves an elastic membrane and counter electrodes that perform electrostatic actuation. When an appropriate voltage is applied on the two opposite electrostatic plates, the attached membrane will move in one direction, because a force is generated between the two plates according to *Coulomb's Law*, given by:

$$F = \frac{\epsilon AV^2}{2x^2} \quad (1.1)$$

where ϵ is dielectric constant, A is the electrode area, x denotes the spacing between two plates, and V means the applied voltage. When the applied voltage turns off, the deflected membrane will move back to its initial position. By repeatedly turning on and off the applied voltage, the available volume inside the chamber is changed alternately so that the fluid can be sucked into the chamber and pumped outwardly.

Table 1.1 Reciprocating displacement micropumps

<i>Actuation</i>	<i>Reference</i>	<i>Structure material</i>	<i>Size (mm³)</i>	<i>Valves</i>	<i>Pump chambers</i>	<i>Diaphragm material</i>	<i>Diaphragm Thickness (μm)</i>	<i>Pumping medium</i>	<i>Voltage (V)</i>	<i>Power (mW)</i>	<i>Actuation Frequency (Hz)</i>	<i>Pressure (kPa)</i>	<i>Flow rate (μL/min)</i>	<i>Transduction efficiency (μL/J)</i>	<i>Application reported in reference</i>
<i>Electro-static</i>	[68] Zengerle <i>et al.</i> , 1992	Silicon	98	Cantilever type	1	Silicon	25	Water	170	n/r	25	2.5	70	n/r	n/r
	[69] Cabuz <i>et al.</i> , 2001	Plastic	225	Passive	1	Metallized kapton.	n/r	Gas	160	n/r	66	n/r	30000	n/r	Chemical & biological
	[70] Teymoori <i>et al.</i> , 2005	Silicon, glass	28	Active valve	3	Polysilicon	2	n/r	23	n/r	50	n/r	9.1	n/r	Chemotherapy
	[71] Machauf <i>et al.</i> , 2005	Silicon	n/r	Valveless	1	Nickel	60	Water	50	n/r	1830	n/r	1	n/r	n/r
	[72] Kim <i>et al.</i> , 2015	Silicon	479.4	Checker-board type	2	Parylene, Cr and Au	3.4	Gas	100	57	15k	17.5	4000	1170	n/r
<i>Piezo-electric</i>	[74] Koch <i>et al.</i> , 1998	Silicon	n/r	Cantilever type	1	Silicon	70	Ethanol	600	n/r	200	2	120	n/r	Drug delivery
	[75] Junwu <i>et al.</i> , 2005	PMMA	n/r	Cantilever type	1	Beryllium bronze	n/r	Water	50	n/r	800	23	3500	n/r	Drug delivery
	[76] Feng <i>et al.</i> , 2005	Silicon	160	Passive	1	ZnO and parylene	16.5	Water	80	3	60k	0.12	3.2	17.8	Implantable application
	[77] Ma <i>et al.</i> , 2006	Silicon	7037.2	Check valve	1	PZT and silicon	180	Fluid with glucose	67.2	n/r	208	3.43	40	n/r	Transdermal insulin delivery
	[78] Geipel <i>et al.</i> , 2006	Silicon	7.6	Active	1	PZT	80	water	100	n/r	2	10	5	n/r	Drug delivery
	[79] Doll <i>et al.</i> , 2006	Silicon, PMMA	330	Active	1	PZT	n/r	Water	n/r	n/r	27.8	60	1800	n/r	Implantable application
	[80] Hsu <i>et al.</i> , 2008	Silicon, glass	n/r	Passive	3	Glass and PZT	150	Blood	140	n/r	450	1.8	50.2	n/r	Drug delivery
	[82] Bohm <i>et al.</i> , 1999	Plastic	800	Passive membrane	1	Silicone rubber	200	Water	5	500	50	n/r	2100	70	n/r
<i>Electro-magnetic</i>	[83] Santra <i>et al.</i> , 2002	Silicone elastomer	3535	Passive	1	Silicone rubber	200	Air	10	1900	4.5	1.016	260	2.3	n/r
	[84] Yamahata <i>et al.</i> , 2005	PMMA	20	Nozzle/diffuser	1	PDMS	n/r	Water	n/r	n/r	12	0.02	400	n/r	Lab-on-a-chip systems
	[85] Pan <i>et al.</i> , 2005	PDMS, PCB	600	Ball check valves	1	PDMS	100	Water	n/r	500	5	3.6	1000	33.3	Lab-on-a-chip systems
	[87] Jeong <i>et al.</i> , 2000	Pyrex glass, Silicon	n/r	Nozzler/Diffuser	1	p+ Silicon	2	Water	8	320	4	2.5	14	0.7	n/r
<i>Thermo-pneumatic</i>	[88] Zimmermann <i>et al.</i> , 2004	Glass, silicon	n/r	Planar flap valve	1	n/r	n/r	Isopropyl alcohol	n/r	180	10	16	9	0.8	Cryogenic systems/ Drug Delivery
	[89] Hwang <i>et al.</i> , 2005	Glass, SU8 and silicon	105.3	Capillary stop valve	2	n/r	n/r	Water	20	580	n/r	n/r	3.33	0.11	Transdermal Drug delivery
	[90] Jeong <i>et al.</i> , 2005	PDMS	n/r	Active	3	PDMS	30	Water	20	n/r	2	0	21.6	n/r	Drug delivery systems
	[91] Kim <i>et al.</i> , 2005	PDMS, glass	n/r	Diffusers	1	PDMS	770	Methanol	55	n/r	6	n/r	0.078	n/r	Lab-on-a-chip
	[92] Benard <i>et al.</i> , 1997	Silicon	n/r	Check valves	1	TiNi	3	Water	0.6	540	0.9	4.23	50	1.5	n/r
<i>Shape memory alloy</i>	[93] Xu <i>et al.</i> , 2001	Silicon	54	Flap check valve	1	NiTi and Silicon	20	Water	n/r	n/r	40-60	100	340	n/r	n/r
	[94] Makino <i>et al.</i> , 2001	Pyrex glass, Silicon	280	Check valve	1	TiNi	6	Water	n/r	400	n/r	100	4.8	0.2	n/r
	[95] Guo <i>et al.</i> , 2004	Acryl-silicon rubber	445	Diffusers	1	NiTi alloy	n/r	n/r	6	n/r	1~10	n/a	700	n/r	Biomedical application

Transduction efficiency: Ratio between flow rate and power; n/r: Not reported.

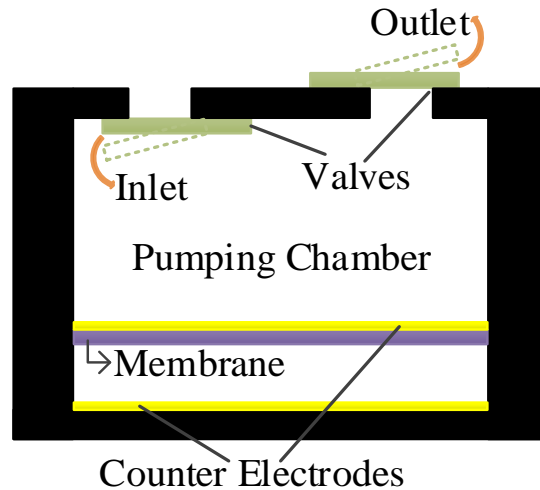


Figure 1.5 Cross section of an electrostatic micro pump.

The earliest electrostatic micro-pump was reported by Zengerle *et al.*, where a silicon membrane was used in the pump with an outer dimension of $7 \times 7 \times 2 \text{ mm}^3$, and a pumping rate of $70 \text{ }\mu\text{L}/\text{min}$ was achieved when a voltage of 170 V was applied with a frequency of 25 Hz [68]. Cabuz *et al.* developed a dual diaphragm micro-pump which can achieve a flow rate of $30 \text{ mL}/\text{min}$ at a driving voltage of 160 V ; this micro-pump operated in bidirectional mode but was applicable for gases only [69]. Teymoori and Sani designed a 3-chamber electrostatic pump for biomedical applications, such as chemotherapy, it provided a flow rate of $9.1 \text{ }\mu\text{L}/\text{min}$ at a threshold voltage of 18.5 V in a simulation model [70], although the actual fabrication and experimental measurements to verify the simulation performance were not reported. Electrostatic micro-pumps show a fast response time and a high pumping rate, but at the cost of a relatively complicated structure and a high applied voltage.

B. Piezoelectric

Piezoelectric effect is generally regarded as the linear electromechanical interaction between the mechanical and the electrical states in certain types of materials, such as piezoelectric

lead zirconate titanate (PZT). A flexible membrane of piezoelectric material will deform to a certain degree if a voltage is applied onto it as shown in Figure 1.6. In the piezoelectric micro-pump, the shaking membrane acts like a push plate to displace the fluid in and out of the chamber.

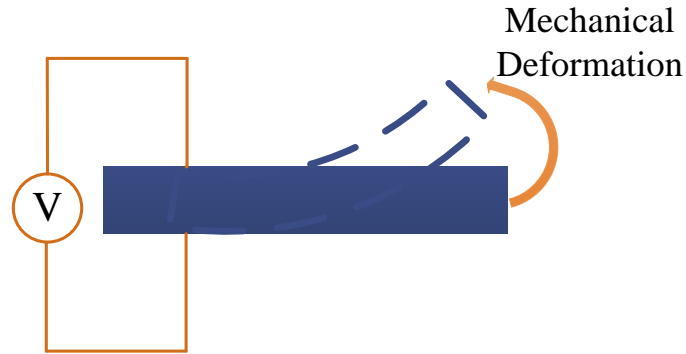


Figure 1.6 Piezoelectric effects.

An early piezoelectric micro-pump that was used for insulin delivery was fabricated in 1978 [73]. A high-performance cantilever-valve micro-pump that used a PZT actuator was investigated for drug delivery, which achieved a high flow rate of 3.5 mL/min [75] Ma *et al.* developed a novel PZT micro-pump integrated with a micro-needle array for delivering transdermal drugs, with a flow rate of 40 μ L/min obtained at a driving voltage of 67.2 V [77]. The piezoelectric actuation presents a high displacement, good reliability, fast response time and energy efficiency [81], but the required voltage is above dozens of volts, bringing safety issues for human body implantation.

C. Electromagnetic

A typical electromagnetic micro-pump consists of a pumping chamber, a flexible membrane

together with a permanent magnet, driving coils, and valves (see Figure 1.7). The electromagnetic force (or *Lorentz* force) is generated in the presence of an external magnetic field, which can be created by a permanent magnet. When a current is driven through the coils, an attraction or repulsion between the coils and the magnet happens, deforming the membrane. Therefore, elastic membranes, such as a polydimethylsiloxane (PDMS) membrane, are usually adopted to obtain a large deflection and pumping volume.

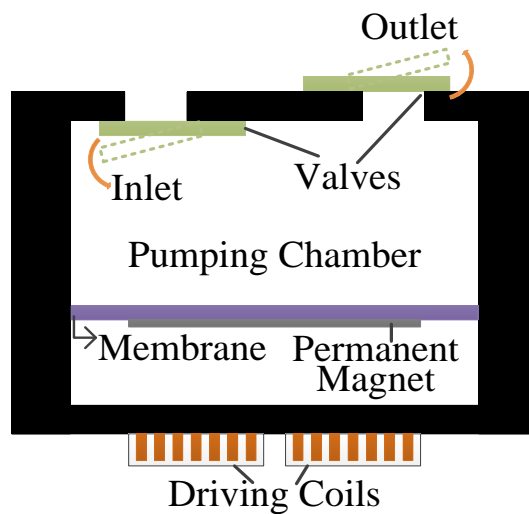


Figure 1.7 Cross section of an electromagnetic micro pump.

Bohm *et al.* proposed an electromagnetic pump using conventional micromechanical production methods. A NdFeB permanent magnet with a diameter of 5 mm and a height of 1.6 mm was glued onto a flexible silicone rubber membrane, and an alternating square-wave current of 100 mA at 50 Hz was applied across the coil, achieving a maximum pump rate of 2.1 mL/min, at a high rate of power consumption (5V, 100mA) [82]. A NdFeB magnetic disc having a diameter of 3.1 mm and a thickness of 1.6 mm was attached to the PDMS membrane, which provided a pumping rate of 1 mL/min with a 10-turn planar coil fabricated

on a PC board; it required 500 mW of power [85]. A current of 500 mA was required to make the membrane deflect, causing a 55 μm deflection as measured in [86]. Electromagnetic actuation can achieve high displacement due to its large deflection, as well as a fast operation response because electromagnetic fields arise and disappear rapidly. However, electromagnetic micro-pumps need to consume relatively large amounts of power, which causes large heat dissipation.

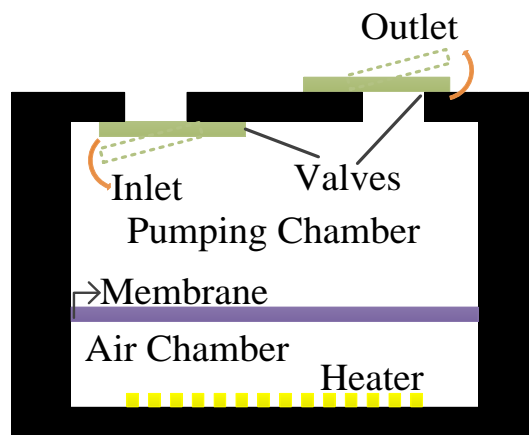


Figure 1.8 Cross section of a thermopneumatic micro-pump.

D. Thermopneumatic

A thermopneumatic micro-pump consists of a heater, a sealed cavity and a diaphragm as shown in Figure 1.8. The cavity is full of air or fluids, and once power is applied to the heater, the temperature inside the cavity increases, resulting in thermally induced volume change and/or phase change of fluids. The membrane is thereby deflected for actuation due to the pressure increase in the air chamber. When the power is removed, temperature and pressure in the cavity decrease, which makes the membrane move back to its original state.

An influential work on the thermopneumatic micro-pump was reported in [88] in which a

flow rate of 9 $\mu\text{L}/\text{min}$ was measured, consuming power of 180 mW. Hwang *et al* proposed a submicroliter level thermopneumatic micro-pump with a size of 13 mm \times 9 mm \times 0.9 mm for delivering a transdermal drug [89], where the resistance of the micro-heater was 690 Ω , and the pumping volumes were 0.1 μL for 3 s at 15 V, and 0.1 μL for 1.8 s at 20 V. The power supply for the thermopneumatic micro-pump should be retained constantly above a certain level, resulting in large power consumption. Moreover, the response is also very slow due to the thermal inertia of the device.

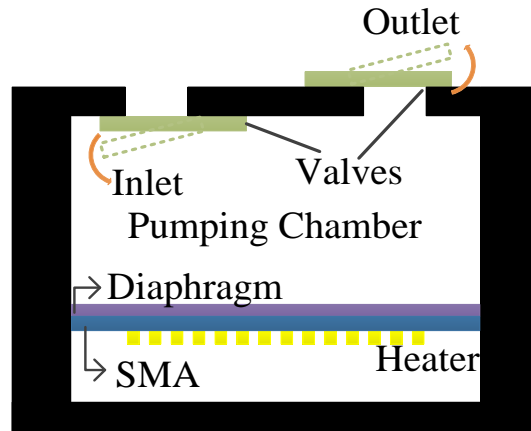


Figure 1.9 Cross section of a SMA micro-pump.

E. Shape memory alloy

Certain materials, such as titanium nickel (TiNi) alloy, inherit the property of shape memory. The shape memory effect represents a phase transformation between Austenite phase at high temperature and Martensite phase at low temperature. When SMA is heated, it will cause a shape deformation that can be used as an actuation upon a diaphragm; while cooling back to the Martensite phase, the SMA will return to its original shape. By repeatedly heating and cooling the SMA material, a continuous pumping is achievable. A simple design for an SMA

actuator is shown in Figure 1.9, where a highly elastic SMA membrane is generally required in the actuator.

TiNi is a popular material used in the SMA actuator, as it provides a large deformation and pumping rate, and can sustain a high operating pressure due to its highly recoverable strain. An early work used TiNi to achieve a maximum pumping flow rate of 50 $\mu\text{L}/\text{min}$ at an operating current of 0.9 A and voltage of 0.6 V in [92]. Xu *et al.* reported a typical SMA micro-pump [93], which obtained a high flow rate of 340 $\mu\text{L}/\text{min}$ at a driving current of 120 mA. [94]. For biomedical applications, a novel SMA micro-pump that used a TiNi wire coil was developed in [95], with a body size of 9 mm in diameter and 7 mm in length, achieving a maximum flow rate of 700 $\mu\text{L}/\text{min}$ under the applied voltage of 6 V and current of 0.25 A. An SMA actuator based implantable drug delivery device was designed to maintain a lifetime of at least 10,000 cycles with each dose of 5 μL ; the pump had a fast opening time of 0.66s but with high power consumption of 120 mW [61]. A SMA pump can retain a large deflection, withstand high stress (>200 MPa), and have a long operation period. However, it needs particular SMA materials and the high power consumption is a concern for many biomedical applications.

1.3.2 Non-reciprocating type micro-pumps

In contrast to a reciprocating displacement actuator, non-reciprocating counterparts do not need any physical actuation component [19]; the corresponding working principle is generally based on the conversion of non-mechanical energy to kinetic momentum. Most non-reciprocating type micro-pumps usually have neither moving mechanical parts nor

complicated valves so that the corresponding geometry design and fabrication process are relatively simple [66]. There are many kinds of non-reciprocating type actuation mechanisms, however, some of them are not suitable for drug delivery applications due to safety issues. For example, an electroosmotic (EO) actuation requires a voltage of several thousand volts [96, 97]; an electrowetting (EW) actuation may not be applied to the human body because liquid-phase metal (such as mercury) is used, this increases the toxicity concerns [98]. The other possible actuation mechanisms associated with biomedical applications include magnetohydrodynamic (MHD), osmotic-type, and electrolytic reactions. Key features, sizes, and performance characteristics of these types of micro-pumps are summarized and referenced in Table 1.2.

Table1.2: Non-reciprocating type micro-pumps.

<i>Actuation Mechanism</i>	<i>Reference</i>	<i>Structure material</i>	<i>Size (mm³)</i>	<i>Diaphragm material</i>	<i>Diaphragm Thickness (μm)</i>	<i>Pumping medium</i>	<i>Voltage (V)</i>	<i>Power (mW)</i>	<i>Flow rate (μL/min)</i>	<i>Transduction efficiency (μL/J)</i>	<i>Applications reported in reference</i>
MHD	[99] Jang <i>et al.</i> , 2000	Silicon	16	/	/	Seawater	60	108	63	9.7	n/r
	[100] Huang <i>et al.</i> , 2000	PMMA, Glass	8	/	/	NaOH solution	15	n/r	1200	n/r	Biomedical studies
	[101] Lemoff <i>et al.</i> , 2000	Silicon	6.08	/	/	NaCl	6.6	n/r	18.3	n/r	Biological microfluidic systems.
	[102] Homsy <i>et al.</i> , 2005	Pyrex, PDMS	3	/	/	KCl	15	n/r	0.5	n/r	Miniaturized total analysis systems
Osmotic	[103] Su <i>et al.</i> , 2002	Cellulose acetate	0.51	Saran F-310	40	Water	/	/	0.2E-3	/	Implantable drug delivery
	[104] Su <i>et al.</i> , 2004	Mylar, PDMS	12.5	Saran F-310	30	Water	/	/	3.3E-3	/	Implantable drug delivery
Electrolytic	[105] Ateya <i>et al.</i> , 2004	Silicone, PDMS	n/r	/	/	NaCl solution	4.3	n/r	24E-3	n/r	Lab on a chip, drug delivery
	[23] Li <i>et al.</i> , 2008	Silicone rubber, Parylene C	54	/	/	Water	n/r	n/r	7	n/r	Intraocular drug delivery
	[106] Chiu <i>et al.</i> , 2009	PDMS, Teflon, Glass	n/r	/	/	Blood	2.5	52E-3	88E-3	28.2	Micro total-analysis-systems, biochips.
	[22] Li <i>et al.</i> , 2010	Glass, Parylene C	46	Parylene C	10	Water	n/r	n/r	6.5	n/r	Implantable drug delivery

Transduction efficiency: Ratio between flow rate and power; n/r: Not reported; /: Does not apply.

A. Magnetohydrodynamic (MHD)

MHD micro-pump needs a structure in which both an electrical field and a magnetic field exist simultaneously. As shown in Figure 1.10, two opposite walls of the micro-channel are bounded by electrodes to generate an electric field and two permanent magnets with opposite polarity are placed on the other two walls to create a magnetic field. The corresponding structure is shown in Figure 1.10. MHD actuation is based on the *Lorentz* force between the electrically conductive fluids (conductivity > 1 S/m) and the magnetic field. When voltage is applied to the electrodes, causing an electric field, the working fluid will flow according to the direction of *Lorentz* force; the direction of movement is perpendicular to both the electrical field and the magnetic field.

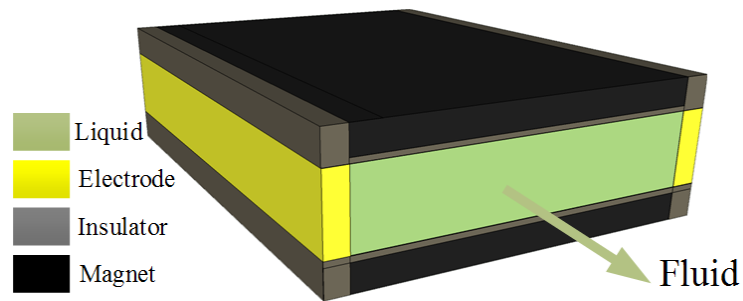


Figure 1.10 Schematic illustration of a MHD micro pump.

Jang and Lee proposed an early MHD micro-pump [99], where seawater (conductivity of 4 S/m) was chosen as the working fluid in the magnetic field with a flux density of 0.44 T, the applied voltage varied from 10 V to 60 V, and a maximum flow rate of 63 $\mu\text{L}/\text{min}$ was achieved at the current of 1.8 mA. A LIGA microfabrication based MHD micro-pump was investigated and tested in [100], where a peak flow rate of 20 $\mu\text{L}/\text{s}$ was achieved for 2% NaOH solution under a voltage of 15 V and a magnetic flux density of 1.05 T. MHD is able

to achieve a moderate flow rate, but at a cost of a complicated structure and the requirement of a conductive liquid to be pumped.

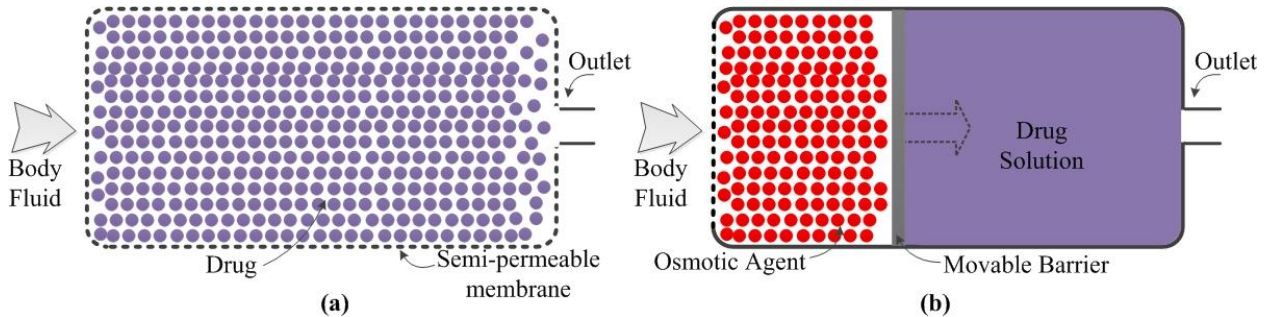


Figure 1.11 A schematic diagram of the osmotic type micro-pump for drug delivery application. (a) Operation principle of a single compartment pump. (b) Operation principle of a two-compartment pump.

B. Osmotic

Osmosis is a fundamental phenomenon that occurs when two solutions with different concentrations are separated by a semi-permeable membrane. Solvent molecules on the one side are allowed to pass across the semi-permeable membrane while the passage of solute on the other side is rejected; an osmotic flow across the semi-permeable membrane is generated from the region of low solute concentration to the region of higher solute concentration for compensating differences in solute concentrations, resulting in a hydrostatic pressure difference on the two sides of the semi-permeable membrane. As a consequence, the hydrostatic pressure exerts an osmotic force upon an actuation diaphragm. In general, osmotic micro-pumps can be divided into two categories based on the number of compartments [17]. Take an example of the osmotic micro-pump based drug delivery application shown in Figure 1.11. Figure 1.11(a) illustrates a single compartment osmotic system where body liquid acts as the solvent flowing across the membrane, dissolving the

drug and then displacing the drug solution through the outlet. In two compartment systems as shown in Figure 1.11(b), the solvent dissolves an osmotic agent (such as solution with higher concentration or solid state solute) stored in a separate confinement from the drug. The region of the osmotic agent expands, thereby pushing the movable barrier, and consequently, the liquid drug is pumped outward.

Su and Lin reported two types of osmotic micro-pumps, a semipermeable-piston type and an impermeable-piston type, with sodium chloride as the osmotic driving agent, achieving constant flow rates of 4.5 and 11.5 nL/h, respectively [103]. In the impermeable-piston type osmotic micro-pump, the actuation diaphragm was made of vinylidene chloride and acrylonitrile copolymer (Dow Saran F-310); water from the aqueous environment was drawn through a semipermeable membrane into the actuator chamber and the induced volume expansion deformed the diaphragm, achieving a flow rate of 0.2 $\mu\text{L/h}$ [104]. An osmotic pump doesn't require extra power stimulus, making it a suitable candidate for drug delivery applications with low dosing requirements and passive controllability.

C. Electrolytic

More recently, electrolytic actuators have attracted growing interest, and their working principle is mainly based on the expansion of electrolysis gases [105]. When the voltage is applied to the electrolysis electrodes which are immersed into the electrolyte, electrolytic reaction happens, resulting in the dissociation of the electrolyte. For example, DI water can be electrolyzed into hydrogen and oxygen gases (H_2 and O_2). The generated gases increase the pressure in the chamber, which drives the fluid, as depicted in Figure 1.12. In contrast to

the other actuation mechanisms, the electrolytic reaction doesn't require a high voltage, for example, the voltage threshold for the electrolysis of water is 1.23 V.

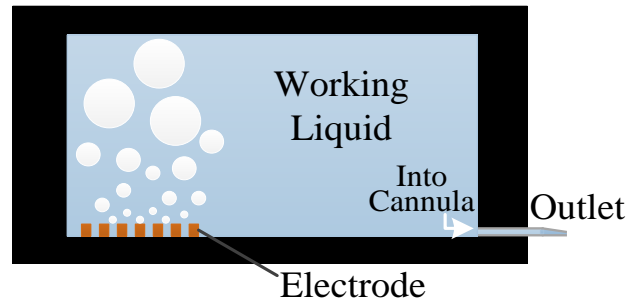


Figure 1.12 Cross section of the electrochemical micro-pump illustrating electrolysis-generated bubble pumping the liquid directly.

In recent years, Meng's group has done some influential works in electrolytic bubble-actuated drug delivery systems. An intraocular drug delivery device was investigated in [23], where the electrolysis of drug solution and pumping were occurring simultaneously because the liquid drug also performed the function of an electrolyte. This work provided a pumping rate range from 438 pL/min to 7 μ L/min using driving currents from 5 μ A to 1.25 mA. A microfluidics system integrated with an electrolysis-based micro-pump exhibited advantages for blood transportation in [106], where a pumping rate of 88 nL/min was achieved at a cost of power consumption of 52 μ W. An optimum electrolytic actuator design using a Parylene bellows was demonstrated in [22], obtaining a maximum flow rate of 6.5 μ L/min at a driving current of 1 mA.

By comparing the works reported in Tables 1.1 and 1.2, the electrolytic pump shows strong potential applications for implantable drug delivery systems due to its low power consumption, low voltage requirement, high transduction efficiency, appropriate flow rate

and active controllability. Moreover, electrolytic micro-pumps usually have a relatively simple structure, showing both fabrication and operational advantage. Therefore, the electrolytic actuation mechanism is adopted for our implantable drug delivery system.

1.4 Introduction to Microvalve

A microvalve was first reported in 1979 [107], and great progress has been made during the last three to four decades. Currently, microvalves are able to be integrated with many microfluidic systems for flow regulation, on/off switching and sealing of the microsystems [108]. Based on their controllability, microvalves can be generally categorized as passive microvalves and active microvalves. Passive microvalves are often regarded as one part of micropumps: most of them are incorporated in inlets and outlets of reciprocating displacement-type micropumps as mechanical moving parts, including flaps [93, 109], membranes [110, 111], balls [112, 113] or mobile structures [85, 114, 115]. Passive microvalves do not require extra power and have a relatively simple structure, but their valving performance depends on forward pressure as the valves only open in the forward direction. They exhibit poor valving efficiency in the reverse flow direction, and leakage flows are commonly observed at low backward pressure [108].

Active microvalves have either mechanical or non-mechanical actuating parts. Technically, mechanically active microvalves can be fabricated by MEMS technologies, where the mechanically movable part can be actuated by magnetics [116-118], electrostatics [119-121], piezoelectrics [122, 123], thermal effects [3, 26, 124, 125], or other approaches [126, 127]. These kinds of microvalves have similar actuation mechanisms as the displacement-type

micropumps illustrated in subsection 1.3.1; they usually require a high level of current (≥ 10 mA) or voltage (≥ 50 V), and they consume extra power [108]. Non-mechanical valving function is accomplished by the application of “smart” materials with electro-rheological [128], electrochemical [129, 130] or phase change properties. Phase change based microvalves are newly emerged, and usually exhibit cost, operation and fabrication advantages compared to other active microvalves [108]. Popular phase change materials include hydrogel [28, 131-134], sol-gel [135, 136], paraffin [137-140], and ice [141].

As a phase change material, PNIPAM hydrogel that reacts to temperature change is maturely developed and of great interest in many applications, such as sensing [142, 143], bio-membranes [144], colour tuning [145], radiotherapy [146], optics [147], cell attachment and cell culturing [148-150]. PNIPAM is also a suitable platform for many biomedical applications due to its high tunability in water, simple synthesis, and biocompatibility [151]. For example, PNIPAM was directly used as drug delivery vehicle [28] to provide a controlled release of ophthalmic drops for glaucoma therapy dependent on the phase change caused by ambient temperature change [152, 153]. The corresponding principle is that the PNIPAM hydrogel's volume changes at a temperature transition point referred to as the lower critical solution temperature (LCST). Below the LCST, PNIPAM is hydrophilic, swelling with water molecules when placed in an aqueous environment, while it shows hydrophobicity once its temperature exceeds LCST, thereby expelling water molecules and shrinking in volume. Figure 1.13 illustrates the volume change of PNIPAM below and above LCST, respectively. This thermal-responsive, reversible swelling/shrinkage behavior occurs because hydrogen bonds between water molecules and the amide groups of PNIPAM dominate the

intermolecular association below LCST. However, the hydrogen bonds will break, and hydrophobic interaction between the isopropyl groups of PNIPAM chains will become more significant at a higher temperature than LCST.

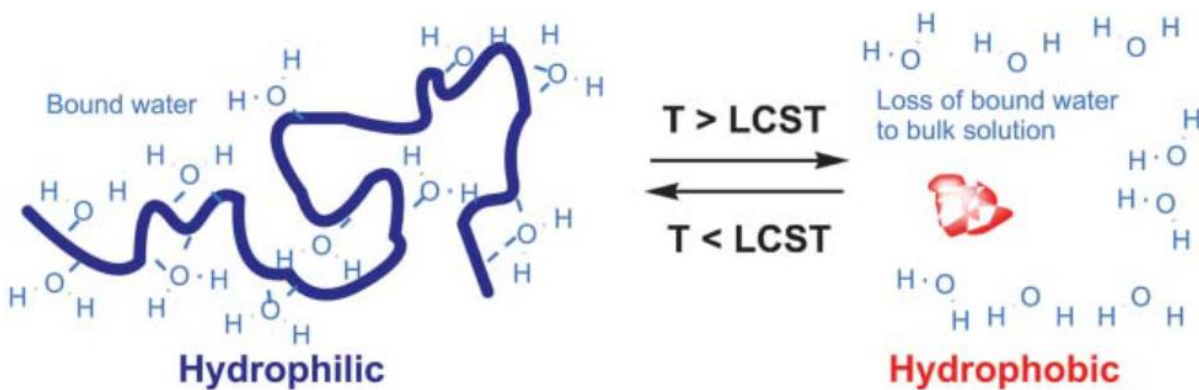


Figure 1.13 Illustration of thermos-responsive behavior of PNIPAM [154][†].

In addition to the thermo-responsive nature and reversible hydrophilic to hydrophobic transition, PNIPAM hydrogel is able to embrace magnetic particles due to its viscoelasticity, allowing heat generation by an external induction heating system. These features can be exploited for a remotely operated microvalve, showing another novel application of PNIPAM hydrogel. Ghosh *et al.* first reported a simple form of remote actuation of a PNIPAM based microvalve, using an oscillating magnetic field as an external stimulus [27]. In their work, ferromagnetic nanoparticles (Fe_3O_4) were embedded in PNIPAM hydrogel, generating heat in the magnetic field (operated at 100–1000 kHz) and causing the PNIPAM to shrink, consequently accomplishing the valving functions. The experimental data indicated that the volume of polymer monolith inside the microfluidic channel decreased by approximately 80%, and the magnetic field actuated shrinking response time was about 3 seconds, showing a fast response to external stimuli.

[†] Reprinted with permission from Royal Society of Chemistry Publisher.

Rahimi *et al.* investigated a proof-of-concept wireless implantable drug delivery device integrating PNIPAM hydrogel microvalves with a planar inductor-capacitor (LC) resonant circuit that was used as wireless heater [33]. The heater circuit using a spiral coil was fabricated on a polyimide film and exposed to a radiofrequency (RF) magnetic field. The corresponding working principle is that the heater generates heat due to the power consumed in the circuit only when the frequency of the field is tuned to the resonant frequency of the LC circuit, thereby causing the temperature increase of PNIPAM. Consequently, the microvalves open due to the shrinkage of PNIPAM hydrogel. While tuning the operating frequency away from the resonant frequency of the circuit would cool down the heater, in this case, the release holes are gradually sealed by swelling PNIPAM hydrogel, and drug diffusing out from the reservoir is terminated afterwards. The experimental results indicated that the PNIPAM hydrogel achieved a 38% maximum volume shrinkage in the microvalves and the whole device showed no detectable leak over a non-actuation period for 12 hours. It reveals that the PNIPAM hydrogel microstructures are able to offer a robust seal against the liquid diffusion.

Considering that the SDR drug delivery system needs the reverse fluid from outside the device to replenish the drug reservoir, PNIPAM hydrogel has a swelling time within which the liquid can pass through it when serving as the soft material for a valve. PNIPAM microvalves can be triggered remotely, which may further facilitate the integration of the valve and other implantable micro-actuators. Moreover, localized heating is not uncommon in biomedical treatments, and as the temperature in the heating area is easy to regulate, this allows feasible operation of a PNIPAM valve. Therefore, we adopt PNIPAM hydrogel to

control the outlet of the drug delivery device. Combining the similar valve design of encapsulating the magnetic particles in the PNIPAM hydrogel with the electrolytic pump shows the potential to share the same remote power source and reduce the system complexity. This will be demonstrated in this dissertation.

1.5 Introduction to WPT

Wireless power transfer (WPT) has been proven as an effective method for powering implantable electronics [155, 156], because a built-in battery has a limited lifetime and its replacement requires surgery for a majority of implants. Moreover, size is a limited factor for many implantable biomedical electronics, because space is not available for batteries. By making use of WPT technology, the battery can be replaced. Consequently, the whole size is drastically reduced by using an electronic circuit that connects directly to the implantable device, resulting in a compact structure. Purely optical radiation is one kind of WPT, but compared to the recently developed WPT technologies, the least amount of power is transferred due to the severe effects of path loss. In order to achieve high power transfer efficiency (PTE), WPT systems using various coil models are investigated below.

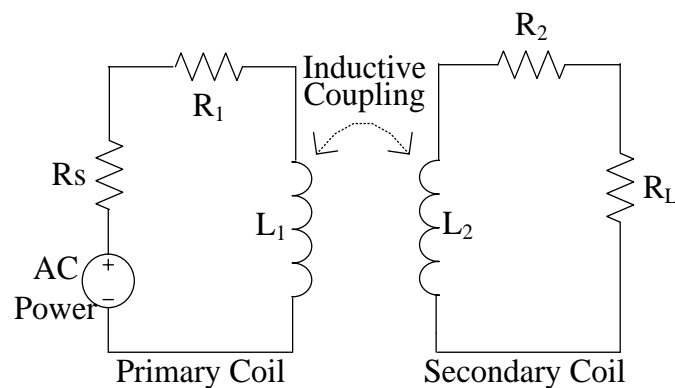


Figure 1.14 The inductive coupling based circuit model.

1.5.1 Inductive-coupling type

A conventional WPT system is based on inductive coupling or through electromagnetic induction. In such systems a primary coil carries alternating current (AC) that creates a sinusoidal varying magnetic field (and flux), inducing a voltage across another separate coil. It transfers power with a relatively high efficiency to a load. For simplicity, a two coil model is used here as an example of inductive coupling. The corresponding circuit model is shown in Figure 1.14, where R_s represents the source own resistance, and R_{1-2} and L_{1-2} denote the resistances and inductances of the two coils, respectively. R_L is the load. Based on this circuit model of two coupled inductance, the equivalent impedance Z can be calculated as:

$$Z = (R_s + R_1) + j\omega L_1 + \frac{k^2 \omega^2 L_1 L_2}{j\omega L_2 + R_2 + R_{load}} \quad (1.2)$$

where k is the coupling coefficient of the two coils.

Power transfer efficiency (PTE) that strongly depends upon the quality factor (Q -factor) of the primary coil (Q_p), secondary coil (Q_s) and coupling coefficient (k) is a critical parameter for evaluating the performance of inductive coupling, and it is given by [44, 157]:

$$\eta_{2-coil} = \frac{k^2 Q_p Q_s}{1 + k^2 Q_p Q_s} \quad (1.3)$$

where the general Q calculation is defined as:

$$Q = \frac{2\pi fL}{R} \quad (1.4)$$

where f represents the operating frequency of the coil, L means the inductance of the coil, and R is the equivalent resistance of the circuit. Herein, Q factor indicates the ratio of stored energy to the energy losses.

An early study on inductively powering the implantable monitoring and stimulating device was presented in [158]; this device was able to deliver power of more than 50 mW with a transfer efficiency of 36% at a separation distance of 30 mm. In [159], copper coils were patterned on a polyimide-based, flexible printed circuit board (PCB), using a ferromagnetic core to reduce the magnetic flux dissipation, and the PTE was enhanced to 34% at a transfer distance of 5 mm. Although the inductive-coupling type WPT system has the advantage of simple construction, it requires a strict alignment between the coils and is critically sensitive to the transfer distance so that PTE will drop dramatically with increasing distance.

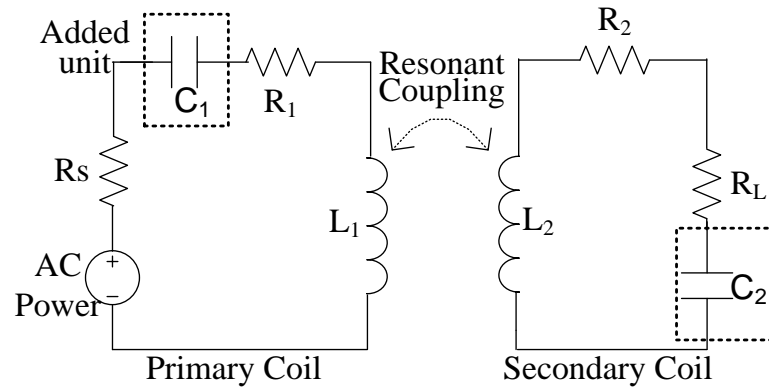


Figure 1.15 The resonance-based circuit model of added capacitors.

1.5.2 Resonance-based type

A recently developed R-WPT technology has attracted growing interest due to its improved PTE and stability [44, 160-162]. Compared to purely inductive coupling, R-WPT needs extra capacitors to create resonant coupling between the inductors; the corresponding principle is that mutually separated coils operate at the same resonant frequency to form a resonant circuit, which allows peak power to be transferred wirelessly from the driver coil to the load coil. To improve the pure inductive link, as shown in Figure 1.14, two capacitors are added

into the resonant circuit model (see Figure 1.15). This LC circuit design has the benefit of a higher PTE over a relatively long distance. When the coils operate at the resonance frequency, the impedance of the circuit drops to the lowest level while the transferred current achieves a maximum. The same resonance frequency f_0 over each coil can be adjusted according to:

$$f_o = \frac{1}{2\pi\sqrt{L_m C_m}} \quad (1.5)$$

where m denotes the coil order, L and C represent the inductance and capacitance, respectively.

In the resonance circuit model, the imaginary part in the equivalent impedance can be deleted since the operating currents on the circuits become stable. Consequently the equivalent impedance can be expressed as:

$$\begin{aligned} Z &= Z_{coil1} + Z_{coil2} \\ &= (R_s + R_1) + \frac{k^2 W^2 L_1 L_2}{R_2 + R_{load}} \end{aligned} \quad (1.6)$$

Accordingly, PTE can be obtained as:

$$\eta = \frac{Z_{coil2}}{Z} \times \frac{R_{load}}{R_2 + R_{load}} \quad (1.7)$$

An influential R-WPT work was reported by Soljagic's group [160, 161], using a resonant frequency of nearly 10 MHz on both the primary and secondary coils to wirelessly power a 60 Watt light bulb connected to a load coil over a distance of 2 meters. The corresponding power transfer efficiency reached up to 40%, which confirms that R-WPT systems can

deliver high power over a long distance. Inspired by Soljacic's works, miniaturized R-WPT systems for potentially implantable electronics applications were investigated in [44, 162]. The theoretical calculations of the resonant coupling link were derived in terms of self-capacitance, self-resonant frequency, and Q -factor in [163]. A detailed 4-coil R-WPT system was demonstrated in [44], where a conventional winding structure of multi-layer and multi-turn was used for achieving a PTE of more than 80% within the distance range from 10 mm to 20 mm. In [164], 3-coil resonant coupling system exhibits a comparable PTE over its 4-coil counterpart, and shows a reduced sensitivity to the transfer distance. The transfer efficiencies through two different transmission mediums (air and tissue) were compared by using two printed spiral coils, and maximum efficiencies of 75% and 58% over air and tissue at distance of 10 mm were achieved, respectively [162]. A novel winding design using a pair of printed spiral coils (PSC) for inductive power transfer was investigated in [165], achieving a maximum PTE of 85.8% at an operating frequency of 5 MHz over a coupling distance of 10 mm. For the implantable applications, the PTE is limited by the coils' geometries. In this case, achieving a peak Q -factor at each coil is another effective approach to improve the PTE. In an optimized R-WPT system, the coil circuit needs to be carefully designed in terms of the capacitance and the inductance, which is capable of obtaining a peak Q -factor on each coil at the resonant frequency. Moreover, the selection of the resonance frequency should obey the industrial, scientific and medical (ISM) standard.

1.6 Biological issues

Although microsystems-based implantable drug delivery devices can be fabricated aseptically and encapsulated hermetically [31], the reliability of the implants and the

biocompatibility of the component materials are still questioned for *in-vivo* applications due to tissue inflammation [166], foreign body response [167] and biofouling [168, 169]. Surgical implantation may injure the tissue, which causes an inflammatory response [170], and the continual presence of the implant also prolongs the inflammation. Foreign body response is a body's natural response to the existence of the implanted devices, generating a coat of fibrous capsules on the implants [171], that prevents the interactions between the device and surrounding tissue [170-172]. This cellular encapsulation can be treated as a kind of physiological barrier for sealing the device; accordingly, the *in-vivo* functional performance, such as, the transportation of the drug and the diffusion of analytes (glucose, lactate, *etc.*) to biosensors degrades, thereby fouling the implants with proteins and cells. An example of the biofouling-induced sensing reduction was reported in [167] where the permeability of a glucose sensor dropped to about 50%.

Recently, a common approach to reduce the inflammatory response and suppress fibrotic encapsulation is releasing a variety of biological response modifiers (BRMs). Usually, the BRMs are enclosed within the biodegradable microspheres with biocompatible and anti-biofouling properties [170, 172]. Poly (lactic-co-glycolic acid) (PLGA) is a material widely used for microsphere fabrication [173, 174]. The BRMs loaded into the microspheres include anti-inflammatory dexamethasone [175], growth factors (such as VEGF in [176, 177]), and vasodilator agents (for example nitric oxide in [178]). A change in pH, ionic strength or electrical stimulus can trigger the degradation of the micro-containers, resulting in a consistent BRMs release to the tissue surrounding the implantable devices [170, 172]. Antifouling coating is also a useful approach to enhance the biocompatibility of the

implantable devices and reduce biofouling. The typical materials for fabricating an antifouling membrane involve Nafion [179, 180], hyaluronic acid [181], humic acids [182], phosphorylcholine [183], and polyvinyl alcohol hydrogels [170]. Nano-composite coating is a new development, using carbon nanotubes [184, 185] or silica nano-particles [186] embedded in a polymer matrix for isolating the biofouling.

For implantable drug delivery systems, both BRM release and an anti-fouling coating can be used to suppress the inflammatory response and the foreign body response [166]. For example, the release of dexamethasone loaded PLGA microspheres was demonstrated in [175] as a suitable and useful approach for mitigating the implantation induced inflammation and foreign body response. A variety of nano-porous inorganic coatings using aluminum oxide, titanium oxide and porous silicon on implantable devices were reviewed in [187]. The implantable drug delivery device's reliability can be improved and its lifetime can be extended as long as the anti-biofouling agent is continuously present around the implant. Moreover, any micro-fabrication materials for implantable devices intended for long-term *in-vivo* drug delivery applications must possess strict biocompatibility and bio-stability. The biocompatibility and biofouling of the materials that fabricated an electro-chemically activated implantable device in [62] was evaluated in [188]. The system component materials including gold, silicon, silicon nitride, silicon dioxide and SU-8TM photoresist, exhibit a statistically less inflammatory response and a reduced biofouling by measuring leukocyte concentrations and foreign body giant cells (FBGCs) in the subcutaneous tissue of a rodent model over 21 days. Titanium (Ti) has been successfully used for many orthopedic implants [31]. In our work, the key components of the drug delivery system involving silicon

substrate, PDMS membrane, PMMA drug reservoir, Pt/Ti electrodes and Pt coated carbon fiber mesh are biocompatible materials [189].

1.7 Dissertation Organization and Contributions

This dissertation presents an effective pumping and valving mechanism, and an accurate dose control approach joined together with a novel R-WPT design. As a whole, they form a “remotely operated” drug delivery device for long-term application. Here is the summary of each chapter and its major research contributions:

- Chapter 2 investigates the first combination of the SDR approach with the electrolytic pump, consequently creating a novel actuation mechanism based on the cyclical operation mode. The electrolytic pump delivers the drug at the actuation phase, while it draws fresh liquid to the drug reservoir when the power is removed. The solid drug is dissolved during each non-actuation interval, forming a reproducible drug dose. Moreover, an easily fabricated catalytic reformer is added in the electrolyte chamber to accelerate the electrolysis-bubble recombination rate and to reduce the non-actuation interval. This process decreases the period of each drug delivery cycle, which leads to an increased number of drug delivery cycles and a wider dose range within a given treatment period.
- In Chapter 3, the electrolytic pump and a thermo-responsive hydrogel valve are integrated, which function differently yet share the same electromagnetic field. A thermo-responsive hydrogel called “Poly (N-Isopropylacrylamide)” was first used to control the exit port of the pump in order to avoid undesired liquid diffusion between

drug solution and human liquid. It also allows the reverse flow that refills the drug reservoir within a given opening time. When the electromagnetic field is turned on, the electrolytic reaction happens, driving the drug liquid towards the valve. In the meantime, the heat generated by the iron micro-particles that are embedded into PNIPAM hydrogel causes the PNIPAM to shrink, resulting in an open valve. When the electromagnetic field is turned off, the fresh liquid outside the device refills the drug reservoir before the valve is closed. As the catalytic reformer is employed, more liquid can refill the reservoir within the valve's limited closing time.

- In Chapter 4, an efficient and implantation-friendly design of R-WPT technology is introduced. The R-WPT system is set up, using 3 inductive coils and capacitors to form a circuit model with the same resonant frequency that strictly follows the ISM standard. A novel single layer of inductor coil windings in a pancake configuration is designed in order to obtain a compact and flexible structure for implantable electronic applications and provide a high PTE. Using our R-WPT system, we further add a voltage control unit that is capable of obtaining a constant voltage output for the electrolytic actuator, thereby controlling the drug release rate and dose. Within the effective transfer distance and rotation angles between power transmitter and receiver, the drug release is predictable and well-defined without extra physical and chemical sensors. Moreover, the flow rate or drug release rate can be adjusted by connecting different loads with the pump before implantation. This integration exhibits an easily operated “open loop” dose control approach for drug delivery systems.

Chapter 2 Cyclically Actuated Electrolytic Actuator

This chapter, focusing on an implantable drug delivery system, presents the first prototype electrolytic pump that combines a SDR approach, a cyclically actuated mode and a catalytic reformer. The drug delivery device is actuated using the bubbles formed during electrolysis. It has many features that are different than conventional drug delivery approaches: it is capable of pumping periodically and being refilled automatically; it features drug release control; and it enables targeted delivery. These features improve the release performance and extend the lifetime of the device. The SDR approach is to deliver pulsed doses of a low solubility drug by pulling bodily fluid into a reservoir with the drug in solid-form, allowing the drug to dissolve to its maximum concentration, and then ejecting the drug solution back into the tissue. The cyclical actuation of the pump is performed, forming a reproducible drug solution in the reservoir for long-term therapies. By periodical pulsed pumping a stable and constant drug release can be accomplished, and drug release rate is power-controlled. Using a catalytic reforming element, the cyclical mode is improved because it helps accelerate the electrolysis-bubbles recombination rate, which allows for a shorter cycling period for drug delivery. Two methods are used for fabricating the catalytic reformer: sputtering and electroplating the platinum (Pt) to a mesh-structure scaffold, for example nickel (Ni) metal foam and carbon fiber mesh, which lead to different release performances. Of these two methods, the sputtered Pt-coated Ni metal foam improves electrolysis bubble generation rate; it also has a comparable recombination rate when compared to the electroplated Pt-coated Ni metal foam. The only drawback of this catalytic reformer is that it consumes nickel scaffold. Concerning long-term applications and safety of the scaffold to human, carbon fiber mesh is

selected as scaffold rather than Ni metal foam due to its inert chemical property. The proof-of-principle drug delivery studies are conducted using the electrolytic-pump, carbon fiber mesh based catalytic reformer and solvent blue 38 as the drug substitute. The experimental results demonstrate power-controlled and pulsatile release profiles of the chemical substance, as well as the feasibility and stability of such a drug delivery device. The subchapter 2.1 investigates the prototype of the electrolytic pump and its major components' fabrication process; the subchapter 2.2 evaluates the catalytic reformers' properties in the electrolytic pump; and the catalytic reformer-assisted drug release profiles in cyclical actuation mode are demonstrated in subchapter 2.3; summary is then presented in subchapter 2.4.

2.1 Electrolytic pump

2.1.1 Electrode design and fabrication

The critical component of the electrolytic actuator is the electrolysis electrode. Regarding fabricating the electrode for electrolysis, electroplated Pt is subject to mechanical damage due to the softness of the deposited metal. A popular approach is to electrodeposit Pt-iridium (Ir) alloy to increase the mechanical stiffness [48]. It was reported that an electroplated Nafion-coated electrodes can withstand a currents of up to 8 mA without delamination [48]. An improved adhesion between substrate and Pt can also result in a robust electrode, in [216], Ti/Pt electrode kept stable during the electrolysis reactions with a driven voltage of at least 5 V, and the data in [22] confirmed that the delamination of the Ti/Pt layer on silicon substrate was not observed with a current density of up to 0.15 (the applied current is 10 mA). In this work, the electrode was sputtered onto a silicon wafer, the induced current density and applied voltage was far less than the safe limit as reported in order to avoid

delamination.

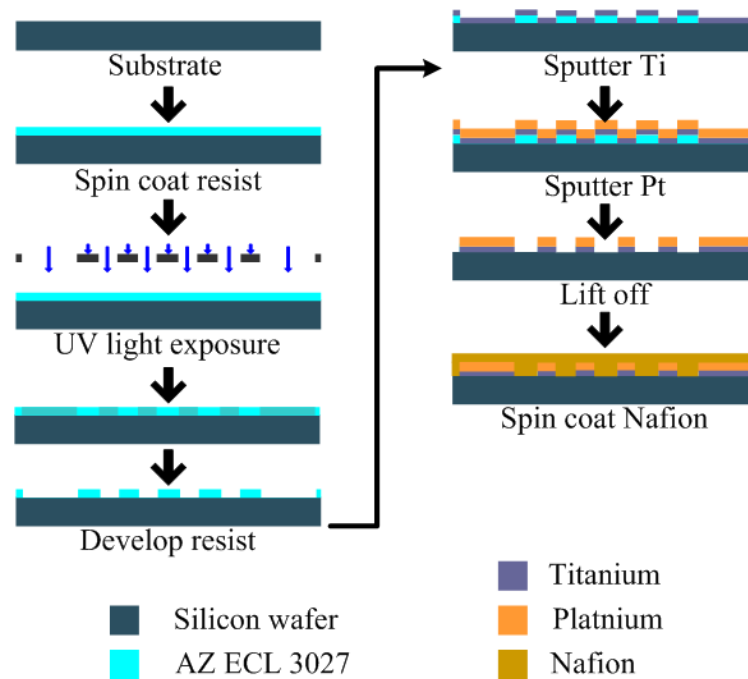


Figure 2.1 Flow diagram of electrodes fabrication process [J1].

The electrode was fabricated following the standard MEMS fabrication technology. The fabrication process of the electrodes (see Figure 2.1) started with a previously polished silicon wafer. AZ 3027 (AZ Electronic Materials) photoresist was spin-coated on the silicon wafer in three steps (1000 rpm for 3 seconds, then 1500 rpm for 3 seconds, and 3000 rpm for 30 seconds) and then the wafer was prebaked at 100°C on a hotplate for 60 seconds. The standard photolithography process was followed using a previously designed mask. Next, the wafer was ultraviolet (UV) exposed, and the exposed photoresist was developed with AZ 726 MIF developer (AZ Electronic Materials, USA). In order to ensure that the exposed photoresist was completely removed, the wafer with the remaining photoresist coating was treated with oxygen plasma for 1 minute. Afterwards, Ti/Pt were sputtering onto the silicon

wafer, the shape of electrodes were defined during the lift-off process in acetone. Finally, the electrodes were completed by spin coating with Nafion (SIGMA-ALDRICH CO., MO, USA). The wafer was then cured at 90°C on a hotplate for 1 hour.

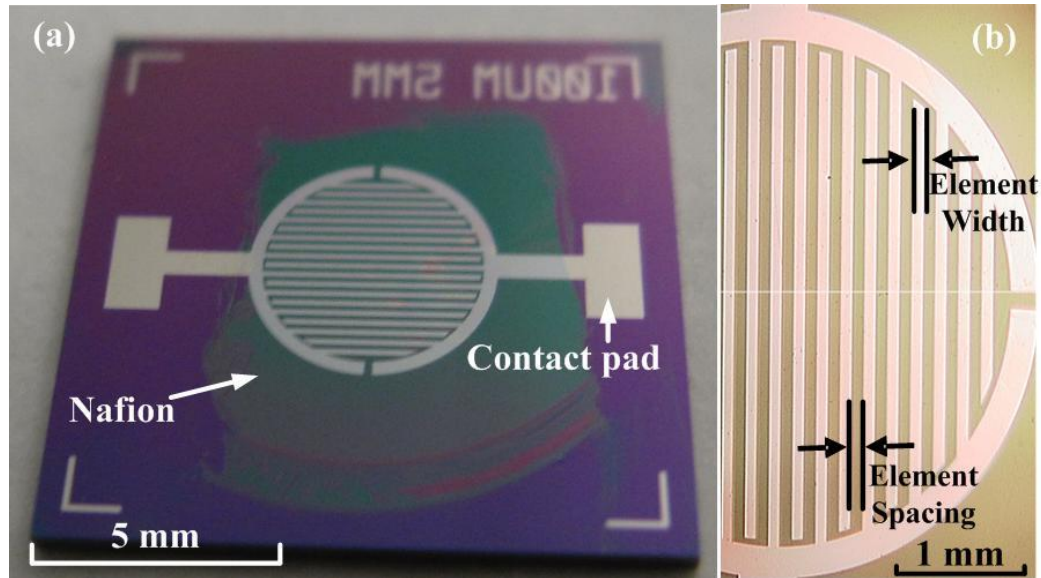


Figure 2.2 Photograph of Ti/Pt electrode design: (a) the electrodes fabricated on silicon with Nafion coating; (b) microscope of the interdigitated electrode layout showing element width and spacing [J1].

The electrode geometry (see Figure 2.2), including the electrode spacing and the element width (defined in Figure 2.2(b)), affects the efficiency of electrolytic bubble generation and pumping [22]. This interdigitated design was selected in order to reduce the resistive path through the electrolyte, contributing to an improved electrolysis efficiency and a lower heat generation [190]. The dimensional parameters were based on the optimal electrode layout: 100 μm in width with 100 μm spacing [48]. The electrodes have a height of 300 nm (thickness: Ti/Pt=1:5), and a radius of 2.5 mm. Herein, Ti was used to enhance adhesion between Pt and silicon. Pt was chosen as the electrode material due to its inert chemical properties and biocompatibility. It can prevent oxidation and corrosion during the electrolytic

reactions and acts as a catalyst for electrolysis bubble recombination [191]. Nafion was uniformly spin coated on the surface of the electrodes, this design of the electrodes was used for all subsequent experiments.

Regarding Nafion, it is a solid polymer electrolyte, which has been developed by DuPont, its chemical structure and properties were demonstrated in [192]. The solid phase and the aqueous phase of Nafion are both permeable to gases [193, 194]. Nafion possesses high gas solubility and protects the electrodes from damage caused by high current electrolysis [48, 195]. During the electrolytic reaction, the generated bubble may occlude the active electrode surface and isolate the electrode from the electrolyte, resulting in reduced electrolysis efficiency. Using a Nafion coating, the bubble occlusion can be avoided, as it allows rapid diffusion of the gases away from the electrode surface. Therefore, contact area between electrodes and electrolyte is increased, which in turn reduces heat production and improves electrolysis efficiency. Moreover, Nafion has been proven as a biocompatible material [192] due to its chemical and biological inertness [196]. In this work, Nafion was used in order to improve the electrolysis efficiency.

Mass transport can influence an electrolysis reaction. Take an example of electrolysis of water here, water can be electrolyzed into oxygen and hydrogen, the gases in the vicinity of the electrode will become supersaturated during electrolysis, because oxygen and hydrogen have low solubility and small diffusion coefficient in water. At low applied current, the dissolved gas remains in the electrolyte and diffuses to the bulk electrolyte slowly. Consequently, the supersaturation state near the electrode keeps constant. With an increasing

current, the supersaturation will exceed the value required for bubble formation. Once the Archimedes' force is greater than the surface adhesion force on the bubble [217], the bubble detaches from the electrode. The generation rate is controlled by mass transfer of gases [218] and is proportional to the square root of "current on" time [219].

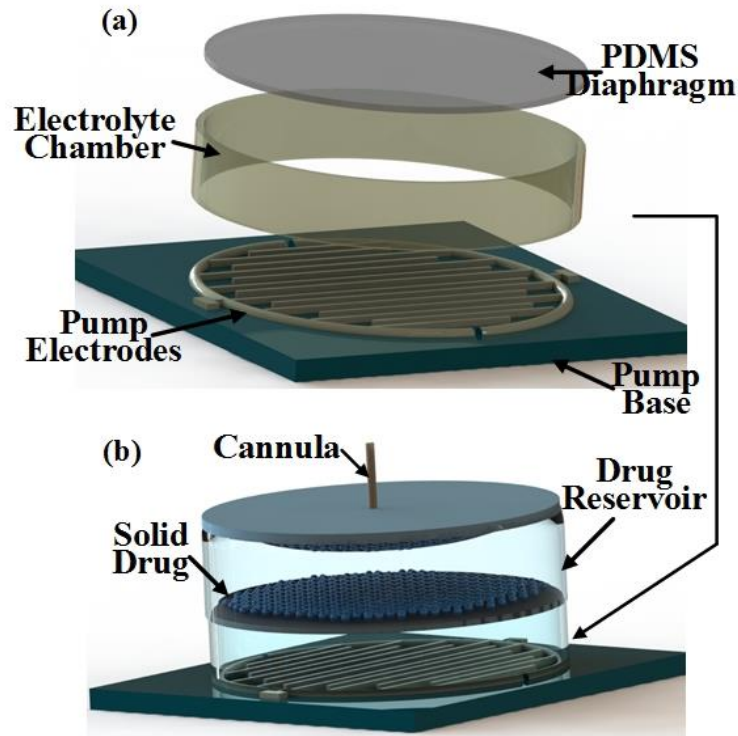


Figure 2.3 Exploded diagram of the electrolytic actuator based drug delivery system including: a) the actuator with major components. b) assembled drug delivery device (reproduced from [J1]).

2.1.2 The pump's design

The major components of our electrolytic pump include: 1) a flat PDMS membrane in between an electrolyte chamber and a drug reservoir to avoid electrochemical reactions and unwanted pH changes from occurring in the drug solution; 2) an efficiency-optimized design of the Pt/Ti electrodes for electrolysis. The overall design of the pump is shown in Figure 2.3.

The pumping chamber (Figure 2.3(a)) at least consists of electrolyte and the electrodes. The electrodes should be immersed in the electrolyte filled pumping chamber before assembling the other components. The solid drug is stored in the reservoir on top of the flat PDMS membrane (Figure 2.3(b)). Once the electrolytic reaction occurs, this configuration allows the drug solution to be dispensed directly to the targeted tissue in the vicinity of the cannula outlet.

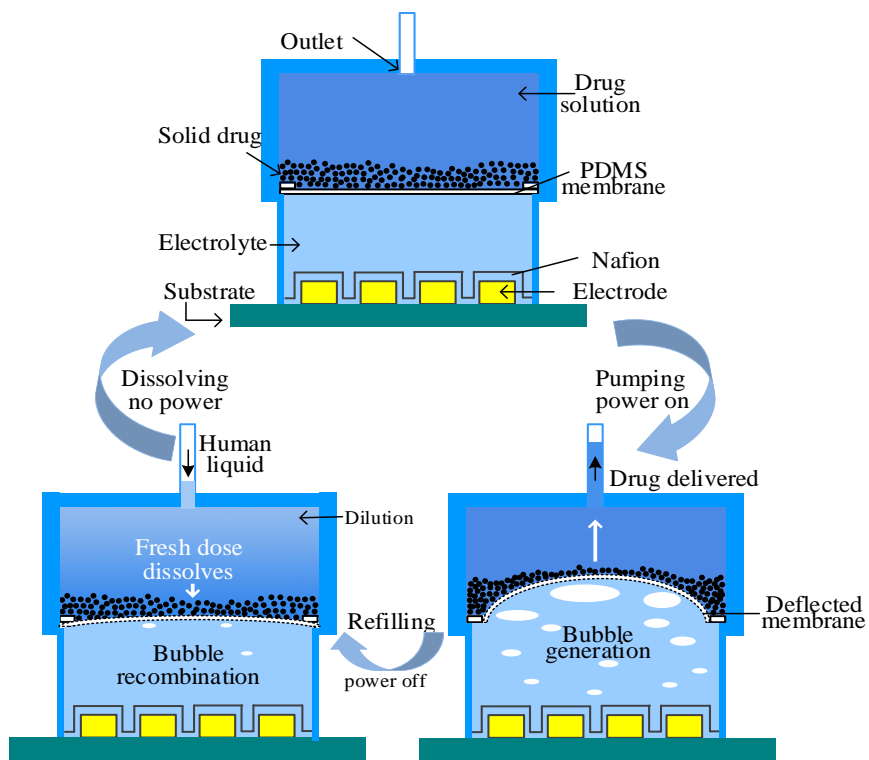


Figure 2.4 Schematic illustration of the electrolytic pump based drug delivery device and its cyclic actuation mechanism (reproduced from [J1]).

Figure 2.4 illustrates the working principle of the electrolytic pump for cyclical drug delivery. The first step is to fill the drug reservoir with DI water through the mechanically drilled channel, making the solid drug partly dissolved and prepared for delivery. Once the power is

applied to the electrodes, an electrolytic reaction starts. The generated gases (for example, DI water can be electrolyzed into hydrogen and oxygen) push the dissolved drug solution outwards due to the deflected PDMS membrane. Power must be removed prior to the membrane reaching its maximum displacement. Unlike bellow membranes [22], flat membranes are easily fabricated, however, at cost of a relatively small displacement at each pumping cycle. With or without applied power, the electrolysis-induced gases may be recombined in the presence of a catalyst. For example, DI water is used as electrolyte in this work, and the recombination of hydrogen (H_2) and oxygen (O_2) is assisted by the catalytic properties of the Pt. Pressure decrease in the electrolyte chamber causes the membrane to move downward, sucking external liquid into the drug reservoir to dissolve the rest of the solid-form drug. By repeatedly turning on and off the power, the solid drug can be dissolved and delivered cyclically.

Note that the selection of the solid drug is critical for cyclically actuated drug delivery devices that adopt an SDR approach. The basic requirement is that the storage is primarily in solid-form of which a small portion is dissolved for each successive dose. To ensure that only a small portion is dissolved in each pumping cycle a low solubility drug is required. A highly soluble drug will be consumed within only a few cycles and dose control will revert back to fine volumetric control like an LDR system which has been widely studied already. While in an SDR system, overall daily dose is controlled by the number of the actuation cycles, the actuation period, and the wattage of applied power, which will be demonstrated in the following subsections.

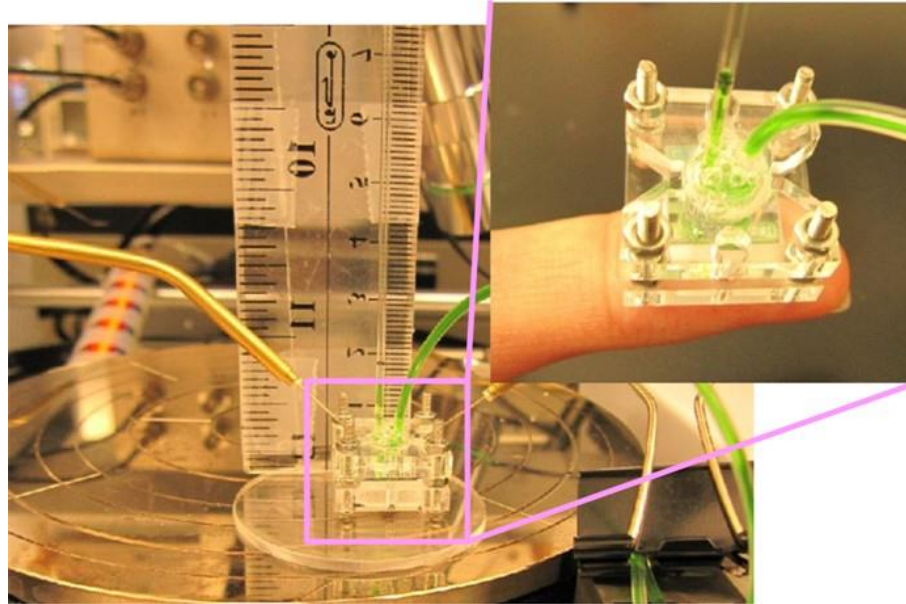


Figure 2.5 Photograph of the experimental setup and structure of electrolytic pump [C1].

2.1.3 The pump's fabrication and performance

Adopting the electrolysis electrodes as shown in Figure 2.2, the pump was mounted and evaluated using a test fixture as shown in Figure 2.5. The electrolysis electrodes are immersed in the deionized (DI) water filled pumping chamber before assembling the other components. The voltage is applied to the electrodes via the probes, bubbles are generated, pressurizing the bottom chamber and pushing the membrane upwards, so that the liquid in the reservoir climbs up the glass capillary. When the power is turned off, the generated gases (H_2 and O_2) in the electrolyte chamber slowly recombine into water, assisted by the catalytic properties of the Pt electrodes. This recombination reduces the pressure in the pumping chamber and the membrane moves downwards drawing the liquid towards the top reservoir. For easy prototype testing a cannula is replaced by an inlet and outlet tube, which can be mechanically clamped, as shown in Figure 2.5. To characterize the pumped flow rate and the reversible electrolytic reaction, the movement of green food coloring dye flowing through the

glass capillary was tracked at different applied power. A computer controlled DC power source measure unit (National Instruments PXI) was applied to the pump through two probes contacting the contact pads of the electrodes. A digital camera was placed in front of the setup to record the displacement rate of green food coloring dye.

The inset of Figure 2.5 depicts that the electrolyte chamber and the drug reservoir were assembled by tightening the polymethylmethacrylate (PMMA) holders. For the experimental measurements, the dimension of the PMMA holder is 2cm : 2cm : 2cm (length : width : height). In prospective drug delivery applications, the pump could be permanently bonded allowing the size of the structure to be significantly reduced. The drug reservoir and holder were made from a 6.2 mm thick PMMA sheet (Moden Glas Acrylic Co., Ltd) using a CO₂ laser (Universal PLS6.75) cutter; the reservoir has internal dimensions of 2.5 mm in radius and 3.0 mm in depth, providing a maximum storage of 60 μ L. A PMMA ring with a 2.7 mm height cut by the CO₂ laser was used as the pumping chamber; the dimensions were an inner radius of 2.5 mm and a wall thickness of 0.6 mm.

To fabricate an elastic membrane, we first prepared PDMS (Dow Corning Sylgard 184) with a mixing ratio of 10:1 (pre-polymer to cross-linker). It was then spin-coated on a buffered oxide etched (BoE) silicon wafer after degassing, cured at 90°C on a hot plate, and then laser-cut into a round shape with a radius of about 3.2 mm. The height is 8 μ m, this measurement was taken with a profilometer (Ambios Technology Inc., CA). Finally, the PDMS was peeled away from the wafer to form the membrane that we used in this work. Because the PDMS membrane can fully cover both the pumping chamber and the drug reservoir, the entire pump

can be sealed during assembly by tightening the fasteners. We observed no outward leakage, nor any dyed water in the pumping chamber, thereby suggesting a completely sealed pump had been assembled. Though the PDMS membrane is gas permeable, this does not affect the actuation performance within a relatively short operation time. For the long term application, the easiest solution to this possibility is to coat Parylene C on the PDMS membrane or use another barrier film in order to avoid gas leakage and diffusion between the pumping and reservoir chambers.

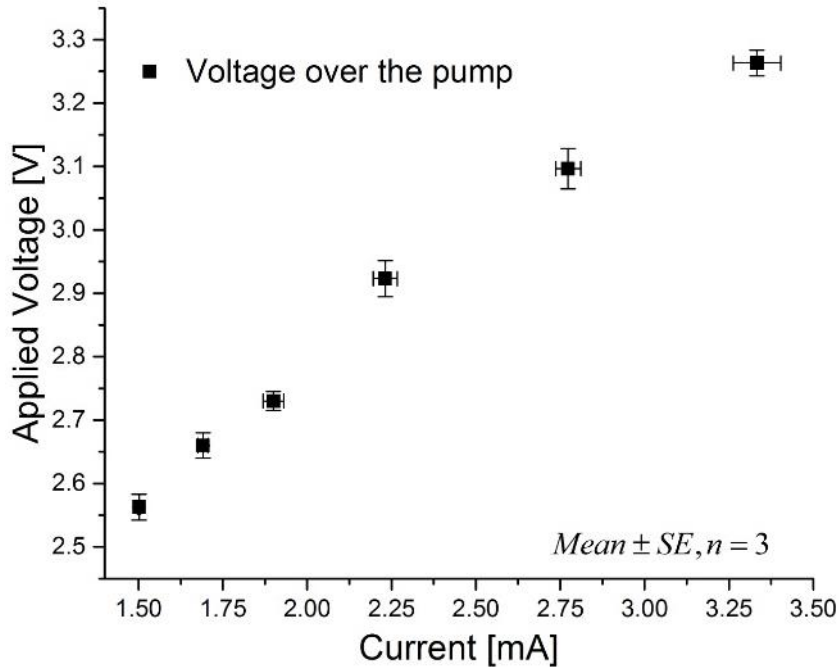


Figure 2.6 Electrolytic pump's I - V property [J2].

Nafion was uniformly spin-coated onto electrodes in three steps (600 rpm for 1 second, then 800 rpm for 3 seconds, and 1500 rpm for 60 seconds) in this work and cured at 90°C on a hotplate for 1 hour, forming a 235 nm thin film. In order to demonstrate the impedance of the electrolytic pump, the I - V curve of the electrodes with Nafion coating was measured as

shown in Figure 2.6. The DC power source (National Instruments PXI) provides DC voltage output, the current passing through the pump can be measured accordingly. The impedance of the pump varies according to the applied voltage, in the other words, the current does not increase linearly with the applied voltage. In this dissertation, the power (the multiplication of the current and voltage) is adopted as the X-axis in the following figures, because the end goal is to use wireless power transfer and the value of interest is the power requirement.

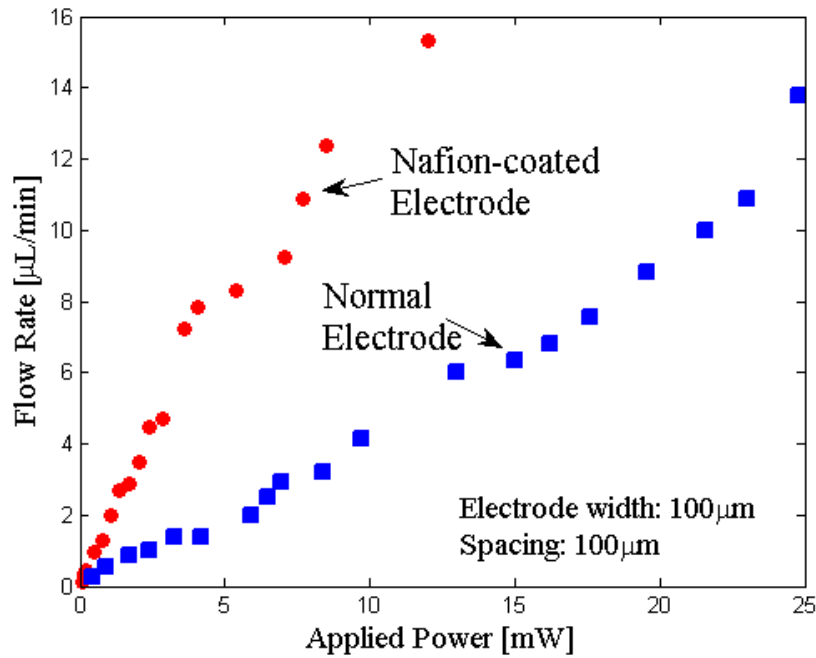


Figure 2.7 Electrolytic pump flow rate vs. applied power for both Nafion coated and uncoated electrodes [C1].

Figure 2.7 represents the flow rates of Nafion-coated electrodes compared to untreated electrodes over different applied powers ranges using the same apparatus. By adjusting the applied power, the flow rate can be controlled accordingly; the higher power he applied, the faster the flow rate becomes. Moreover, we can observe that Nafion coating of the electrode to significantly improve the electrolysis efficiency, which had been previously reported by

Meng's group as well [48].

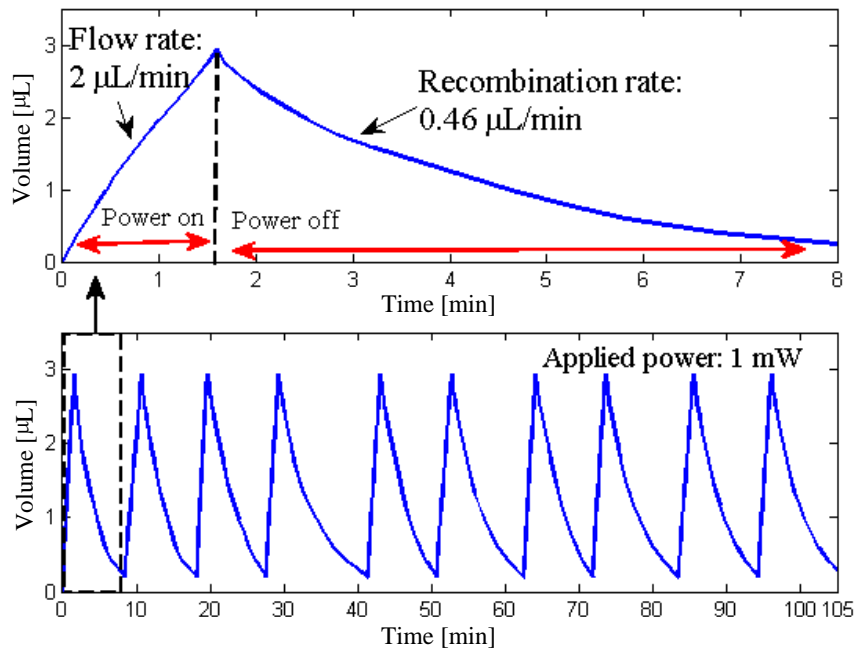


Figure 2.8 Periodical pumping pulses show behaviors of electrolytic bubble and gas recombination [C1].

Because our system requires cyclical actuation to operate, we tested the reverse flow rate during gas recombination, as shown in Figure 2.8. An electrolytic pump with Nafion coated Pt electrodes alone can recombine approximate 2.7 µL of gas in about 6.4 minutes, though still remaining a small portion of un-recombined gas within such an interval. The negative slope of the displacement curve is primarily dependent on the surface area of the bubbles in contact with the platinum electrode. The bottom plot of Figure 2.8 also illustrates a periodic stable pumping pulse, with relatively low power consumption of 1 mW that definitely can be obtained via a wireless power transfer technique [164]. Besides the flow rate which can be controlled by the applied power, as indicated in Figure 2.7, the bubble recombination rate is another factor that determines the number of delivery cycles and the amount of drug released

within a given operation period. Our device allows for controllable flow rates as well as an “on-demand” actuation frequency. In order to further accelerate the bubble recombination rate and increase the number of the delivery cycles within a limited treatment period to address the patient’s needs, adding a catalytic reformer is a reasonable approach.

The experimental apparatus was set up for measuring the amount of drug released per cycle. We used solvent blue 38 (SIGMA-ALDRICH CO., MO, USA) as solid drug substitute, because it has relatively low solubility in water (approximate $1 \mu\text{g}/\mu\text{L}$ in water at room temperature) and it can be easily measured via detection equipment, such as Picodrop Pico200 microliter spectrophotometry (Picodrop Ltd., UK). We put 3 mg of solvent blue 38 on top of the PDMS membrane in advance and then assembled the electrolytic pump. At the outlet of the pump, we placed a small reservoir with a volume of $5 \mu\text{L}$, and carefully injected DI water in the drug reservoir through a laser-drilled inlet, ensuring that the DI water did not leak out to the external reservoir. Then the inlet was clamped, in this case, the laser-drilled outlet is the only channel used for pumping and refilling. Solvent blue 38 is partly dissolved in the reservoir at the initial stage and the rest remains stored in powder-form.

In this experiment, we applied the power of 1 mW to the pump, and the actuation time was 1 minute for each delivery. Extracting the pumped fluid in external reservoir by using a pipette, we determined the amount of the delivered drug by measuring the concentration of the liquid in the pipette via the spectrophotometry. The drug reservoir was then refilled with fresh water for the next measurement. The extracted doses were quantified and show a stable value of approximately $2\mu\text{g}/\text{dose}$ over 7 doses as depicted in Figure 2.9. This is because the

concentration of the pumped liquid is close to its maximum solubility during the pumping period, and new drug can be dissolved within the non-actuation interval, returning to saturation. Moreover, owing to a low solubility of the drug, the solid state can be maintained in a drug reservoir for an extended period, which allows for long-term drug delivery.

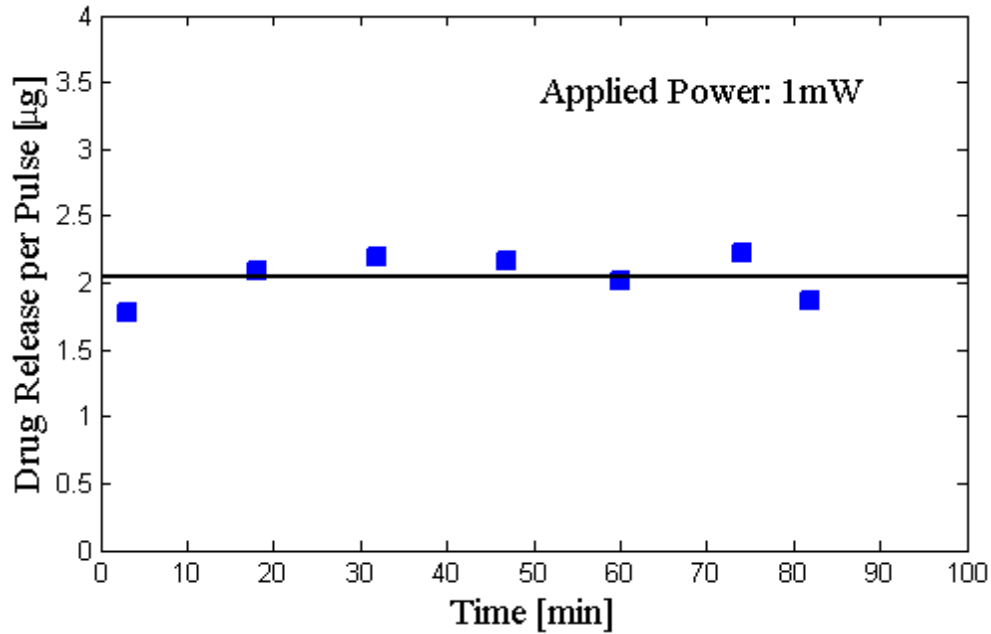


Figure 2.9 The dose of released drug per pulse under the applied power of 1mW [C1].

In summary, the power-controlled and pulsatile circulating release of a drug substitute with low solubility in a reproducible manner was investigated in this subsection. A cyclically pulsed device was integrated the electrolytic pump with the SDR approach which intended to provide long term dosage and simple control. In this device, an applied DC voltage triggers the electrolytic reaction, inducing bubble generation in the electrolyte chamber. The pressure increase deforms a flat PDMS membrane that is in between the pumping chamber and the drug reservoir, discharging the drug solution out of the reservoir. When power is removed,

the fresh liquid automatically refills the reservoir to dissolve more of the remaining solid-form drug due to pressure decrease in the electrolyte chamber. However, a flat membrane cannot achieve a displacement over its maximum safe deflection, limiting the dosing at each pumping. The un-recombined gases in the electrolyte chamber also reduce the pumped volume during the subsequent actuations and eventually deplete the drug solution cycle by cycle. Therefore, in order to improve the pump's delivery performance and achieve "on demand" drug release over a long period, the ability to improve the number of drug delivery cycles within a given treatment period must be developed.

2.2 Catalytic reformer

Improving on the work demonstrated above, an easily fabricated catalytic reformer is added for accelerating the bubble recombination rate, reduces the non-actuation intervals so that the time of each drug delivery cycle is decreased. In this subchapter, the catalytic reformer using different scaffold is introduced, accordingly, resulting in different catalysis performance. It is added in the electrolyte chamber in order to increase the contact area between the catalyst and electrolysis-induced gases. In this manner, bubble recombination starts immediately once the power is turned off, taking less response time than the normal electrolytic pump without a catalytic reformer. Though added catalytic reformers can increase the recombination rate, they decrease the flow rate during the actuation phase due to simultaneously occurred bubble recombination. Herein, Nafion coated Pt/Ti electrodes that lead to high current electrolysis efficiency [48] is chosen to compensate for the electrolysis efficiency reduction caused by the catalytic reformer.

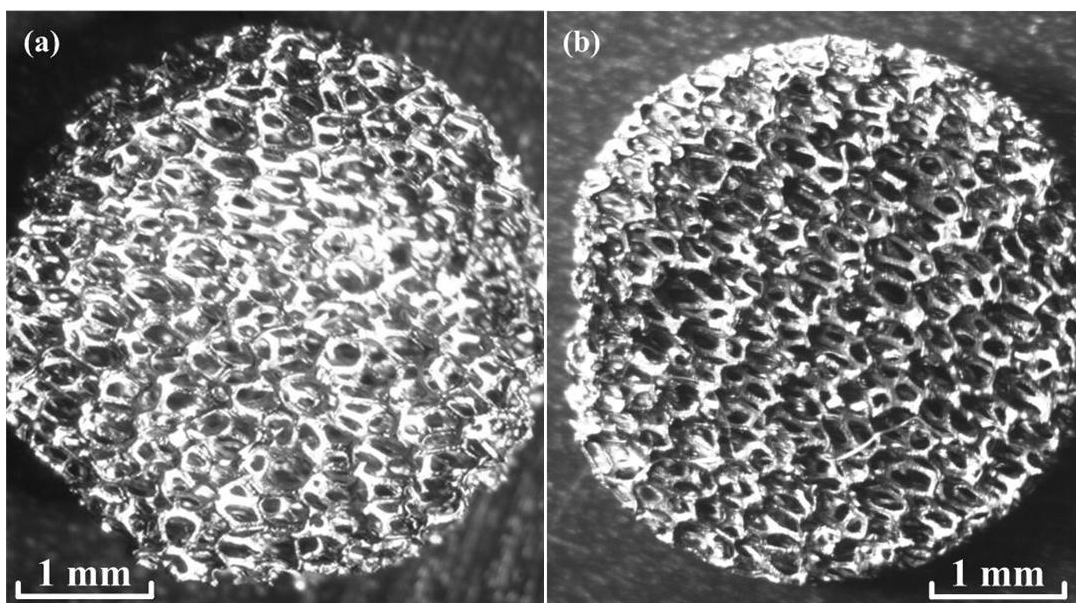


Figure 2.10 Microscope of Pt-coated nickel foam fabricated by (a) sputtering, (b) electroplating [J1].

2.2.1 Nickel foam scaffold

Herein, a nickel (Ni) foam-based catalytic reformer will be introduced, as well as its potential catalysis for drug delivery application. The prototypes of the catalytic reformers using a Ni foam as a scaffold are depicted in Figure 2.10. When fabricating this part of the device, we first cut two identical Ni metal foam sheets into a round shape that fits the electrolyte chamber by using a laser. Next, we sputter coated and electroplated the Ni metal foams with Pt using the following two methods, respectively. For the sputter process, we used a Quorum 300 DT sputtering system (Quorum Technologies Ltd., England) to sputter a Pt film on both sides of the Ni foam. The sputtering process was unable to coat the entire surface of the nickel foam with Pt and exposes the Ni to the electrolyte. The electroplating deposition, in comparison, was performed by connecting the metal foam to a potentiostat in a three-electrode cell configuration, including a reference electrode of Ag/AgCl. Pt nanoparticles were potentiostatically electrodeposited on the entire surface of the Ni metal foam.

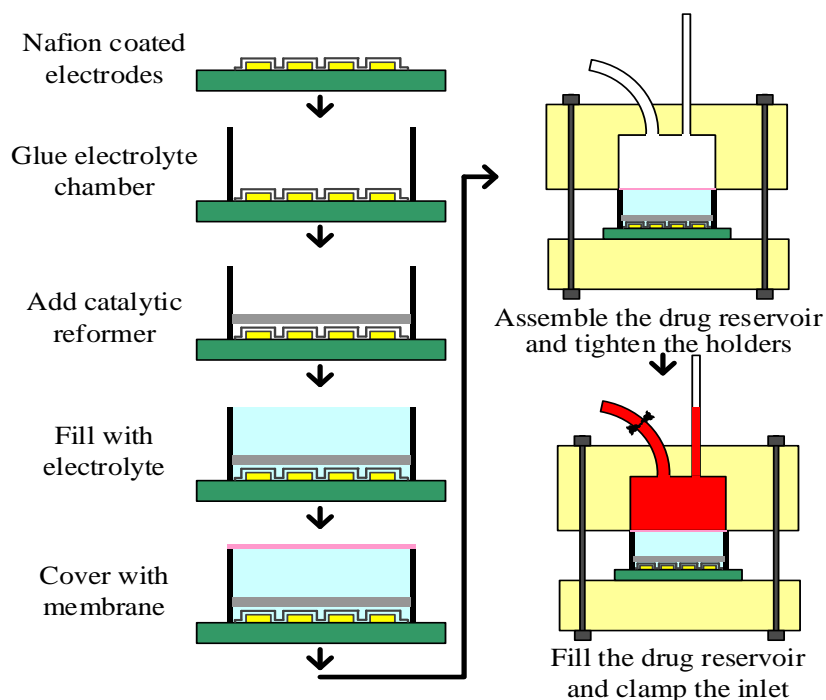


Figure 2.11 Schematic illustration of the assemble process of the electrolytic pump.

Our pump integrated with the catalytic reformer is assembled following the procedure as illustrated in Fig 2.11, and the corresponding apparatus for measurement is shown in Figure 2.12. In pumps having an independent drug reservoir (Figure 2.12b) and electrolytic actuator (Figure 2.12c), their sizes and fabrication processes were demonstrated in subsection 2.1.3. The Pt-coated metal foam fits the size of the electrolyte chamber, and it is immersed in the electrolyte. The reservoir is filled using the inlet line, which is then mechanically clamped. The PDMS membrane's deflection is used to separate the electrolyte from the drug solution, and drive the fluids. Two probes connected to the contact pads of the electrodes are used to apply a voltage to the pump.

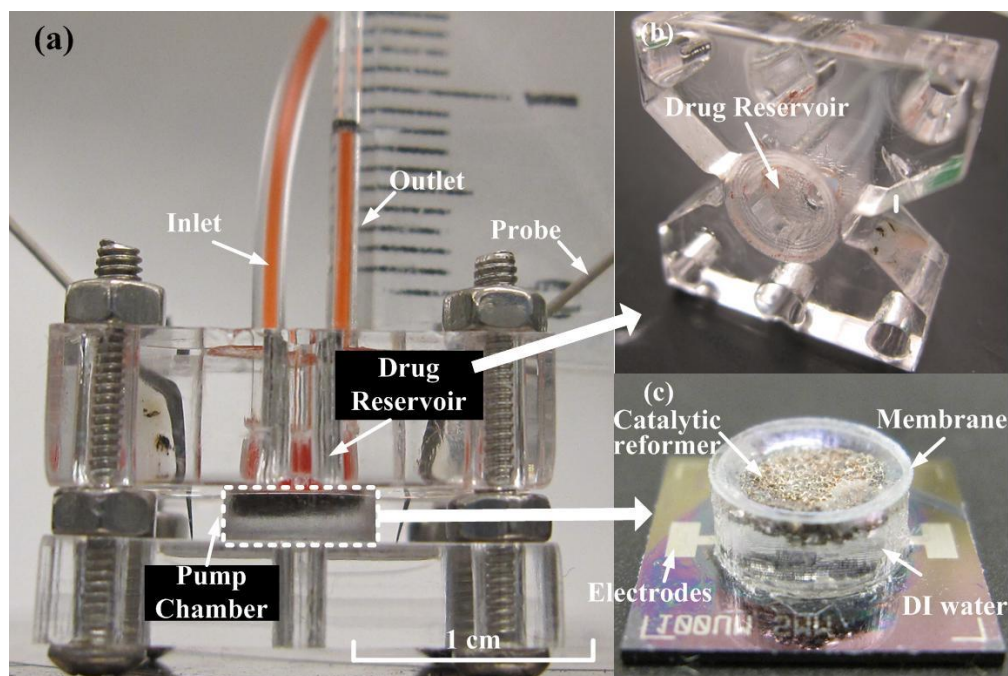
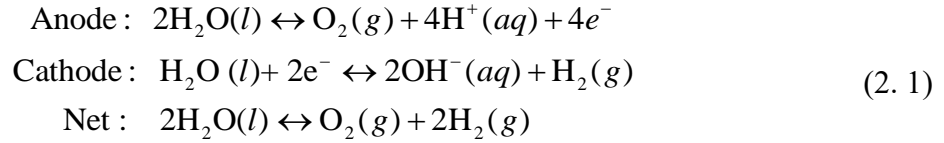


Figure 2.12 Photograph of the experimental apparatus and structure of electrolytic pump: (a) the assembled electrolytic pump for experimental measurements; (b) the photo of laser drilled-drug reservoir from PMMA board; (c) photograph of pumping chamber with a catalytic reformer and Nafion coated electrodes [J1].

When DC power is supplied to the electrodes, gases from electrolysis are generated and the resulting pressure increase in the electrolyte chamber deflects the flexible membrane upwards. The upward displacement of the liquid within the glass capillary is equivalent to the pumped volume. When the power is removed, hydrogen and oxygen start to recombine in the presence of catalyst, causing a pressure decrease in the pumping chamber and the return of the membrane to its starting position. In this manner, the volume of recombined gas or the fresh liquid that refills the reservoir can be measured by the volume change of the colored liquid in the glass capillary. The displacement can be measured using a ruler, as depicted in Figure 2.12. Dividing the displacement of the dye by the time required for the displacement yielded the flow rate.

As mentioned above, the actuation force of the electrolytic pump comes from the dissociation of DI water into hydrogen and oxygen; the corresponding electrochemical reactions are given by:



The efficiency (η) of the electrolytic reactions is defined as:

$$\eta = \frac{V_{\text{experimental}}}{V_{\text{theoretical}}} \tag{2.2}$$

where $V_{\text{experimental}}$ is the generated gas volume calculated by measurements, and $V_{\text{theoretical}}$ is the theoretical volume of the generated gas. The electrolysis-bubble generation is closely correlated to the applied current [197]. The corresponding theoretical generated volume can be calculated by [22, 48]:

$$V_{\text{theoretical}} = \left[\frac{3}{4} \frac{i}{F} V_m t \right] \tag{2.3}$$

where i is current (unit: Ampere), and t is the electrolytic time. F represents Faraday's constant (96.49×10^3 C/mol), and V_m is the molar gas volume at 25 °C (24.7×10^{-3} m³/mol). However, in the practical applications, the generated volume is affected by losses due to recombination of gases into water, dissolution of gases into the solution, and Joule heating.

In this work, the DC power source measure unit (National Instruments PXI) was used to power the pump directly. Both the applied voltage and induced current were displayed on a computer so we could calculate the applied power. Power was applied to the pump until the

PDMS membrane reached its maximum deflection. The electrolysis efficiencies of three different pump versions, run under the same experimental conditions, are shown in Figure 2.13. Current density is defined as the ratio of the current to the surface area of the electrode; it is a more specific variable that indicates the resistive path through the electrolyte, playing a major role in the electrolysis efficiency.

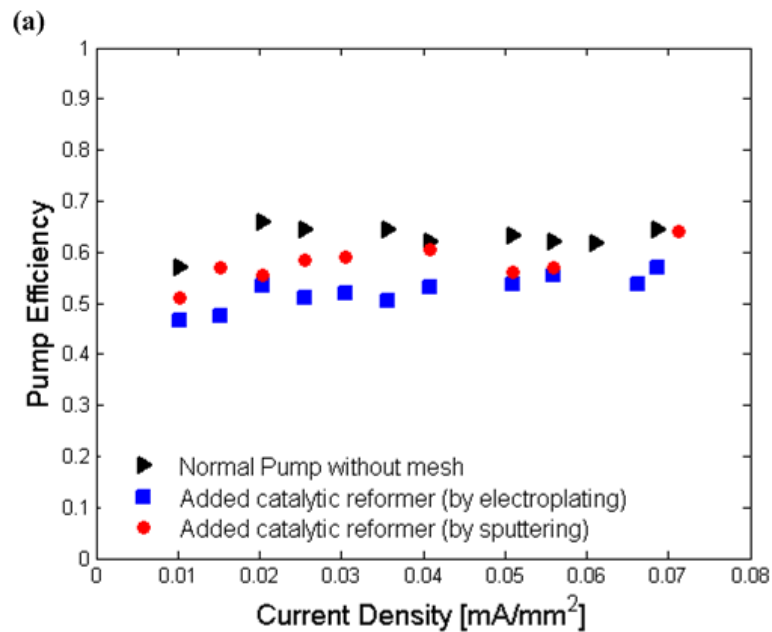


Figure 2.13 Pump efficiency comparisons between three different pump versions [J1].

Of these three pump types, one had only the optimum electrode dimensions and a Nafion coating (denoted as normal pump here), one had an added sputtered Pt metal foam, and one had an added electroplated Pt metal foam. As expected, when a catalytic reformer was added, the pumping efficiencies were lowered. This is because the added Pt-coated metal foam increases the contact area between the Pt and the formed gases, and it contributes to a recombination of bubbles that competes with the generation of bubbles from electrolysis during the pumping stage. Owing to the electroplated Pt-coated metal foam has a larger Pt

contact area than the sputtered Pt-coated foam, the former results in a lower pumping efficiency. Moreover, temperature also affects the electrolysis efficiency, because the bubble recombination that has a negative influence on bubble generation efficiency is temperature dependent. This pump was tested at room temperature ($\sim 22^{\circ}\text{C}$), however its target application is human implantation where temperature variation is limited. The variation in electrolysis within targeted body temperature range is negligible [48].

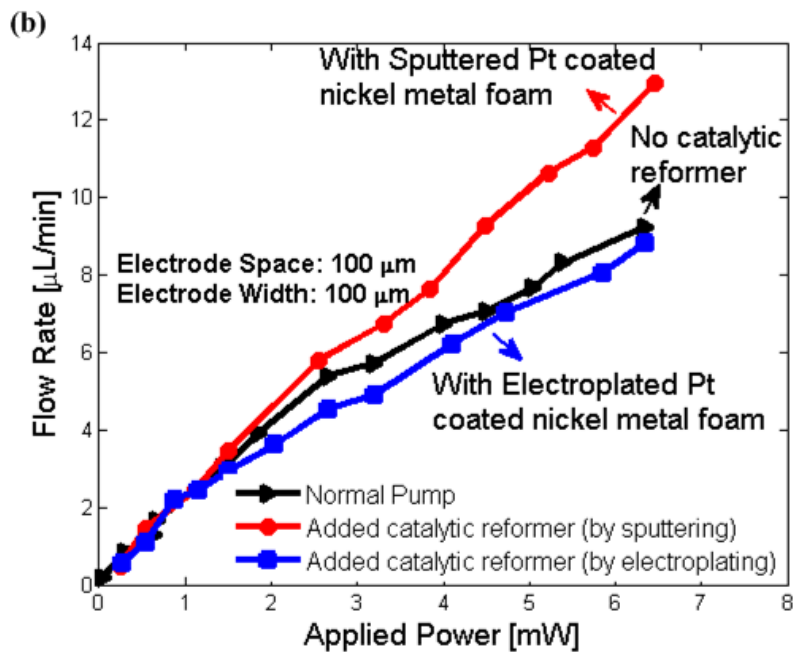


Figure 2.14 Flow rates vs. applied power for three different pump versions [J1].

A higher current generates bubbles faster from electrolysis [48, 197]. As described above, due to the increased recombination rate provided by the catalytic reformer, we should expect that both devices with a Pt coated Ni foam should have a lower flow rate for a given applied power than a device without a catalytic reformer. However, when the Ni metal foam is Pt sputter coated, some of the Ni is still exposed to the electrolyte, as Ni has higher position in

the table of electrochemical series than Pt, it dissolves as Ni^{2+} during electrolytic reactions due to galvanic corrosion. This consumption of the Ni metal foam leads to a faster flow rate as shown in Figure 2.14 due to the conductivity change of the electrolyte. Specifically, a sputtered Pt coated Ni foam increases the conductivity of the electrolyte during the electrolytic reaction. This conductivity improvement requires a lower voltage (or power) to produce the same volume of gases [105] than that of the normal pump. The electroplated Pt-coated metal foam does not have exposed Ni. Thus only the catalytic function is present, and the electrode can be stably used.

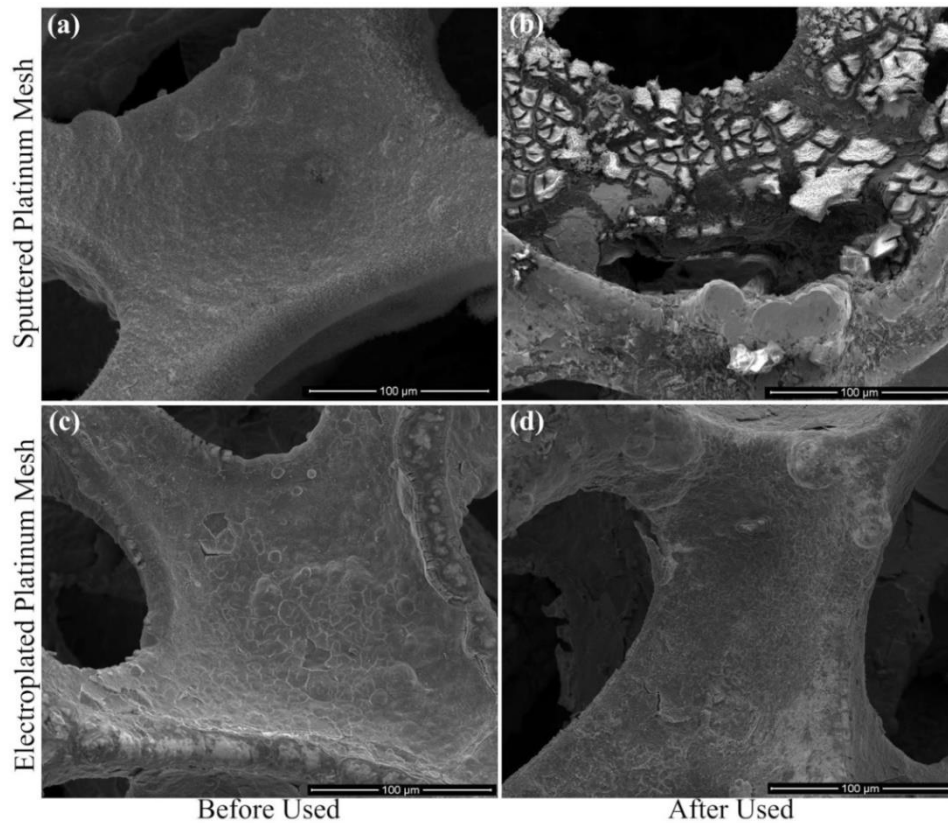


Figure 2.15 SEM images of the Pt coated Nickel mesh surface, (a)-(b) depicts the sputtered Pt mesh before and after used. (c)-(d) shows the electroplated Pt mesh before used and after used. Catalytic reformers were used for 20 actuation cycles with each actuation period of 30 seconds under a power of 4 mW [J1].

In order to verify this point, scanning electron microscope (SEM) images of the Pt-coated metal foam before and after the experiments show the difference between the damaged sputtered foam and the stable electroplated foam (see Figure 2.15). The surface of the sputtered Pt-coated metal foam suffered from severe corrosion after used for 10 minutes under an applied power of 4 mW (Figure 2.15a and b). In comparison, although the electroplated Pt-coated Ni metal foam showed a few cracks where Pt deposition was thick (Figure 2.15c), the electroplated Pt-coated metal foam showed no discernible surface change (Figure 2.15d) under the same experimental conditions.

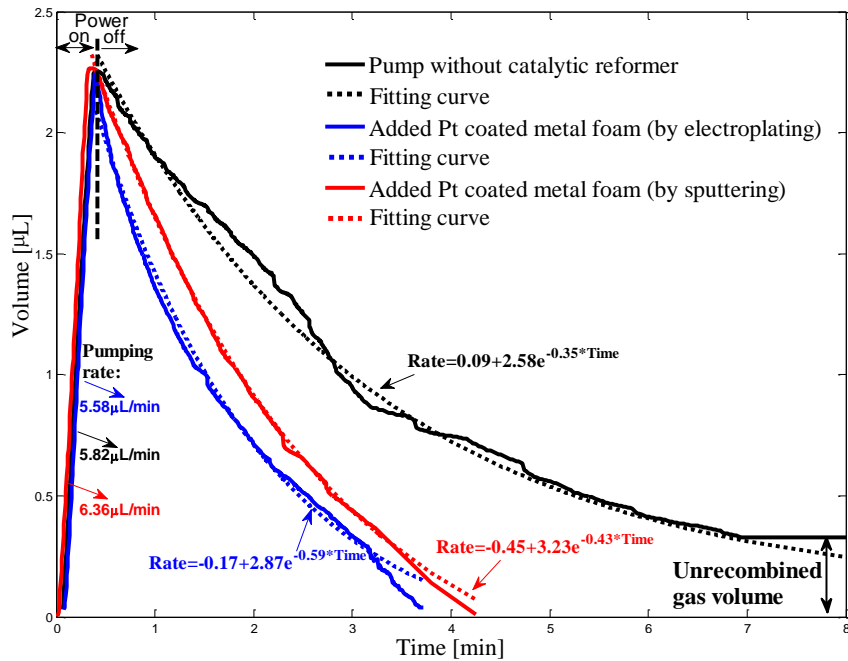


Figure 2.16 Profiles of bubble generation and recombination for three different pump versions; power of 3.7 mW was applied [J1].

To compare the pumping profiles of the three different pumps, we used Labview’s vision assistant to track the red dye flow and to measure the membrane displacement. As expected, the pumps with a catalytic reformer have accelerated recombination rates compared to the

one without a catalytic reformer as shown in Figure 2.16. Electroplated Pt-coated metal foam provides a larger rate than the sputtered Pt-coated metal foam due to its larger Pt-coated contact area.

In summary, the electrolysis bubbles take a long time to recombine [24], but the catalytic reformer greatly speeds up recombination, thus supporting more actuation cycles (doses) in a given time frame. Admitted that sputtered Pt coated Ni foam is capable of increasing both electrolysis bubble generation rate and recombination rate, which may exhibit advantages in many external biomedical devices. However, the application of Ni scaffold in implantable devices will bring concerns regarding its biocompatibility and stability, in case the Ni^{2+} liquid leaks out in the body. Therefore, changing to an inert scaffold for the catalytic reformer or directly using a pure Pt mesh would be a safer consideration.

2.2.2 Carbon fiber scaffold

The absolutely pure Pt meshes usually are not available in laboratories, so we need to find a safe and inert material for the scaffold of the catalytic reformer. From this subsection, a carbon fiber mesh based catalytic reformer will be introduced. Figure 2.17(a) illustrates the exploded view of our proposed drug delivery system, with the corresponding prototype being shown in Figure 2.17(b). This electrolytic pump was assembled following the process as demonstrated in Figure 2.11. Though the design of drug reservoir (Figure 2.17c) was slightly different than the previous one used in subsection 2.1, its fabrication process and its volume kept same. Three Pt-coated carbon fiber meshes were immersed into the pumping chamber (Figure 2.17d) to act as reforming elements in order to reduce the cycle time, which is one of

the determining factors in our system's ability to provide different dosing profiles. Interdigitated platinum/titanium (Pt/Ti) electrodes were fabricated on a silicon wafer by a standard photolithography and lift-off processes (Figure 2.17e), their detailed fabrication processes, and correlated parameters were demonstrated in subsection 2.1.

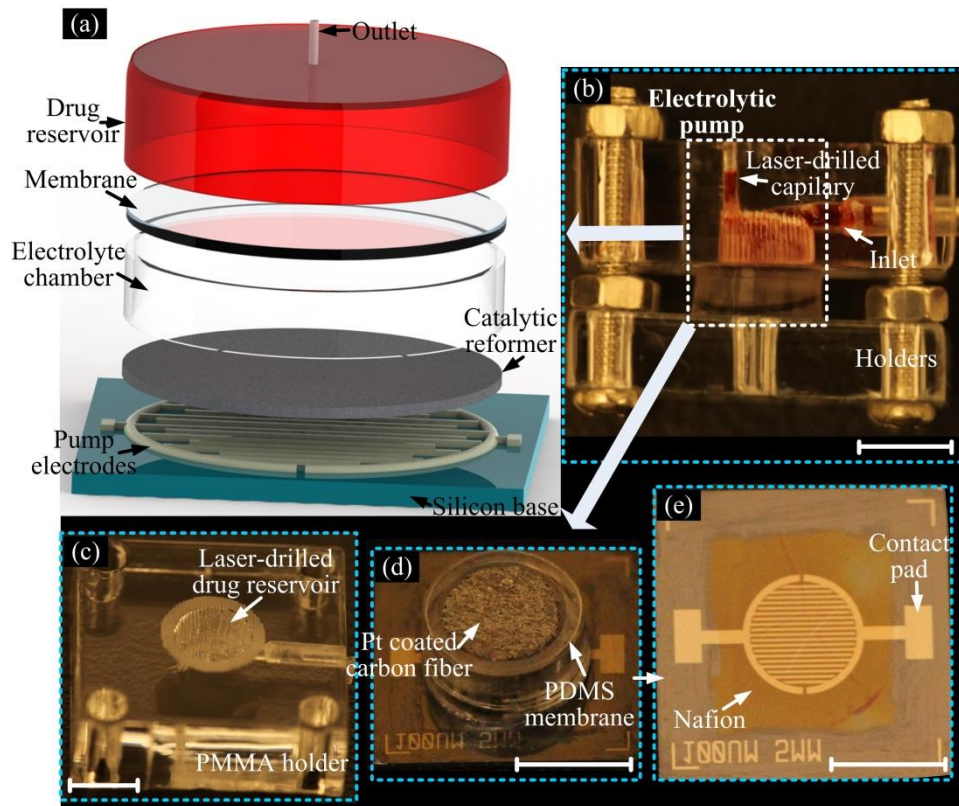


Figure 2.17 Illustration and photographs of our proposed electrolytic pump: (a) Exploded view of the device showing its major components; (b) Test fixture photo; (c) Drug reservoir cut from PMMA board; (d) Photo of assembled electrolysis actuator including Pt coated carbon fiber mesh; (e) Layout of Nafion coated Pt/Ti electrodes. The scale bars are 5 mm [J2].

SEM images of the Pt coated carbon mesh are depicted in Figure 2.18. The porous mesh structure is chosen in order to let the electrolysis-generated bubble pass through and increase the contact area. Carbon fiber mesh (porosity: 78% in this work) is selected as the scaffold because it is an inert and biocompatible material. In fabrication, we first cut three pieces of

identical meshes from a carbon fiber paper (Fuel Cell Store, Texas) with a round shape to fit the actuator chamber. Thereafter we placed them in a Quorum Q300TD sputtering system. Using a 90 mA ion current, we sputtered Pt to form a layer with an estimated thickness of 100 nm. The discs then turned around, and the same procedure was repeated again, so that both sides and the inner surface were coated with Pt. Because each piece of the mesh is very thin ($\sim 300 \mu\text{m}$), we used multiple pieces in order to further increase the Pt contact area.

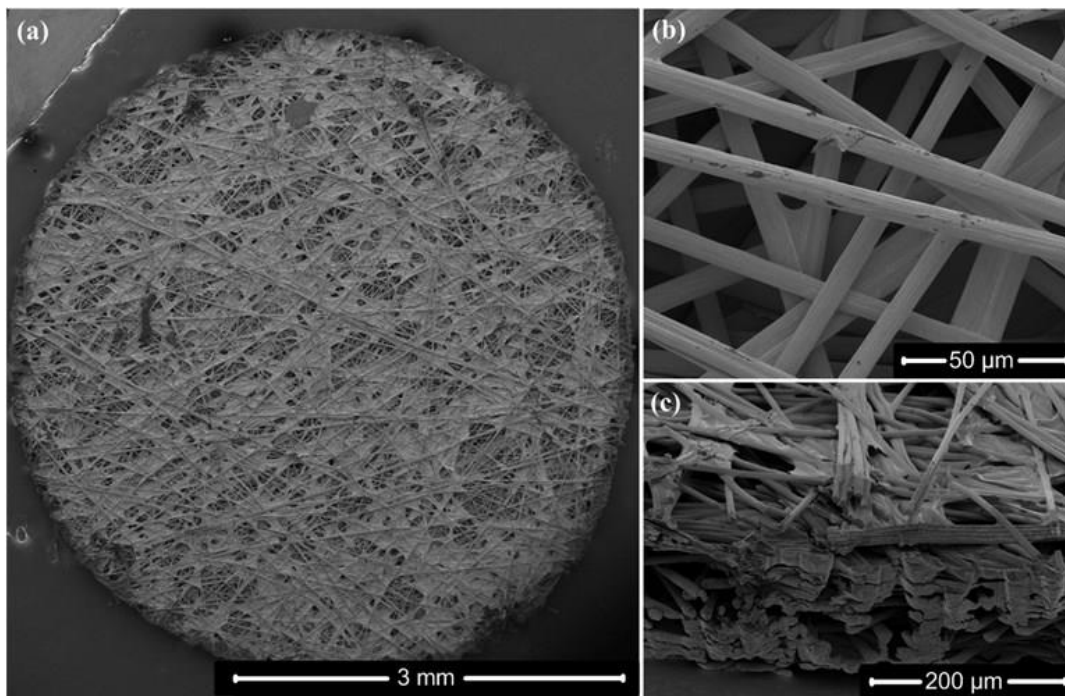


Figure 2.18 (a) Top SEM view of overall Pt coated carbon fiber mesh, showing the magnified region of the edge from (b) the top view and (c) a cross-sectional view, illustrating the details of the porous structure [J2].

As described in subsection 2.1, the working principle of our proposed drug delivery system is based on the cyclical operation including two phases: pumping at bubble generation and refilling at bubble recombination, which are implemented by “power on and off”, respectively. The catalysis performance of the Pt coated carbon fiber meshes in the cyclical

mode was tested using the same experimental apparatus as illustrated in subsection 2.2.1. Figure 2.19 shows the power controlled flow rates for two different pump versions run under the same experimental conditions: a pump with Nafion coating; and the one with an added catalytic reformer. The results indicate that the added Pt-coated carbon fiber meshes decrease the electrolysis efficiency and flow rate, because an increased Pt contact area can simultaneously recombine more gases into water even in the electrolysis-generation phase. With increasing applied power, the electrolysis bubble generation becomes faster and more dominant, so the flow rate difference between the pump with and without catalytic reformer becomes smaller.

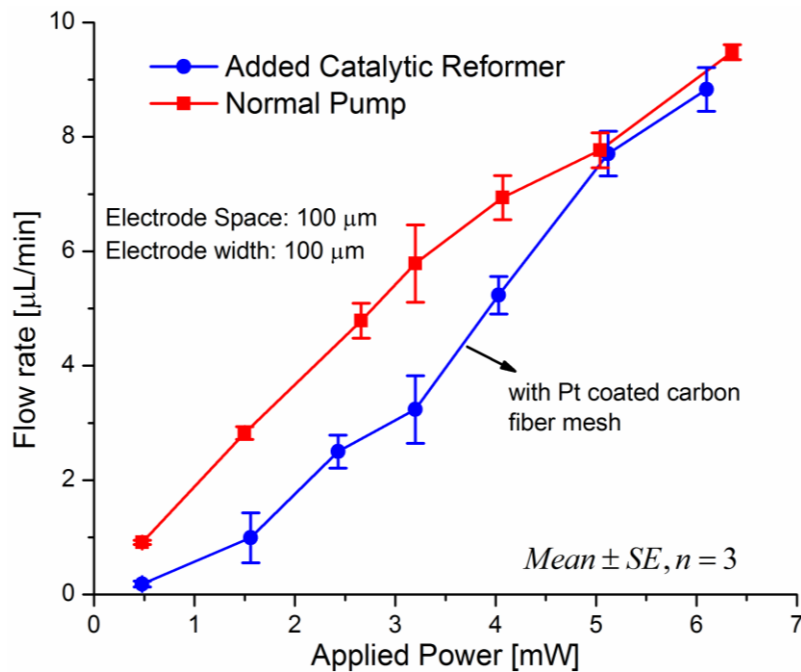


Figure 2.19 Power controlled flow rates for the electrolytic pump with and without catalytic reformer ($Mean \pm SE, n=3$) [J2].

Labview's vision assistant was used to track the red color flow in order to measure the membrane displacement. Figure 2.20 compares the displacement profiles of the two pumps

under the same applied power. As analyzed above, the pump using the Pt-coated carbon fiber meshes lowers the flow rate since it brings the effects of competitive bubble recombination. Power was applied until the pumped volume reached about 2.3 μL , and then the power was removed. The generated bubbles slowly recombined in the normal pump because it only has a Pt electrode and does not use a Pt-coated carbon fiber meshes.

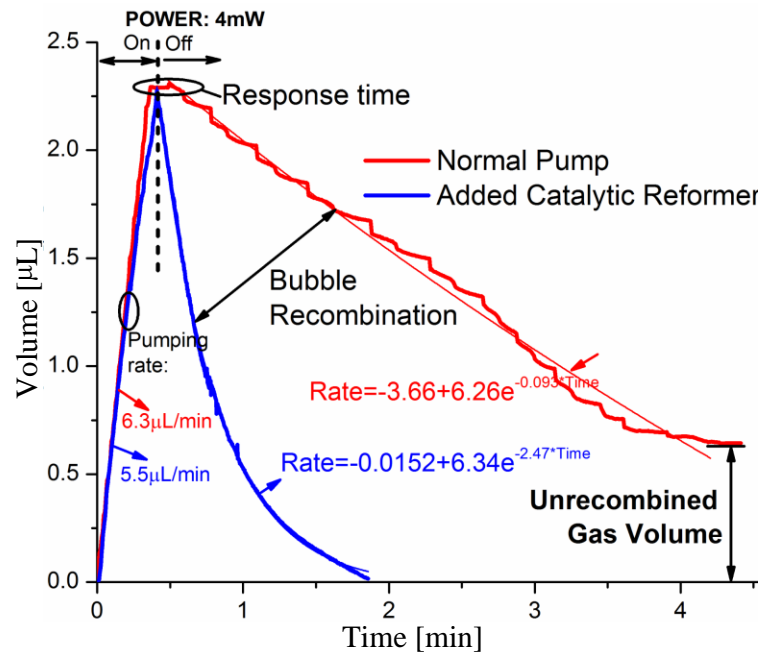


Figure 2.20 Real-time membrane displacement of the electrolytic pump with and without catalytic reformers under the same experimental conditions, power of 4 mW was applied and then removed [J2].

As shown in Figure 2.20, 72.1% of the pumped volume flows in reverse through the pipette, illustrating a significant portion of un-recombined gas [24] since the Pt contact area is too small. In comparison, using our catalytic reformers, 99.3% of the gas recombines, providing a larger membrane deflection for the next delivery. This improvement in recombination comes at a slight reduction in the efficiency during the “power on” phase as can be seen from

the lower pumping rate (blue) in Figure 2.20. However, this faster recombination rate dramatically reduces the period of each cycle, exhibiting a great improvement in cyclical mode.

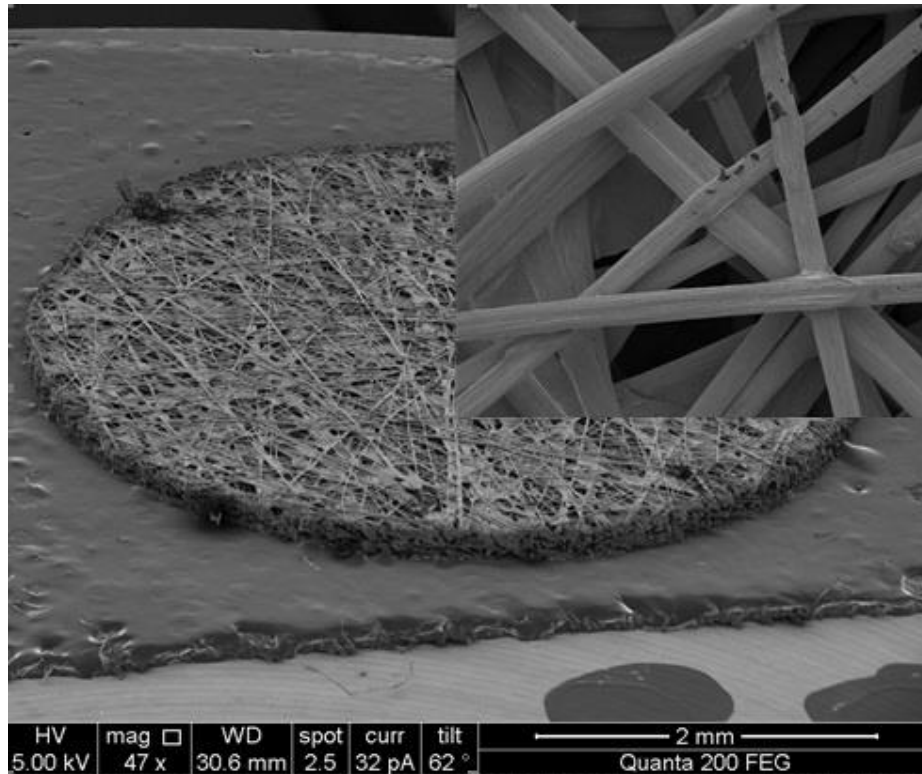


Figure 2.21 SEM images of the Pt coated carbon fiber surface after used. Catalytic reformers were used for 20 actuation cycles with each actuation period of half minute under a power of 2.4 mW [J2].

As demonstrated in subsection 2.2.1, Ni scaffold has a risk of consumption during the electrolytic reactions. While using carbon fiber scaffold, this concern is addressed here. After 20 cycles (the period of each actuation is 30 seconds, the applied power is 2.4 mW), its SEM images have been depicted as Figure 2.21, the surface of the catalytic reformer is unchanged (Figure 2.18 shows its SEM images before use). This demonstrates that both carbon fiber and platinum do not react with DI water, oxygen and hydrogen during the electrolytic reactions

with the chosen experimental parameters. Though Coughlin and Farooque claimed that anodic oxidation of coal at an electrode occurs at mild temperature [198], the carbon corrosion becomes readily observable in high temperature ($> 100^{\circ}\text{C}$) environment [198-200], however the implantable drug delivery device cannot be run at an elevated temperature for safety reasons. Further, the catalytic reformer is not directly in contact with the electrodes, avoiding electrochemical reactions on its surface. Considering the long-term application, more detailed verification for the carbon fiber scaffold's stability needs to be performed prior to implantation studies.

2.3 Cyclical actuation mode

The main feature of our drug delivery device is its cyclical pumping of the drug solution and refilling of the drug reservoir. This subchapter presents: 1) combining a SDR approach with a controllable electrolytic actuation model to extend treatment time; 2) lowering the applied power to allow for the possibility of wireless powering [34], which also further miniaturizes the size of the implant; 3) achieving on-demand drug release with a rate that can be accurately attained by intermittent delivery.

2.3.1 Cyclical operation performance

As stated already, the main function of the catalytic reformer is to increase the electrolysis-induced bubble recombination rate and reduce the period of the delivery cycle. The assembled electrolytic pump integrated with the carbon fiber mesh based catalytic reformer in the cyclical operation mode must be evaluated. This test used the same experimental apparatus as mentioned in subsection 2.2.1, characterizing the pumping performance of the

cyclical mode at different applied powers and actuation frequencies. Figure 2.22 shows the profiles of membrane displacement under applied powers of 2.4 mW, 4.5 mW and 6 mW, respectively.

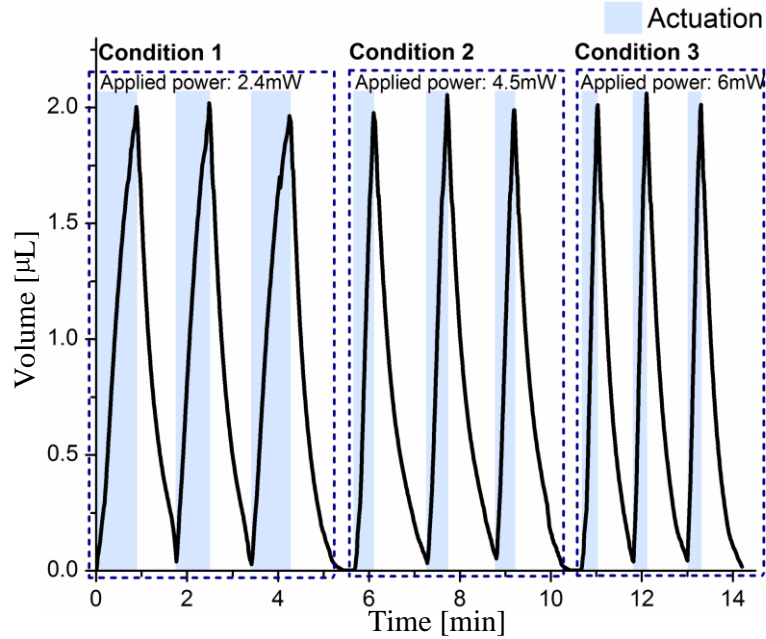


Figure 2.22 Cyclical displacement operated with different applied power indicating stable behaviors of electrolysis bubble generation and recombination [J2].

The increase in applied power leads to a shorter time for pumping due to faster bubble generation. When the power actuation is removed, the electrolysis bubbles immediately start to recombine, causing the red colour solution to flow back, which is equivalent to the refilled liquid. The integration of the Pt-coated carbon fiber mesh helps to quickly recombine 2 μL of gases in at about 1 minute, while almost the same volume of the gases needs far more than 4 minutes to be recombined without the application of the catalytic reformer as illustrated in Figure 2.20. Actuation conditions 1~3 in Figure 2.22 demonstrates the power-controlled and stable abilities of our cyclical pulsed delivery system that uses bubble generation and

recombination for pumping and refilling. Recombination time in each condition is slightly different, this is because the catalytic reforming elements were not mechanically fixed and they would randomly move upon the bubble generation, causing a non-constant contact area between the catalyst and the bubble.

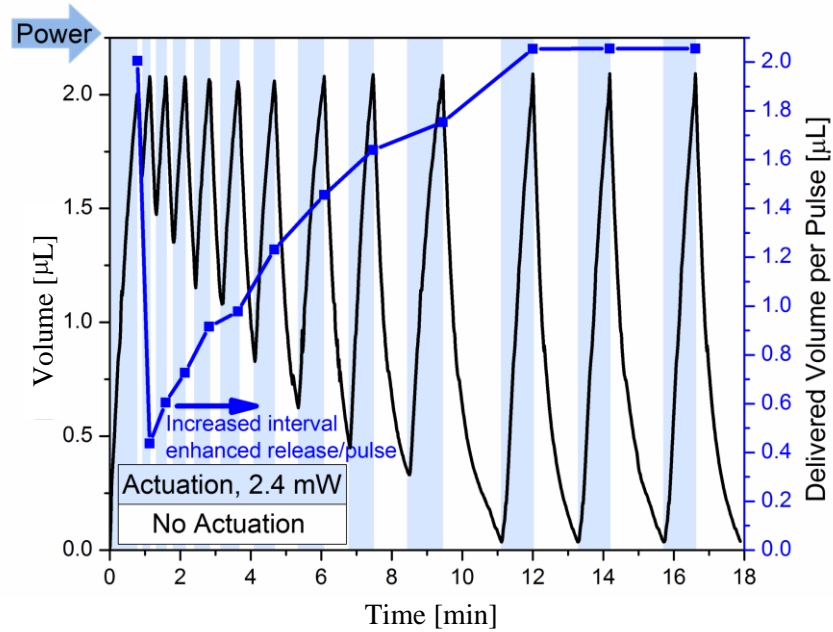


Figure 2.23 Membrane displacement operated with different actuation frequencies using a constant power of 2.4 mW [J2].

In addition to the applied power, the delivery frequency (the cycle numbers over the operation time) is also a critical factor that can determine the amount of drug delivered within a given treatment period. Our proposed device allows for power controlled flow rates and “on demand” delivery frequencies in order to meet the specific requirement of drug concentration level, addressing the patients’ needs. As an example of our devices functionality, Figure 2.23 depicts the relationship between delivery frequency and pumped volume for the cyclic mode when a power of 2.4 mW was used. A higher delivery frequency

means a shorter non-actuation interval between actuations, which may not provide sufficient time for full refilling of the reservoir, causing a less fluid to release during subsequent pulses. Decreasing the delivery frequency or increasing the non-actuation interval can enhance the delivered volume at each pumping. In order to obtain a compromise between the delivery frequency and the maximum amount of liquid released during each actuation, adding catalytic reformers is a must. Our Pt-coated carbon fiber meshes can quickly recombine the electrolysis bubble and provide full delivery within short periods, for example, the dose of 2 μL can be prepared in about 1 minute for the following actuations. Figure 2.23 also indicates the stable delivery profile over actuation durations and recombination intervals.

In summary, the addition of our catalytic reformers can nearly recombine all the electrolysis bubble and accelerate the recombination rate. This effect cannot only provide the maximum achievable displacement at each delivery, but it also allows for more delivery cycles within a specific treatment time.

2.3.2 Cumulative drug release

Overall daily dose is controlled by the number of fixed volume pumping cycles. In this experiment, we used solvent blue 38 (SIGMA-ALDRICH CO., MO, USA) as the solid drug substitute to evaluate our device's cyclical release performance. We used the setup depicted in Figure 2.24 to measure the release of the chemical substance. An external reservoir filled with 4% w/v bovine serum albumin (BSA) in phosphate buffered saline (PBS, pH 7.4) was used to emulate the human liquid environment (37°C) to which the drug was delivered. This solution was considered to be a suitable model of physiological fluid [30] and widely used

for *in-vitro* release tests [4, 30, 62]. A magnetic stirring bar was put into the external reservoir for accelerating the drug diffusion uniformly into the external liquid when the stirrer (Advanced Multi-position Stirrer, Henry Troemner LLC, USA) started to work. It is an idealized testing model, where cell absorption and naturally occurring flow rates in the body are not taken into account. The electrical wires were soldered to the electrodes of the pump so that the DC power source could power the device. We carefully placed the solvent blue 38 in powder-form on top of the PDMS membrane in advance. Then the PBS solution was injected in the drug reservoir through a laser-drilled inlet (see the inset of Figure 2.24) after the pump was assembled. We clamped the inlet afterwards, so that the laser-drilled outlet was the only channel used for pumping and refilling.

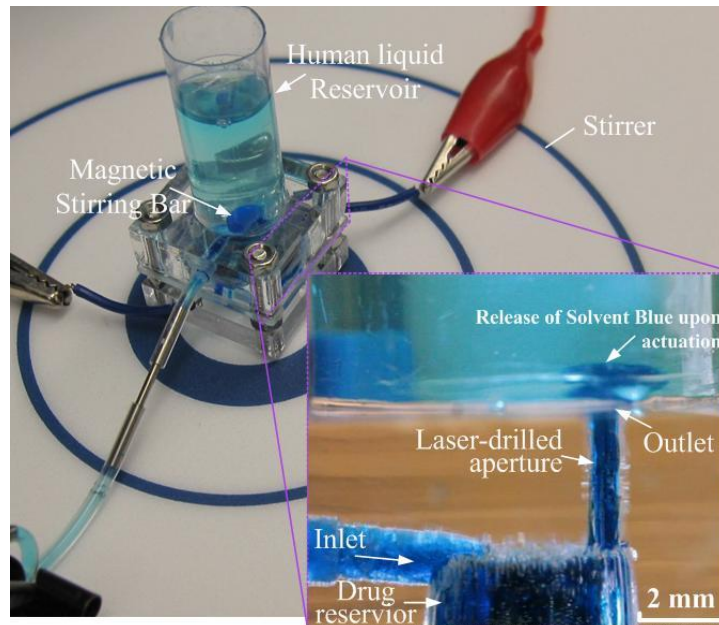


Figure 2.24 Experimental apparatus of drug delivery, side view of device depicts release of solvent blue into external solution upon electrolysis bubble actuation [J2].

As we already stated, the drug solution was pumped by electrolysis-bubble generations and

its volume corresponds to the displacement caused by the membrane deflection. The inset of Figure 2.24 demonstrates the released drug upon electrolytic actuation. Note that the pumping rate of the drug delivery device must be consistent with naturally occurring flow rates in the body. For example, flow rates of ocular drug delivery are preferred below 2 $\mu\text{L}/\text{min}$ as the ciliary body of the eye produces aqueous humor at $2.4 \pm 0.6 \mu\text{L}/\text{min}$ in adults [201]. Therefore, the released drug can diffuse away from the delivery site before it is sucked back into the reservoir during the refilling stage. The electrolytic reaction is reversible in the presence of Pt, so refilling stage happens when the applied power is removed. The fresh liquid refills the drug reservoir and mixes with the previous drug solution to dissolve fresh drug and achieves concentration equilibration for the next dose.

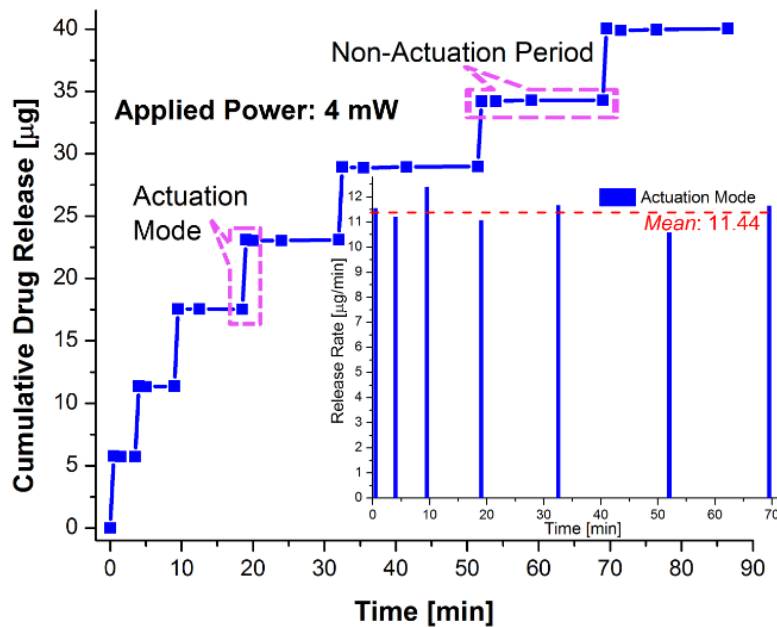


Figure 2.25 Intermittent release of solvent blue 38 from the pump to the external reservoir by applied power of 4 mW. After each pumping a period of delivery is followed with non-actuation mode. Released solvent blue 38 was cumulated by a series of actuations [J2].

In this experimental test, about 25% of the volume of the drug reservoir was used to store 3 mg of the solvent blue 38. We fixed the applied power at 4 mW, and the actuation time was 30 seconds for each delivery cycle. We used microliter spectrophotometry (Picodrop Ltd., UK) to measure the concentration change of the liquid in the external reservoir at the end of each actuation. Accordingly, the amount of each release with and without actuation was determined as shown in Figure 2.25. The cyclical power on-off operations provided a consistent drug release for multiple pulses over 90 minutes with a stable release rate of $11.44 \pm 0.56 \mu\text{g}/\text{min}$ (Mean \pm SD) during each actuation cycle of 30 seconds (see the inset of Figure 2.25). Two factors account for this stable dosing: firstly, the volume ratio between the newly refilled liquid and drug reservoir was $\sim 2 \mu\text{L}:60 \mu\text{L}$. This ratio reduces the impact on the overall concentration inside the drug reservoir; second, a certain amount of the fresh solid drug would be dissolved in the newly refilled liquid within the non-actuation period, thereby attaining new concentration close to the previous one. Dissolving time is related to drug's physical property, the correlated studies must be performed prior to the implantation. In this proof of concept drug delivery system, we demonstrated the feasibility of our device in terms of stable pumping profiles and drug release rate.

Note that diffusion-based drug release during the non-actuation period was rare due to a short non-actuation interval (from 2 minutes to 10 minutes in Figure 2.25) in this work. However, for the long period, its effects cannot be ignored. We did an independent test for 6 days, and we measured that 20 μg of solvent blue 38 diffused into the external liquid. Therefore the average diffusion rate over the course of these 6 days was 2.3 ng/min. In order to prevent such diffusion, a variety of valves can be developed in conjunction with our device in order

to avoid these effects over long-term usage.

Finally, this dissertation has not dealt with any biological issue as it is a proof of concept of the delivery system using a blood surrogate, which is a reasonably ideal testing environment. Further testing with *in-vitro* models and *in-vivo* testing in animal models will definitely provide greater information as to which body locations and environments are optimal for its operation, but such testing is outside of the scope of this work. The literatures on biological issues are given in the first chapter of this dissertation, which address the challenges of implementation.

2.4 Summary

This chapter investigated an on-demand electrolysis-driven pump which is intended for an accurate and controlled drug delivery system. Various release dosages and rates can be achieved by adjusting the applied power, such that it meets the concentration requirements at the disease site. An SDR approach was adopted, which is appropriate for long-term therapeutic treatments via the cyclically pulsed mechanism. This method uses cyclical power between on and off, dissolving a solid-form drug in human liquid during the bubble recombination phases, and forming reproducible drug solution for delivery at bubble generation phases.

The other key advantage over existing electrolytic pumps is that our device includes the catalytic reformer in the electrolyte chamber. In this work, sputtered Pt-Ni foam, electroplated Pt-Ni foam and Pt coated carbon fiber mesh were analyzed and evaluated. The sputtered Pt-metal foam increases the flow rate of the electrolytic pump, reducing power

consumption. However, this reduced power comes with a trade-off: the Ni scaffold is consumed during the electrolysis, which makes this device unsuitable for long-term applications. The electroplated Pt-metal foam is not consumed, and it provides a faster recombination rate. Consequently, the cycle time is reduced allowing a greater dosing range, but more or less Ni scaffold brings biocompatibility concerns. As a result, the Pt coated carbon fiber meshes were selected as the catalytic reformer. These reforming elements not only improve the recombination rate, but they lead to a shorter drug release cycle than the normal device. The Pt-coated carbon fiber meshes aid in fully recombining the generated gases into water, thus increasing the membrane displacement for the next delivery cycle. The drug concentration level is mainly a function of the delivery frequency and the volume of each delivery. Therefore, shorter pulsed period means that more cycles of drug release can be achieved within a given time. In other words, a wider dose range within a specific therapeutic period can be guaranteed, so that drug concentration can be controlled according to the current requirements of treatment.

A drug substitute with low aqueous solubility, solvent blue 38, was used to characterize our device. Our experimental results indicate that a consistent release rate of $11.44 \pm 0.56 \mu\text{g}/\text{min}$ was achieved in each actuation under an applied power of 4 mW. Because the concentration in the drug reservoir remains constant (close to the saturation state) before each delivery, the resulting release dose can be calculated using the drug's saturation and the pumped volume. The cumulative release of multiple pulses demonstrates the stability and feasibility of our proposed system.

Chapter 3 Remotely Operated Thermo-responsive Valve and the Actuator

This chapter presents a drug delivery device combining an electrolytic pump and a thermo-responsive valve, which are both remotely operated by an electromagnetic field (40.5 mT, 450 kHz). The drug delivery device exhibits a novel operation mechanism for long-term therapeutic treatments using an SDR approach, it also prevents undesired drug liquid diffusions. When the electromagnetic field is on, the electrolytic pump is powered, the electrolysis-induced bubble drives the drug liquid towards the Poly (N-Isopropylacrylamide) (PNIPAM) valve that consists of PNIPAM hydrogel and iron micro-particles. The heat generated by the iron micro-particles causes the PNIPAM to shrink, resulting in an open valve. When the electromagnetic field is turned off, the PNIPAM starts to swell. In the meantime, the bubbles are catalytically recombined into water, reducing the pressure inside the pumping chamber, which leads to the refilling of the fresh liquid from outside the device. A catalytic reformer is included, allowing more liquid refilling during the limited valve's closing time. The amount of body liquid that refills the drug reservoir can further dissolve the solid drug, forming a reproducible drug solution for the next dose. By repeatedly turning on and off the electromagnetic field, the drug dose can be cyclically released, and the exit port of the device is effectively controlled. Subchapter 3.1 presents the prototype of the PNIPAM valve and its fabrication; the methodology and the experimental results are analyzed in subchapter 3.2; summary is presented in subchapter 3.3.

3.1 PNIPAM valve

Over a long period, undesired drug diffusion from a drug solution to the human liquid

environment cannot be ignored at the outlet of the implant. This issue is especially important for therapeutic treatments using more potent drugs: uncontrolled drug diffusion may bring unpredictable harm to patients. Therefore, a controllable valve for the drug delivery device is needed. In previous works, a thermo-responsive PNIPAM valve was developed, which was controlled by inductive heating with an alternating current (AC)-driven electromagnetic field [27, 33]. The swelling and shrinking behaviors of the PNIPAM polymer monolith inside a micro-channel caused at different temperatures were demonstrated in [27]. This phenomenon occurs by expelling or absorbing water molecules, depending on whether the PNIPAM is above or below a designed lower critical solution temperature (LCST) [29, 204], respectively. In this manner, the hydrogel seals the channel or allows the liquid to flow through it.

Regarding the fabrication of the PNIPAM valve in this work, it is consisted of PNIPAM hydrogel and iron powder. Following the PNIPAM hydrogel's fabrication procedure in [205], we fabricated the PNIPAM hydrogel by mixing equal volumes of two different solutions: the first solution includes 20 wt% of N-Isopropylacrylamide (NIPAAm), 4wt % of N, N'-Methylenebisacrylamide (BIS) as a cross linker, and 2% v/v N, N, N', N'-tetramethylethylenediamine (TEMED) as a reaction accelerator; the second solution is 4.5 wt % of potassium persulfate (KPS) used as an initiator of the reaction. These two fluids were injected into the valve micro-channel through a Y-shape junction with an equal injection rate; the polymerization of the PNIPAM hydrogel occurred shortly after the two solutions diffused together. The polymerized PNIPAM (red color dyed) in a glass capillary (diameter of 0.5 mm) is depicted in Figure 3.1, when it is at room temperature ($\sim 22^{\circ}\text{C}$), it seals the micro-

channel (Figure 3.1a). A distinct feature of the PNIPAM is that it shrinks to about half its original diameter, when its temperature increases above the LCST (Figure 3.1b). This opens the valve, allowing the drug solution to be delivered outwards. Magnetic losses [206] in the iron powder cause the heat for this operation, which is induced by the same electromagnetic field that is able to drive the electrolytic pump for drug delivery.

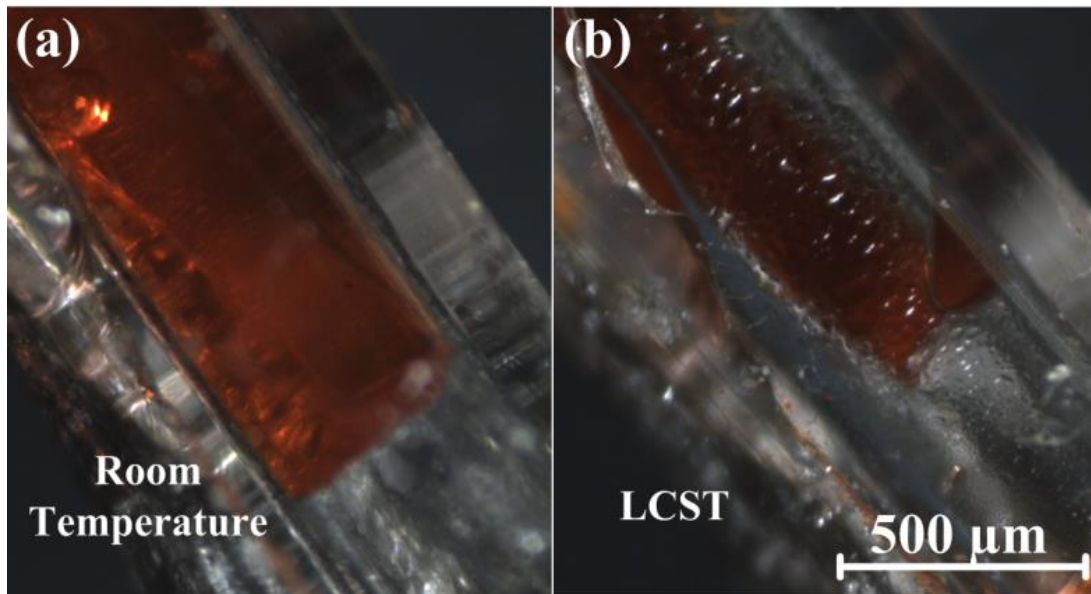


Figure 3.1 PNIPAM hydrogel: (a) at room temperature; (b) at LCST [C2].

Shrinkage efficiency is a critical factor for evaluating the practical use of the PNIPAM serving as a soft valve in the drug delivery system. In order to investigate the characteristic of PNIPAM microvalve and demonstrate the feasibility of the combination of the valve and the electrolytic pump, a red dye was used to track the displacement of fluid over the valve. In this experiment, the PNIPAM valve was made of a straight glass capillary (a diameter of 0.5 mm and a length of 22 mm) filled with PNIPAM polymer and surrounded by iron powder (size <math><10 \mu\text{m}</math>, purchased from Sigma-Aldrich Co. LLC.) which was glued to the capillary, as

shown in Figure 3.2. This design can maintain a stable state of the hydrogel at a cost of low thermal efficiency to the valve, and the heat dissipation may injure tissues or cells if it is directly exposed to the body environment. This valve was placed in an induction heating system (operated at 450 kHz, purchased from IEW GmbH) which was used to generate an electromagnetic field. The pump drove the tracking fluid towards the valve, while the valve was operated by different electro-magnetic field strengths, controlling the exit port of the electrolytic pump.

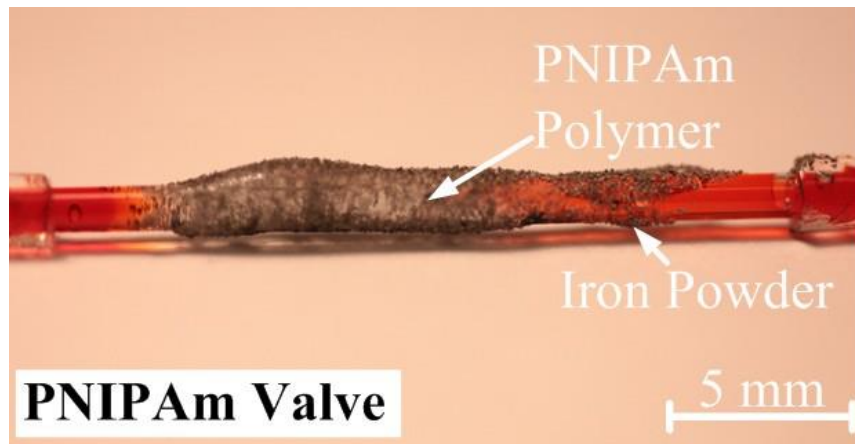


Figure 3.2 Straight PNIPAm polymer valve [C2].

In the electromagnetic field, iron particles produce heat due to the magnetic losses [206], which in turn cause the temperature increase of the valve. Figure 3.3 shows the throughput of the tracking liquid through the PNIPAM valve under different electromagnetic fields (40.5 mT and 58.5 mT). The results indicate that by increasing the electromagnetic field strength, the time required to achieve maximum throughput through the hydrogel valve decreases, resulting from a faster heating of the iron powder and thus a faster shrinking of the PNIPAM. The throughput here is the total volume of fluid (μL) having passed through the valve at any

time, after having turned on the electromagnetic field. In both cases, the PNIPAM valve reaches its terminal volume, beyond which it cannot shrink any further, and where it provides the largest throughput. However, the PNIPAM in the 58.5 mT test shrinks faster; thus, reaching this terminal volume sooner. Moreover, the particles' size may affect the heat generation rate in the field, but we found the size of the iron micro-particles we used did not negatively affect the valve's function at the field's operating frequency and strength; yet they are considerably more cost efficient than nano-sized beads like the ones used previously [27].

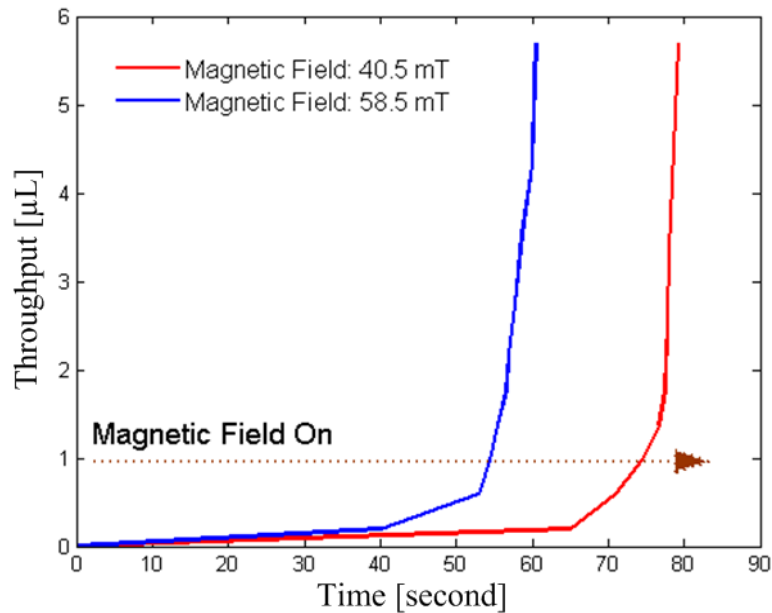


Figure 3.3 Throughput of the valve under different magnetic fields to demonstrate the corresponding opening time [C2].

3.2 Remote operation

A “remotely operated” drug delivery device is presented in this subsection, combining an electromagnetically powered pump with a thermo-responsive valve that results in an integrated system with components differing in function yet sharing the same remote power

source. The overall design of our proposed device is shown in Figure 3.4. The electrolyte chamber (Figure 3.4a) consists of a catalytic reformer and two interdigitated platinum/titanium (Pt/Ti) electrodes. Both the catalytic reformer and the electrodes are immersed into the electrolyte chamber, and an elastic PDMS membrane separates the pumping chamber from the drug reservoir (Figure 3.4b) in order to prevent oxidation of the drug solution and unwanted pH changes. The PNIPAM valve controls the exit port of the device. An inductive coil (Figure 3.4c) that is placed in the electromagnetic field connects to the contact pads of the electrodes for powering the pump.

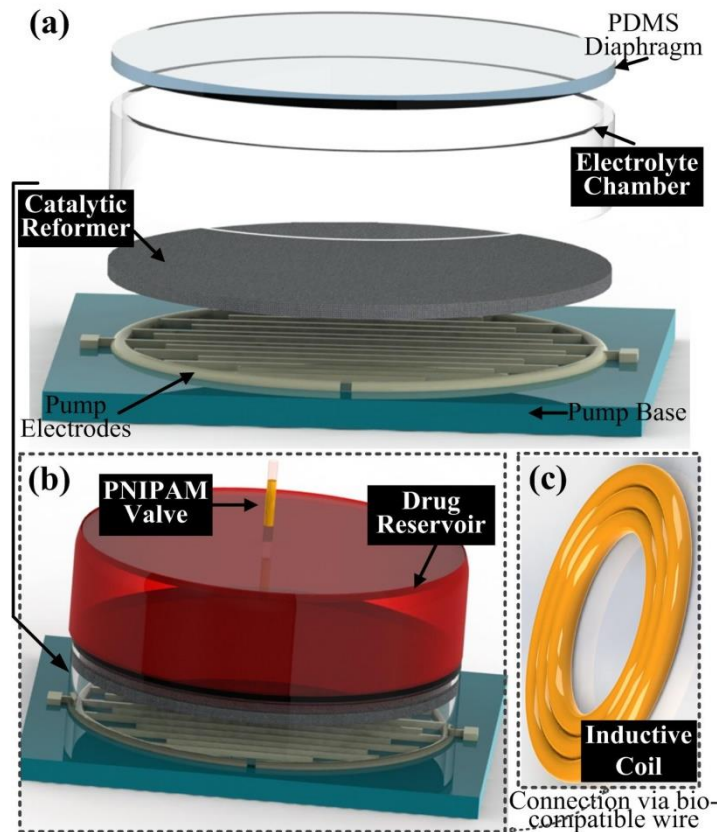


Figure 3.4 Exploded view of the device showing its major components [J3].

Accordingly, Figure 3.5 illustrates the device’s working principle in the electromagnetic

field. Pumping the drug fluid and refilling the drug reservoir is based on the deflection of the PDMS membrane. When the AC magnetic field is on, the induced voltage in the coil powers the electrode, driving the electrolytic reaction. The electrolysis induced-bubbles (H_2 and O_2 from the separation of DI water) deform the PDMS membrane, pushing the drug towards the valve. In this design, the valve is made of PNIPAM hydrogel mixed with iron micro-particles. The AC magnetic field causes heating of the iron micro-particles via magnetic losses [206], leading to the PNIPAM to shrink when the temperature reaches or passes its LCST. This change in the PNIPAM opens the valve and allows the drug solution to flow past it.

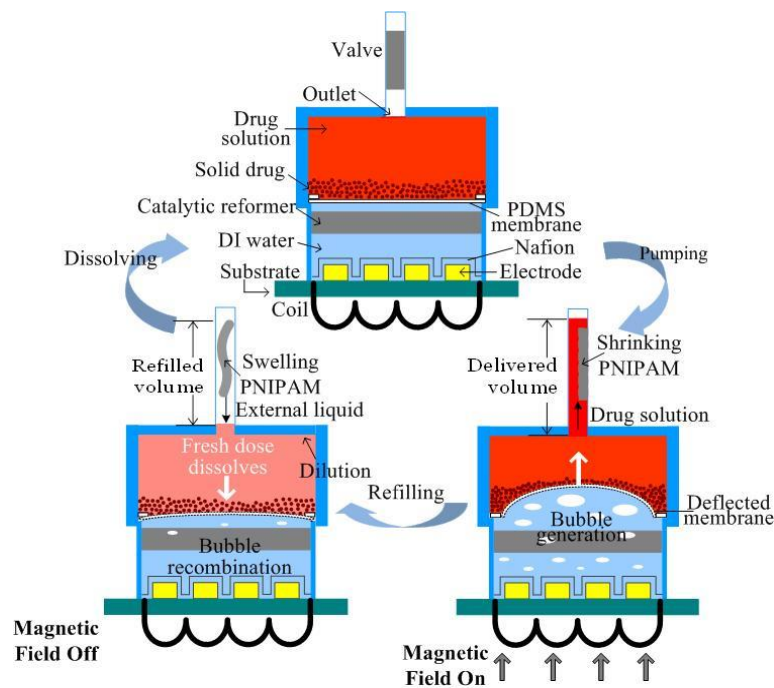


Figure 3.5 Schematic illustration of the SDR based device and its cyclic operation [J3].

When the magnetic field is off, the PNIPAM swells, sealing the outlet. In the meantime, because of the recombination of electrolysis bubbles into water, the PDMS membrane moves

downwards, causing fresh fluid from outside the device to refill the drug reservoir before the valve is fully sealed. This fresh fluid dissolves a certain amount of solid drug, based on the drug's solubility limit, forming the new drug solution for the next dose. The recombination process can be accelerated by the Pt-coated carbon fiber mesh, due to its catalytic properties. In this manner, more fluid can flow back into the drug reservoir within the valve's closing time. By repeatedly turning on and off the AC magnetic field, the drug solution can be delivered cyclically.

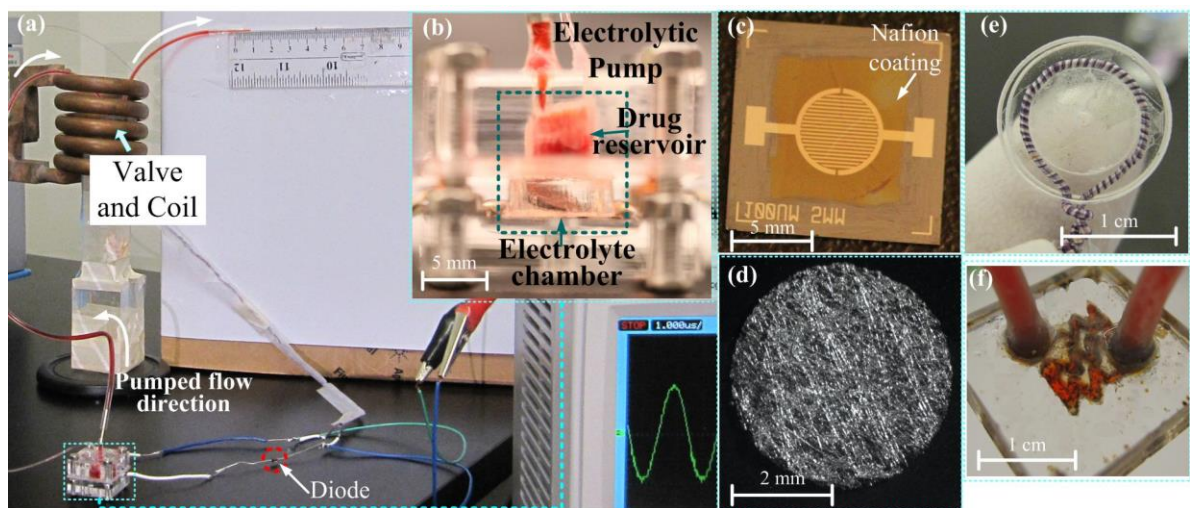


Figure 3.6 (a) photographs of the experimental apparatus and the prototypes of the major components: (b) assembled electrolytic pump; (c) image of Nafion coated Pt/Ti electrodes; (d) sputtered platinum coated carbon fiber mesh; (e) inductive coil; (f) the PNIPAM valve mixed with iron micro-particles [J3].

Figure 3.6(a) shows the experimental setup with the mounted prototype (Figure 3.6b); Figure 3.6c shows the Pt/Ti interdigitated electrodes with Nafion coating; In general, the Pt/Ti electrodes used in this work were fabricated following a standard lithography process: (i) photoresist deposition and ultraviolet light exposure to define the pattern, (ii) sputter deposition of Ti and then Pt, and (iii) lift-off processing to remove the sacrificial layers.

Nafion was spin-coated on the surface of the electrodes. The detailed fabrication process and dimensions were demonstrated in subsection 2.1.1. Figure 3.6d shows the catalytic reformer, which used the carbon fiber paper (Fuel Cell Store, Texas) with a diameter of 5 mm and thickness of 0.3 mm as a scaffold, its fabrication process and properties were investigated in subsection 2.2.2. The drug reservoir is made by drilling a cavity into a PMMA substrate; its internal radius is 2.5 mm, and its depth is 3 mm. The electrolytic chamber is also made of a PMMA loop with an internal radius of 2.6 mm and a height of 2.7 mm. To ensure the tests are repeatable, the electrolytic pump is mounted by tightening PMMA holders (2 cm by 2 cm by 2 cm). For prospective drug delivery applications, in order to reduce the size of the entire device, the holder can be substituted by a permanent bonding of the drug reservoir to the actuator chamber. A Litz wire coil (AWG 46) with a diameter of 10 mm and 1 turn (Figure 3.6e) was connected to the contact pads of the electrodes. The voltage induced by the AC magnetic field was then rectified by a diode for powering the pump. An oscilloscope (Agilent DS01012A) was used to measure the voltage induced in the coil. The electromagnetic field was generated by the induction heating system (IEW GmbH), and its field strength, B , can be calculated using Faraday's Law, given by:

$$V_{emf} = -N \frac{\Delta(BA)}{\Delta t} \quad (3.1)$$

where the voltage V_{emf} is measured by oscilloscope in the coil with area A and number of turns N , f is the field of frequency ($t = 1/f$).

The PNIPAM valve (Figure 3.6f) was constructed using a serpentine-shaped PMMA micro-channel, which was filled with a mixture of PNIPAM and the iron micro-particles (Sigma-

Aldrich Co. LLC.). The serpentine micro-channel (width: 0.4 mm; depth: 0.3 mm) was made on a PMMA substrate using a laser cutter (Universal PLS6.75). This serpentine structure helps keeping the PNIPAM in place, and it improves area efficiency benefitting system integration compared to a straight channel design in [27]. However, the mixture of iron particles with the PNIPAM may have a risk of affecting the performance of the hydrogel over time. After uniformly distributing 3 mg of the iron micro-particles into the micro-channel, the PMMA substrate was bonded to another PMMA substrate using a thermal-compression bonding system (INSTRON Dual Column Testing Systems). An optimized concentration of NIPAM monomer in the polymer matrix and the encapsulated magnetic particles improves the efficiency of the device [27], but this kind of optimization is out of scope of this work.

The magnetic field applied can be calculated using Faraday's Law, in which the area of the coil, number of turns and the field frequency determine the voltage induced in a coil. A red dye was used as a drug solution substitute, which could easily be tracked. A digital camera was placed in front of the test setup to record the displacement of the dye across a glass capillary at the outlet of the device. The setup as shown in Figure 3.6 was utilized for measuring the dye displacement over the valve, and this displacement was measured using a ruler. As analyzed in subsection 2.2.2, recombining the electrolysis bubbles during the non-actuation time, in the case of the pump without a catalytic reformer takes a considerably longer time, while the pump with a catalytic reformer, all the generated bubbles can be recombined within a short time. Owing to the fast recombination rate, the electrolytic pump with the catalytic reformer is much more suitable for this "remotely operated drug delivery system", allowing fresh fluid to rapidly refill the drug reservoir before the valve seals the

outlet. In order to further improve the recombination rate, we added three catalytic reformer elements to the system.

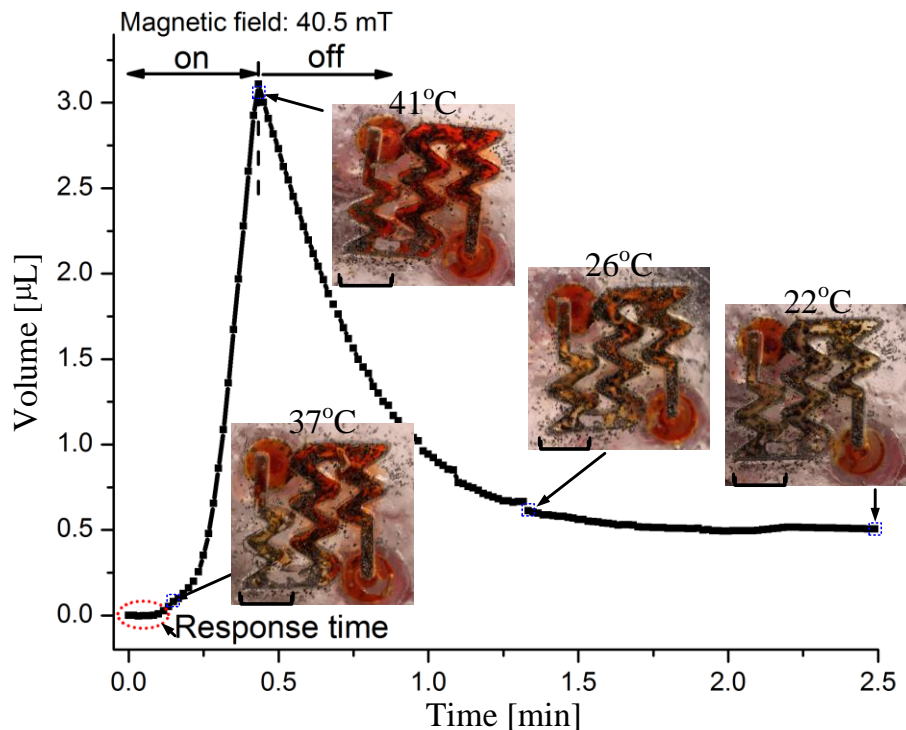


Figure 3.7 Pumping profile under an electromagnetic field of 40.5 mT when the thermo-responsive valve was used in combination with a pump with three catalytic reformer elements. The insets illustrate the states of the valve at different time points and the corresponding temperatures. Black particles are the iron micro-particles. Scale bars are 3 mm [J3].

The temperature of the PNIPAM valve was monitored by an infrared thermometer gun (Thermo Fisher Scientific Inc.). The dye displacement together with the valve's temperature under an electromagnetic field of 40.5 mT is shown in Figure 3.7. The PNIPAM valve required several seconds of response time before it opened. Following the response time, a small volume of liquid was displaced while the temperature of the valve was approximately 37°C. During this time, the valve was not completely open; however, a small percentage of

the valve had reacted to the temperature change. At this point, little liquid can pass through the valve during the PDMS membrane deflection. Afterwards, the slope of the displacement (or flow rate) increased, indicating that the valve was gradually opening. At a displacement of approximate 1 μL (~20 seconds), the slope of the displacement curve becomes linear (or constant flow rate), implying that the PNIPAM hydrogel has completely shrunken and the valve has reached its full open state. The electromagnetic field was applied until the volume displacement reached 3 μL (41°C at this point).

After turning off the electromagnetic field, recombination in the electrolytic chamber occurred, retracting the PDMS membrane and drawing liquid back towards the drug reservoir. By using three catalytic reformer elements, the recombination rate became much faster (analyzed in subsection 2.2.2). During the bubble recombination, the PNIPAM cooled down and swelled so that the valve closed. The valve was nearly closed after about 1 minute (when it reached 26°C). When the temperature of the valve dropped to 22°C, the valve was fully closed, leaving a displacement of 0.5 μL . This remaining displacement was caused because the valve's closing time was shorter than the pump's recombination time under the chosen parameters. This result demonstrates the valve's ability to properly seal the outlet.

In order to demonstrate the feasibility and stability of the SDR approach for multiple drug delivery doses, we operated the device in the “on/off” mode several times. In each cycle, the electromagnetic field was turned on until the dye displacement reached a value of 3.5 μL . After switched off the magnetic field, the dye flowed back and the PNIPAM hydrogel expanded. When the reverse dye flow stopped, we turned the electromagnetic field on again

for another cycle. Figure 3.8 shows the result of this cyclic operation. It can be observed that by pumping up to 3.5 μL in the first cycle, an un-refilled volume of around 0.5 μL remained. This un-refilled volume is due to the bubble recombination being slower than the valve's closing time, and becomes a stable offset after the first cycle.

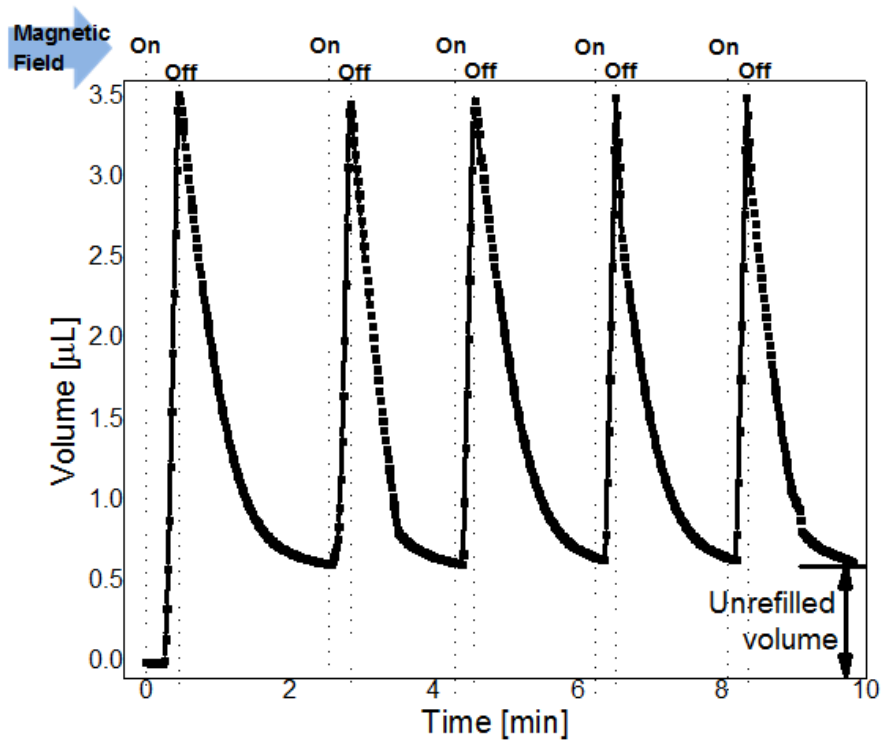


Figure 3.8 Cyclic liquid displacement of the dye when a device with a pump, three catalytic reformer elements and a PNIPAM valve is operated with an electromagnetic field of 40.5 mT that is periodically turned on and off [J3].

During the following cycles only 3 μL were pumped and the displacement reached its original value at the end of the refilling period. This observation suggests that a maximum volume of approximately 3 μL can be refilled within the valve's closing time and the same amount can be repeatedly pumped without any loss of volume over time. This condition must

be satisfied for long-term operation of a system that cyclically replenishes drug supply by dissolving an internal solid drug that continuously saturates the fluid. The recombination rate (or the slope of the negative displacement) at each pulse is slightly different, because the catalytic reforming elements were not mechanically fixed within the chamber and they would randomly move upon the bubble generation, thereby, changing the contact area between the catalyst and bubble. In future work, the catalytic reformer should be permanently bonded to the electrolyte chamber, in order to achieve a more stable bubble recombination rate.

3.3 Summary

In this chapter, we have demonstrated an electromagnetically operated drug delivery device with an electrolysis-actuated pump and a thermo-responsive valve. Both the pumping mechanism and the valve are operated remotely by the same electromagnetic field. The device is capable of releasing a single dose or cyclic doses of drug from a solid drug reservoir, and it features a valve-controlled exit port that prevents undesired diffusion. The operation mechanism of the device includes two stages corresponding to the electromagnetic field being “on” or “off”. In the “on” state the generated electrolysis-bubbles drive drug delivery through the open valve. In the “off” state the bubble recombination draws fresh liquid into the drug reservoir, which is needed for dissolving a new drug dose, and the PNIPAM valve closes, sealing the exit port. A cyclic operation of the device shows repeatable and stable behavior.

Moreover, the bubble generation rate and the recombination rate of the pump can be adjusted by selecting different sizes for the inductive coil and a different number of catalytic

reformers. For example, a reduced size of the coil can lead to a lower flow rate. The function of the valve is to avoid any drug diffusion, but it also requires that the recombination rate should be accelerated as much as possible to refill the drug reservoir before the valve fully closes. The required recombination rate was achieved by using three catalytic reformer elements inside of the electrolytic chamber. The device provides a suitable platform for the SDR approach, which is intended for a remotely operated drug delivery system for long-term therapeutic treatments.

Chapter 4 Optimization of a 3-Coil R-WPT System with Dose Control

Approach for Drug Delivery

Besides the electromagnetic induction, resonance-based wireless power transfer (R-WPT) system is newly emerged, that is capable of powering the implantable devices. Miniaturized size of the implantable coil and high power transfer efficiency (PTE) are the main tasks for such applications. This chapter presents a novel R-WPT system using three inductive coils which form a compact configuration and obtain a high PTE over a relatively large coil separation distance. At receiver side, secondary coil and load coil are wound together on a single layer, this design not only reduces the thickness, but also increases the coupling coefficient between the primary coil and load coil that, in turn increases the PTE. All coils achieve their maximum Q -factors after optimizing their geometry parameters. In our R-WPT prototype, the radius of implantable coils is 15-mm, with a resonance frequency of 6.76 MHz. The overall system is characterized in terms of inductance, capacitance, Q -factor and PTE. For the combination of R-WPT and drug delivery device, a critical issue is that the received voltage (or power) is unknown, resulting in an unpredictable release rate and dose. Therefore, we further add a voltage control circuit at receiver side, which maintains a constant voltage on the electrolytic actuator, providing well-defined flow rate. Subchapter 4.1 presents an optimized design of the coil model; subchapter 4.2 evaluates the R-WPT's performance and efficiency experimentally; subchapter 4.3 investigates the remotely operated drug delivery system combining the R-WPT and the constant voltage control circuit; summary is then given in subchapter 4.4.

4.1 Coils' design model

4.1.1 Wire property

As shown in Figure 4.1(a), the traditional coil design used in R-WPT system are made of a long electrically conductive wire that winds into a structure with N_a layers and N_t turns, increasing the thickness of the implantable devices. The wires used in resonance-based coils, commonly require a low effective series resistance (ESR) in order to reduce power dissipation. However, both the skin and proximity effects will increase the power dissipation due to the increasing ESR at higher frequencies [44]. In this case, the efficiency of the wireless inductive links will degrade. Therefore, multi-strand Litz wires are commonly used to mitigate the negative impacts of the skin and proximity effects [163, 207], the features of Litz wires are demonstrated in [208]. These wires' ESR, even at high frequencies, do not increase because they consist of multiple thin wire strands that are twisted together and are electrically insulated from each other (see Figure 4.1(b)). In this work, we employed AWG41 Litz wires for inductors.

When both the skin and proximity effects are taken into account, the AC resistance R_{ac} of a coil consisting of multiple Litz wires can be obtained as [163]:

$$R_{ac} = R_{dc} \left(1 + \frac{f^2}{f_h^2}\right) \quad (4.1)$$

where f is the operating frequency. f_h is the frequency at which power dissipation is twice the DC power dissipation, and R_{dc} is the DC resistance of the coil, which is derived from [44, 163], respectively;

$$f_h = \frac{2\sqrt{2}}{\pi r_s^2 \mu_0 \sigma \sqrt{N_a N_i N_s \eta_a \beta}} \quad (4.2)$$

$$R_{dc} = \sum_{i=1}^{N_a} \pi N_i D_i \frac{\rho R_s (1.015)^{N_B} (1.025)^{N_C}}{A N_s} \quad (4.3)$$

where r_s , N_s , β are the radius of each single strand wire (see Figure 4.1(b)), the number of strands per bunch, and the area efficiency of the bunch, respectively. The area efficiency, η_a of the coil is calculated in [163]. The vacuum permeability is represented by μ_0 and σ is the conductivity of the conductor. D_i is the average diameter of the coil at the i_{th} layer. A , ρ , R_s , N_B , and N_C are the wire cross-section area per strand, resistivity of the wire, maximum DC resistance of each strand, number of bunching operations, and number of cabling operations [44], respectively.

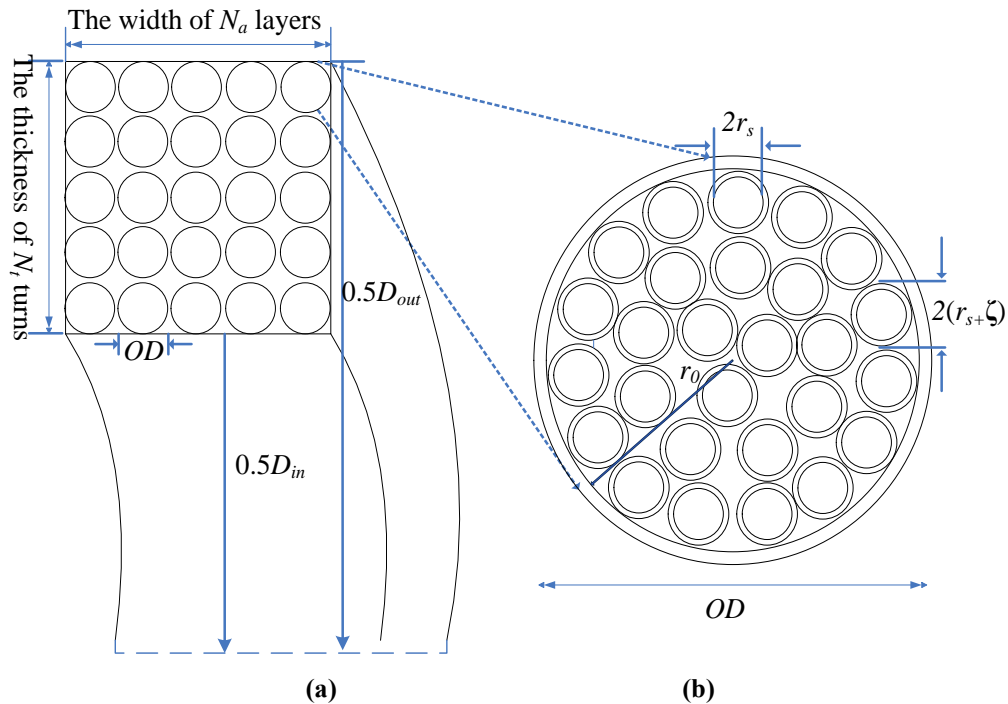


Figure 4.1 Coils' cross sections. Din: inner conductor loop, Dout: outer conductor loop, OD: outer diameter. (a) Typically wound Litz wire coil with multi-layer and multi-turn structure. (b) Cross sections of single turn with multi-strand wires [J4].

Parasitic capacitance is caused by the interplay between the wires due to their proximity to each other [209, 210]. If we further take the effect of the parasitic capacitance C_{par} and AC resistance into account, the total impedance of the coil becomes [163, 211]:

$$\begin{aligned} Z_e &= (j\omega L_{self} + R_{ac}) \parallel \frac{1}{j\omega C_{par}} \\ &= \frac{R_{ac} + j\omega L_{self}}{(1 - \omega^2 L_{self} C_{par}) + j\omega R_{ac} C_{par}} \end{aligned} \quad (4.4)$$

In this equation, the real part of Z_e represents the effective AC resistance, which is derived as:

$$ESR = \frac{R_{ac}}{(1 - 4\pi^2 f^2 L_{self} C_{par})^2} \quad (4.5)$$

The effective inductance L_{eff} , contributes to the imaginary part of Z_e , and is given by:

$$L_{eff} = \frac{L_{self}}{1 - 4\pi^2 f^2 L_{self} C_{par}} \quad (4.6)$$

where L_{self} is the total self-inductance of the coil.

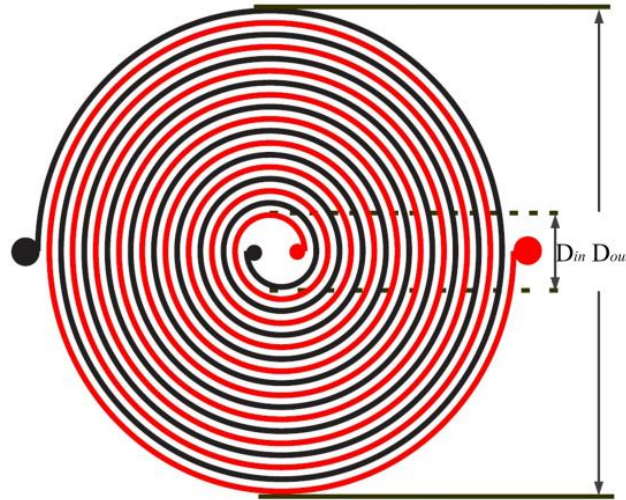


Figure 4.2 Proposed structures of secondary coil and load coil [J4].

4.1.2 Self-inductance and parasitic capacitance

The winding structure of our proposed coil pair for the secondary coil and load coil is shown in Figure 4.2. As both two coils at receiver side are wound on the same layer, the inductive coupling between the primary coil and load coil should be taken into account, but this coupling coefficient was always neglected in previously reported works [44, 164]. It is a single layer ($N_a=1$), so the total self-inductance of such a coil can be modeled as [44, 212]:

$$L_{self} = \sum_{i=1}^{N_t} L(a_i, R) + \sum_{i=1}^{N_t} \sum_{\substack{j=1 \\ j \neq i}}^{N_t} M(a_i, a_j, \rho = 0, d = d_{ij}) \quad (4.7)$$

The first term in the equation represents the summation of each turns' inductance, and the second term represents the summation of mutual inductance between turns. They can be calculated as follows, respectively.

$$\begin{cases} L(a, R) = a\mu_0[\ln(\frac{8a}{R}) - 2], & (R \ll a) \\ M(a, b, \rho = 0, d) = \mu_0\sqrt{ab}[(\frac{2}{k} - k)K(k) - \frac{2}{k}E(k)] \\ k = [\frac{4ab}{(a+b)^2 + d^2}]^{1/2} \end{cases} \quad (4.8)$$

where a_i is the radius of the i_{th} turn of a coil, R is the wire radius, N_t is the total turns on each coil layer, d_{ij} is the relative distance between i_{th} turn and j_{th} turn. When $\rho=0$, the turns on the layer are perfectly aligned. $K(k)$ and $E(k)$ are the complete elliptic integrals of the first and second kind, respectively.

As shown in Figure 4.2, turns are very close to each other, so the parasitic capacitance should be considered. In our proposed coil, parasitic capacitance for single layer coils is

approximately calculated as [213]:

$$C_{par} = \frac{1}{N_t^2} [C(N_t - 1)] \quad (4.9)$$

where C is parasitic capacitance between neighboring turns and it is given by [163]:

$$C = \varepsilon_0 \varepsilon_r \int_0^{\pi/4} \frac{\pi D r_0}{\zeta + \varepsilon_r r_0 (1 - \cos \theta) + 0.5 \varepsilon_r d} d\theta \quad (4.10)$$

where D , r_0 , ζ , d , ε_r and ε_0 are the average coil diameter, inner radius of a bunch, thickness of the insulation coat (see Figure 4.1b), relative distance between neighboring turns, relative permittivity of strand insulation and dielectric constant of the free space, respectively.

4.1.3 Q -factor calculation

For coils used in R-WPT systems, the Q -factor and self-resonance frequency are critical. A high Q -factor reduces heat dissipation, which is a very important requirement for implantable medical devices (IMDs). Moreover, a high Q -factor can contribute to a high PTE, its influence on PTE can refer to [44]. The general Q calculation is defined as:

$$Q = \frac{2\pi fL}{R} \quad (4.11)$$

As analyzed above, the effective Q -factor of our proposed coil without load can be derived by:

$$Q_{eff} = \frac{2\pi fL_{eff}}{ESR} = \frac{2\pi fL_{self}}{R_{dc}} \left(1 - \frac{f^2}{f_{self}^2}\right) \left(1 + \frac{f^2}{f_h^2}\right)^{-1} \quad (4.12)$$

where the self-resonance frequency f_{self} can be derived by the self-inductance L_{self} and the parasitic capacitance C_{par} of the coil:

$$f_{self} = (2\pi\sqrt{L_{self}C_{par}})^{-1} \quad (4.13)$$

The self-resonance frequency should be taken into account at the beginning of the coil design, especially for those coils that operate at a higher frequency. Because the self-resonance frequency constrains the maximum operating frequency of the coil, if the operating frequency exceeds its self-resonance frequency, the ESR will increase drastically [214], and the entire coil will not function. Therefore, the self-resonance frequency should be kept at a relatively high level in order to obtain a high Q -factor according to (4.12).

Table 4.1 AWG LITZ wire property.

Radius of wire per strand,	0.06 μm
Number of strands, N_s	60
Area efficiency, β	83%
Conductivity, σ	58 S/mm ²
Inner loop diameter, D_{in}	6 mm
Thickness, ζ	3 μm
Inner radius, r_o	0.51 mm
Relative permittivity, ϵ_r	3

The AWG Litz wire with 60 strands was adopted in our R-WPT experiments; the other physical parameters of the AWG Litz wire are listed in Table. 4.1. Based on the proposed design of implantable coils, the diameter of the first loop must be small in order to make a relatively small size of implantable coils, so an inner loop diameter of 6 mm was used. Moreover, the selection of the operating frequency is critical for implantable WPT systems, according to the ISM band standard, frequency range (6.765 MHz \sim 6.795 MHz) was adopted in our system to work within an unlicensed band for wireless devices. Based on the

property of AWG Litz wires, and substituting (4.7)-(4.10) into (4.13), Figure 4.3 shows the calculated tendency of the self-resonance frequency, f_{self} , versus the number of turns, we can observe that f_{self} decreases sharply when the number of turns is less than 10, although f_{self} decreases with the increasing turns, the minimum frequency is 14 MHz which is still large enough for obtaining a low ESR.

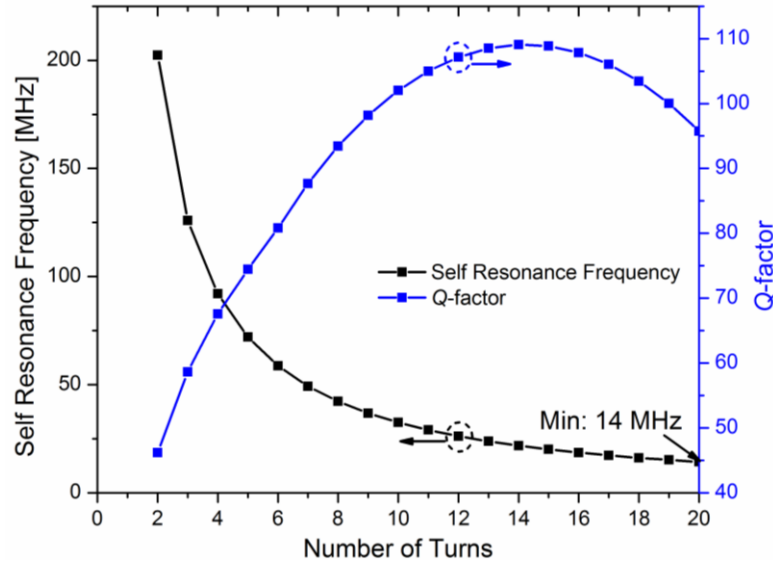


Figure 4.3 Tendency of self-resonance frequency and Q -factor versus the number of the turns, the operating frequency $f=6.7$ MHz [J4].

Besides f_{self} , the other parameter for calculating the Q -factor in (4.12) is f_h , which should be as high as possible. Because it not only optimizes the Q -factor, but it also prevents the coil from severe power dissipation due to the proximity effect [163]. In our proposed coil model, f_h can achieve a distinctly higher value as compared to its counterpart in the traditional coil structure by calculating (4.2) due to a single layer ($N_a=1$). Figure 4.3 shows that the Q -factor increases monotonically with the increasing turns when the operating frequency is 6.7 MHz and achieves its peak when the number of the turns is around 12. The Q -factor starts to drop

when the number of turns is over 14 because AC resistance dominates according to (4.12). This figure can optimize our proposed coil design to obtain a highest Q -factor. In previously reported works, the maximum diameter of the implantable coil was 30 mm [155], so 12 turns that can obtain an approximately peak Q -factor was selected to form a coil with a diameter of 30 mm as shown in following sections.

4.2 Power transfer efficiency evaluation

4.2.1 Power transfer models

For conventional WPT systems, the 2-coil model was widely used for inductive coupling where the PTE strongly depends upon the Q -factor of the primary coil (Q_p), secondary coil (Q_s) and mutual coupling (k). This relationship is defined as [157, 158]:

$$\eta^{2-coil} = \frac{k^2 Q_p Q_s}{1 + k^2 Q_p Q_s} \quad (4.14)$$

More recently, a 4-coil power transfer system, based on coupled-mode theory (CMT) [215], was proposed for a high PTE at a relatively long coupling distance. 4-coils refers to the driver, primary, secondary and load coil (also denoted as coils 1 to 4 for simplicity in this dissertation), respectively. For a relatively large transfer distance in a 4-coil system, because the coupling coefficient k_{mn} is proportional to d_{mn}^{-3} , where d_{mn} is the separation between coils m and n , the terms k_{13} , k_{14} , and k_{24} are usually neglected, Therefore, the corresponding PTE is computed as [44, 164]:

$$\eta^{4-coil} = \frac{(k_{12}^2 Q_1 Q_2)(k_{23}^2 Q_2 Q_3)(k_{34}^2 Q_3 Q_{4L})}{[(1 + k_{12}^2 Q_1 Q_2)(1 + k_{34}^2 Q_3 Q_{4L}) + k_{23}^2 Q_2 Q_3](1 + k_{23}^2 Q_2 Q_3 + k_{34}^2 Q_3 Q_{4L})} \quad (4.15)$$

where $Q_m = 2\pi f_0 L_m / R_m$ is the unloaded quality factor of coil m . R_m and L_m are the effective resistance and inductance of the coil m , respectively. Because coil 4 connects to the load R_L in series, the loaded Q -factor Q_{4L} can be derived as:

$$Q_{4L} = \frac{2\pi f_0 L_4}{R_4 + R_L} = \frac{Q_4}{1 + Q_4 Q_L} \quad (4.16)$$

where Q_L refers to the load Q -factor, and it is calculated as $R_L / 2\pi f_0 L_4$ [215]. The highest PTE can be achieved when all of the coils operate at the same resonance frequency f_0 :

$$f_0 = \frac{1}{2\pi\sqrt{L_m C_m}} \quad (4.17)$$

where C_m is the effective capacitance of the coil m .

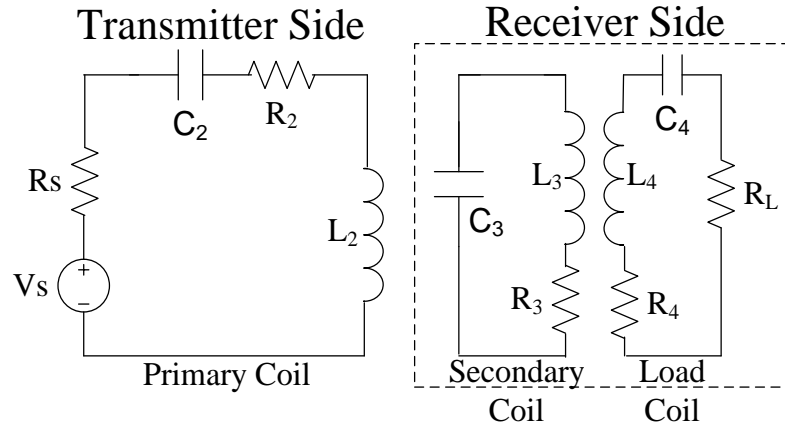


Figure 4.4 Circuit model of the 3-coil R-WPT system [J4].

Our proposed three coils R-WPT system uses coils 2-4. The coil pair (coils 3 and 4) is on the receiver side, so that a high coupling coefficient k_{34} can be obtained. This design can effectively compensate the transfer efficiency degradation caused by loaded Q -factor Q_{4L} reduction. Based on (4.16), the reduction of Q_{4L} is caused by increasing the load resistance.

Therefore, the overall PTE is affected by the increasing of the load at the receiver side. The corresponding circuit-based schematic diagram is shown in Figure 4.4. In Figure 4.4, where V_s is the power source applied to the primary coil, and R_s is source output impedance. Because inductance L_2 to L_4 are different from each other due to the different structure of coils, in order to form the same f_0 over the coils, different capacitors C_2 to C_4 should be selected according to (4.17). The PTE of such a 3-coil scheme is [164]:

$$\eta^{3-coil} = \frac{(k_{23}^2 Q_2 Q_3)(k_{34}^2 Q_3 Q_{4L}) + k_{24}^2 Q_2 Q_{4L}}{(1 + k_{34}^2 Q_3 Q_{4L})(1 + k_{23}^2 Q_2 Q_3 + k_{34}^2 Q_3 Q_{4L} + k_{24}^2 Q_2 Q_{4L})} \quad (4.18)$$

Because the distance d_{23} between coil 2 and coil 3 is same as the distance d_{24} , all of coupling coefficients k_{23} , k_{24} and k_{34} should be considered. Actually, there is another 3-coil system, using two coils on the transmitter side and one coil at the receiver, or 2T-1R model for simplicity. By calculating (4.18), we can observe that a larger k_{34} can effectively improve the PTE than k_{23} , demonstrating that two coils on the receiver side can achieve a higher PTE against transfer distance theoretically.

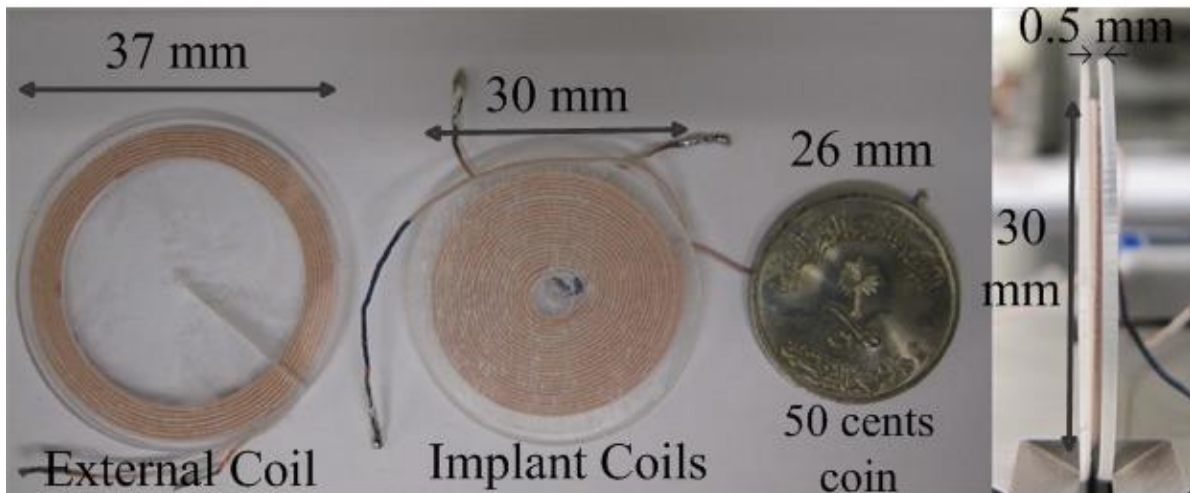


Figure 4.5 Implant coils' dimensions using AWG Litz wire [J4].

4.2.2 Design optimization

Based on the structure of the coils as shown in Figure 4.2, we wound 12 turns for both the secondary coil and load coil. The dimensions of the implantable coils are illustrated in Figure 4.5, where the two coils are wound in parallel on one layer. On the transmitter side, we also wound the coil on a single layer to reduce the thickness of the external devices. Because the primary coil is not strictly constrained by size issue, the outer diameter of the primary coil could be larger than that of implantable coils. The geometric specifications of the coils are summarized in Table. 4.2. The primary coil and implantable coils are made co-centric, and an Agilent 4294A precision impedance analyzer was used to measure the inductance and Q -factor of the coils with the coils' dimensions listed in Table. 4.2. Figure 4.6 describes the measured Q -factor curves versus the operating frequency for the coils 2-4. The frequency range where the coils have the maximum Q -factor is represented by f_{peak} .

Table 4.2 Coils' physical specification by measurements [J4].

Type	Coil Num.	Outer Dia. (mm)	Inner Dia. (mm)	Turn/Layers N_t	Layers N_a	DC Resistance (Ω)	Inductance (uH)	Capacitance (pF)	Q -factor (6.7MHz)
Primary Coil	2	37	30	7	1	3.3	3.16	160	173
Secondary Coil	3	30	6	12	1	3.4	1.97	260	118
Load Coil	4	30	6	12	1	3.6	1.87	260	112

From Figure 4.6, we can observe that all coils 2 through 4 can achieve a nearly peak Q -factor when the operating frequency ranges from 6 to 7 MHz. Based on our measured inductances of coils as given in Figure 4.6, in order to tune all the coils at the same resonance frequency within f_{peaks} , and follow ISM band requirement, we employed three capacitors of 160 pF, 260

pF and 260 pF (listed in Table 4.2) for coils 2 through 4, respectively. From (4.17), we obtained a theoretical resonance frequency of 7 MHz.

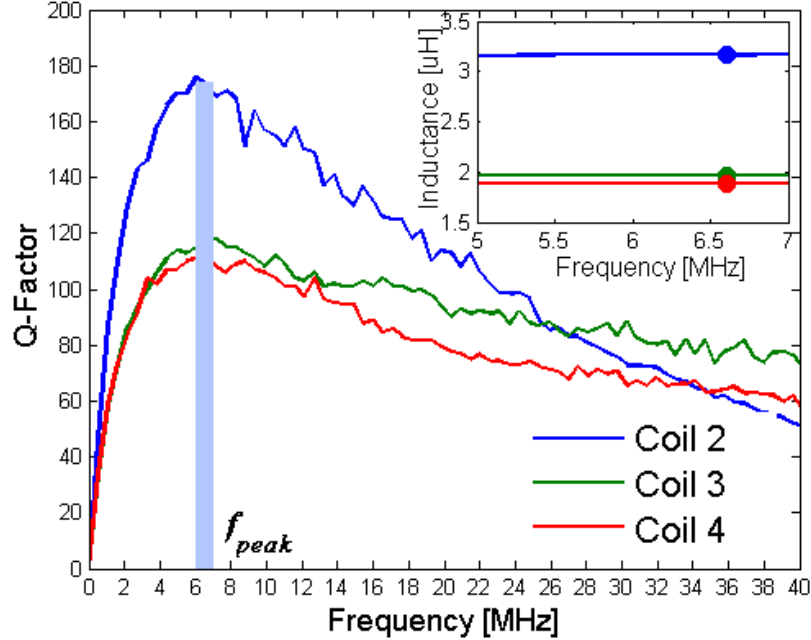


Figure 4.6 Q -factors' curve versus operating frequency [J4].

4.2.3 Experimental setup and measurements for PTE

The PTE is measured and analyzed in this subsection. The main difference between a 2-coil system and our proposed 3-coil system is that an unloaded coil (secondary coil) is added next to the load coil for obtaining an additional Q_3 . A high Q_3 is very useful to improve the PTE. According to the specifications of the coils listed in Tables 4.2, the measured Q -factors and sizes of coils 2 and 4 are used for PTE simulation. Regarding the coupling coefficient between coil 2 and 3, k_{23} is calculated as [44]:

$$k_{23} = 148.2 \left(\frac{1}{d_{23}^2 + r_m^2} \right)^{1.2} - 0.0002857 \quad (4.19)$$

where r_m is the geometric mean of the radii of the primary coil, r_p and the secondary coil r_s . This coupling coefficient indicates an idealized testing model in the free space, for different transmission medium, the coupling will change accordingly.

Figure 4.7 shows the impact of the Q_3 on PTE versus the coupling distance for our proposed R-WPT model. From Figure 4.7, we can observe that PTE decays with an increasing coupling distance d_{23} , however, a high Q_3 can compensate the negative effects of a low coupling coefficient. By increasing Q_3 , the PTE can be improved even at a large transfer range as shown in Figure 4.7.

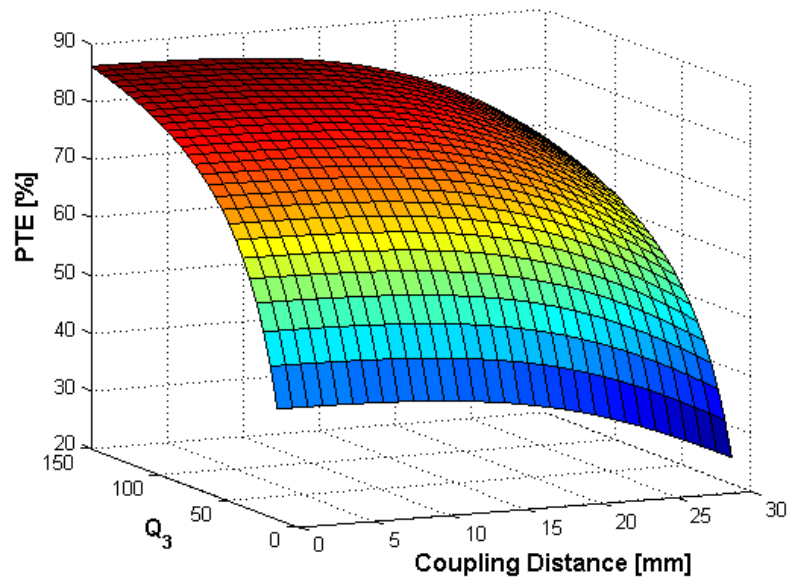


Figure 4.7 PTE versus the Q_3 and d_{23} for the 3-coil system; $Q_2=173$, $Q_4=112$, $R_L=100 \Omega$, $r_p=15\text{mm}$, $r_s=17.5\text{mm}$ [J4].

To demonstrate the validity of the R-WPT techniques, a prototype of 3-coil WPT system as shown in Figure 4.8a was designed and implemented. Moreover, Figure 4.8a also shows the experimental setup of the PTE measurement system. A NI PXI 5402 was used to supply the

AC power on the primary coil. In Figure 4.8b, an Agilent DS01012A oscilloscope displays both voltage waveforms of the primary coil and load coil. A load R_L of $100\ \Omega$ was connected in series with L_4 in the coil 4 in order to compare a previously reported 3-coil work where $100\ \Omega$ of load was used [164]. The current of the coil 4 was calculated by measuring the voltage on R_L . Thus, the received power was obtained by measuring the current flow and voltage waveforms directly.

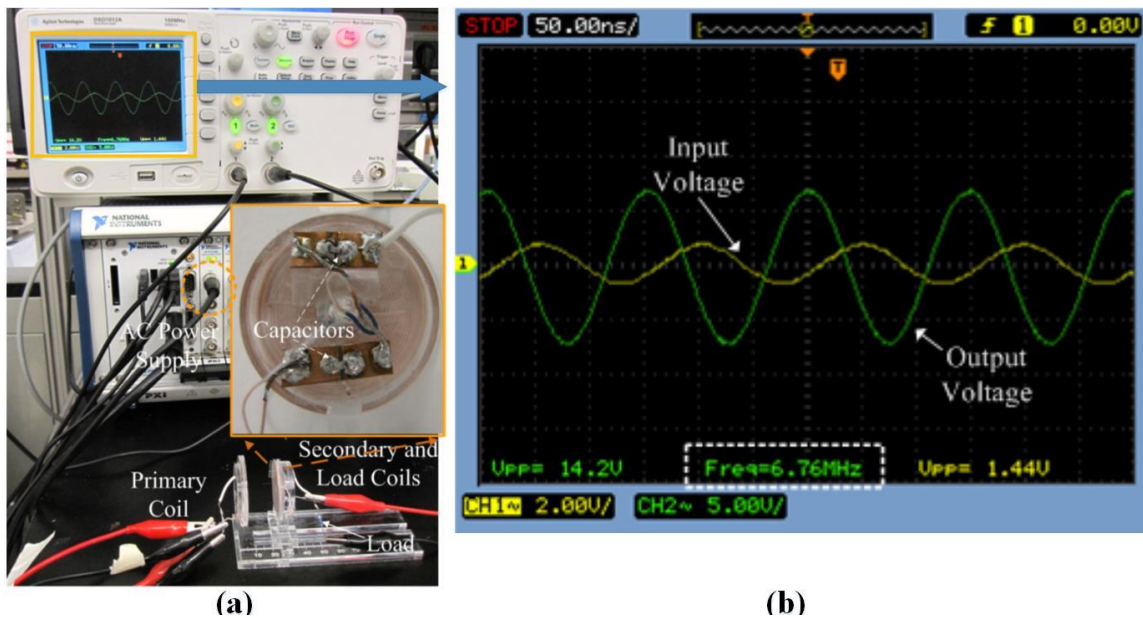


Figure 4.8 (a) The experimental setup for the three-coil WPT system. (b) The measurement results of the primary coil input voltage and load coil output voltage, $d_{23}=20$ mm [J4].

Figure 4.8b illustrates the voltage waveforms of the transmitter and receiver at a transfer distance where $d_{23}=20$ mm. The Waveform generator was tuned at $f_0=6.765$ MHz, equal to the frequency where the voltage on coil 4 achieves the peak, which means this frequency is the actual resonance frequency for the entire WPT system. The voltage at the load coil was much higher than that of the primary coil from Figure 4.8b, because the total turns at receiver

side is larger than that at transmitter side, contributing to voltage amplifier function. This is required for applications of integrating the voltage control mode. The current of load coil was much less than that of primary coil in the measurements. The corresponding PTE derived by measuring the current and voltage over the transmitted power was 82.4% at this distance. We changed the transfer distance d_{23} from 15 mm to 50 mm, which varied the received power, thus, the PTE changed accordingly. The plots of the measured PTE were presented in Figure 4.9.

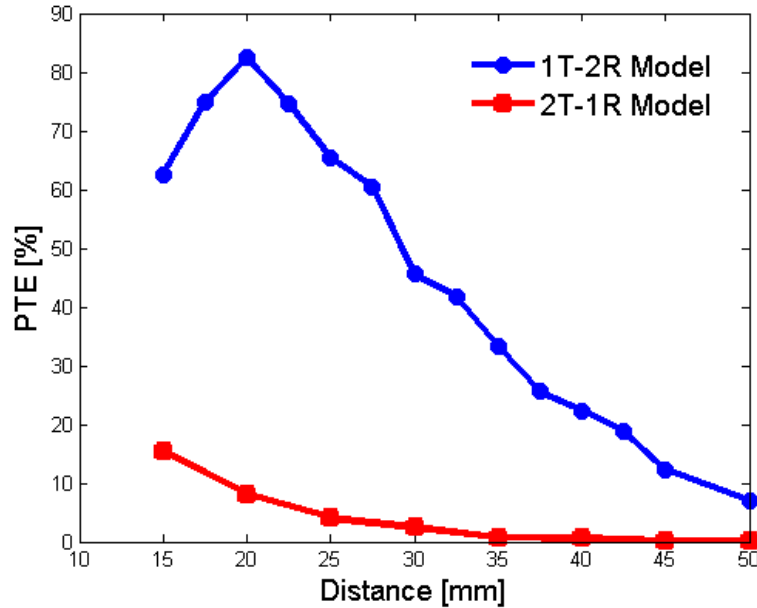


Figure 4.9 PTE measurement comparisons versus the coupling distance [J4].

The highest PTE of 82.4% was achieved at the distance of 20 mm. For given WPT model where the Q -factor of primary coil is fixed, an optimum transfer distance that PTE can achieve a maximum does exist [44], so in our design, 20 mm is the optimum distance. Moreover, the PTE can keep a high value (10%) over the distance up to 45 mm. In order to convince that two coils on the receiver side can effectively improve the PTE, 2T-1R under a

same experimental condition was tested as a comparison. The corresponding experimental results were shown in Figure 4.9 as well, which shows a much lower PTE than our proposed 1T-2R model, verifying that a larger k_{34} is indeed critical to improve the PTE.

Table 4.3 Comparison with previously reported works [J4].

Ref.	No. of Coil	Dimension (r_p, r_s) (mm)	Fre. (MHz)	PTE	Distance (d_{23}) (mm)
[155] Baker <i>et al.</i> , 2007	2-coil	(15, 15)	4.5	54%	10
[165] Jow <i>et al.</i> , 2007	2-coil	(35, 10)	5	30%	20
[162] Xue <i>et al.</i> , 2012	2-coil	(60×25, 25×10)	13.56	20.5%	20
[164] Kiani <i>et al.</i> , 2011	3-coil	(43, 9.1)	13.56	39%	20
[44] Ramrakhyani <i>et al.</i> , 2011	4-coil	(32, 11)	0.7	82%	20
This work	3-coil	(17.5, 15)	6.76	82.4%	20

For a potential biomedical application, the implantable coil can be placed underneath the skin, so the distance between the external device and implantable coil is around 20 mm. Table. 4.3 compares the PTE at a transfer distance of 20 mm between our proposed design with previous studies, such as 2-coil RF power link [155] and its spiral coils structure [165], 3-coil inductive link [164] and 4-coil resonance coupling [44], respectively. All of these works are intended to be applied for potential biomedical implants, for example, Xue *et al.* demonstrates the power transfer performance through different transmission medium (air and tissue) [162]. From Table 3, our proposed 3-coil system and previously reported 4-coil systems show a higher PTE than the 2-coil system because the 2-coil system is very sensitive to the transfer distance d_{23} . In contrast, 3-coil and 4-coil systems can keep a relatively high PTE over a long coupling distance. Additionally, our proposed 3-coil system has a close PTE

as 4-coil system does in the experimental studies, but shows a simpler structure and more suitable design for implants.

In summary, coil size, Q -factor, self-resonance frequency and PTE are key parameters for evaluating the WPT applications, which affect the heat dissipation, operation frequency, power transmission range and maximum load. Coils used in implantable electronics, such as 2-coil and 4-coil WPT systems were compared to our proposed 3-coil scheme using a pair of coils with a single layer. Our 3-coil scheme shows a distinctly higher and comparable PTE versus the coupling distance compared to the equivalent 2-coil and 4-coil system, respectively. For those implants potentially applied underneath the skin, our proposed coil design cannot only reduce the thickness of the implantable devices, but also contribute to both a high Q -factor and self-resonance frequency for the coils, achieving a highest PTE at a distance of 20 mm, which was proven experimentally. Moreover, the selection of the operation frequency must be carefully considered before industrial design, the frequency of 6.76 MHz we used for this work completely follows ISM standards.

4.3 Remotely operated drug delivery with dose control

4.3.1 Wireless system architecture

As described above, the R-WPT system consists of two parts: the transmitter and the receiver. At the transmitter side, an alternating current (AC) source is applied to the primary coil, creating an AC magnetic field, which induces a voltage across the secondary and load coils at the receiver side. Adopting the aforementioned R-WPT system, we further add a constant voltage control circuit at the receiver side. The circuit diagram of this new R-WPT

system is illustrated in Figure 4.10(a). The functions of the control circuit include AC/DC conversion and constant voltage supply for driving the actuator. It consists of a 4-diode bridge rectifier and a 5V Zener diode. The corresponding prototype is illustrated in Figure 4.10 (b).

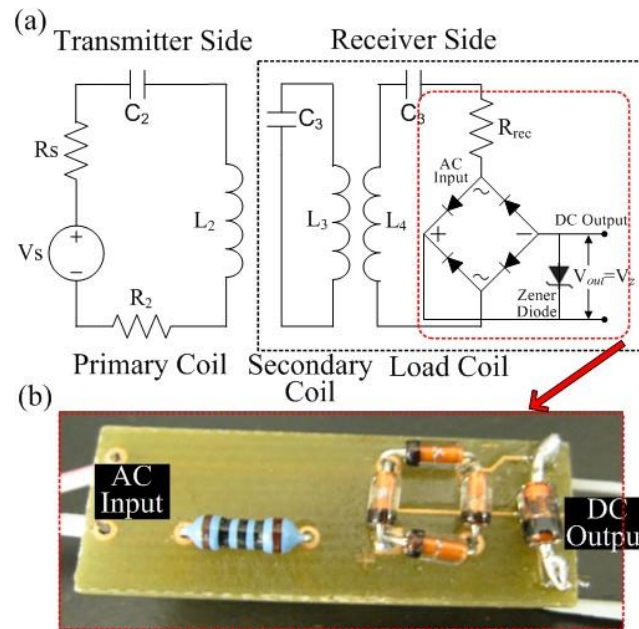


Figure 4.10 Resonance-based wireless power transfer system with the constant voltage control circuit: (a) the corresponding circuit model; (b) the prototype of the control unit. V_s is the voltage output of the AC power source, R_s is the output impedance, R_{rec} is the resistance of the receiver, C_2 - C_4 denote capacitors, and L_2 - L_4 represent coils [J5].

To highlight the effect of the Zener diode in our system we performed an experiment with the circuit unloaded, and directly measured the output voltage of the rectifier at a variety of coil positions and orientations with and without the Zener diode. The Zener diode in its “reverse bias” regulates the voltage output of the rectifier, providing a stable 5V output as long as the voltage induced at the load coil is higher than 5V, as demonstrated in Figure 4.11. As our 3-coil R-WPT system amplifies the output voltage due to the turn ratios, triangle dots in Figure

4.11 indicate the actual voltage received without the voltage regulator, though a peak voltage is received at a transfer distance of 20 mm due to the design of this 3-coil R-WPT, on the whole, the voltage is decreasing with the increasing distance (Figure 4.11(a)).

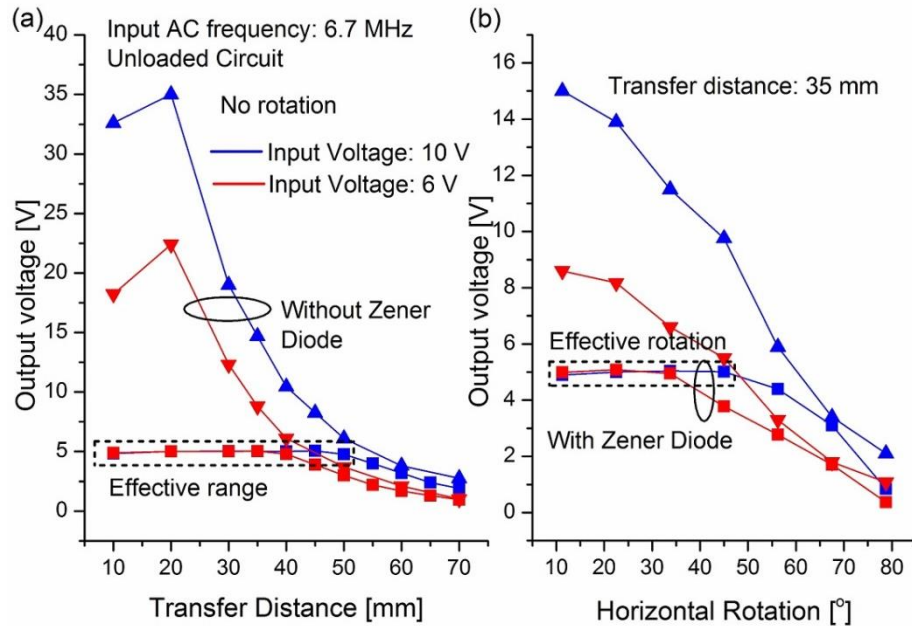


Figure 4.11 System performance with and without Zener diode for voltage control [J5].

Using a 5V Zener diode can regulate the high voltage to the Zener voltage (see square dots in Figure 4.11). Consequently, with the diode, the range where the output voltage is higher than the Zener voltage will become an effective range, and in this range the voltage output is constant. This Zener voltage will be the maximum voltage applied onto the drug delivery device, thereby determining the maximum flow rate of the pump. By increasing the input voltage or power, the effective distance range is improved (compare blue square dots and red square dots). We selected the transfer distance of 35 mm, and rotate the receiver coil, and obtain the output voltage comparison as depicted in Figure 4.11(b), showing a broader range of angles producing a constant voltage by increasing the input voltage. However, this range

of positions and angles that produce a constant voltage comes at the cost of some of the transfer efficiency.

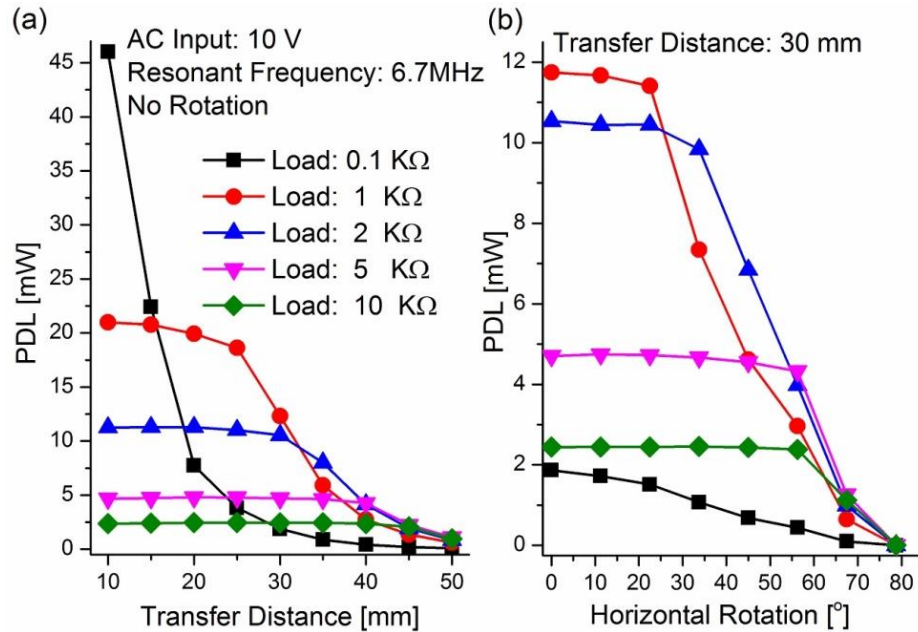


Figure 4.12 The performance comparison of power delivered to the load using different load resistances [J5].

Besides the voltage applied at the transmitter side, the resistance of the implantable device is another critical parameter that determines the power delivered to the load (PDL) [164]. To clarify the relationship between the PDL and the resistance of the load, an adjustable resistor was connected to the output of the control circuit, and the PDL was measured as a function of transfer distance and resistance value. In this test, the transmitted voltage is fixed at 10 V_{pp} level, the power received at the load is shown in Figure 4.12, which demonstrates the impact of the load on the PDL for different distances and rotation angles. In general, an increased resistance will lead to a reduced PDL; however, that lower PDL can be consistently provided for a greater range of coil positions and orientations. Thus, the selection of the resistance

should be carefully considered for this work, as it determines the actual applied power in the device and the range that the PDL can be kept constant.

The results shown in Figure 4.13 further indicate that the optimum load to achieve a maximum PDL varies with the transfer distance. The inset shows that the peak PDL decays with increasing distance, and the optimum load to achieve the peak PDL increases with increasing distance. Figures 4.12 and 4.13 reveal that a higher load resistance improves uniformity of the delivered power for a larger effective distance and rotation range, but at the cost of a reduction of the received power.

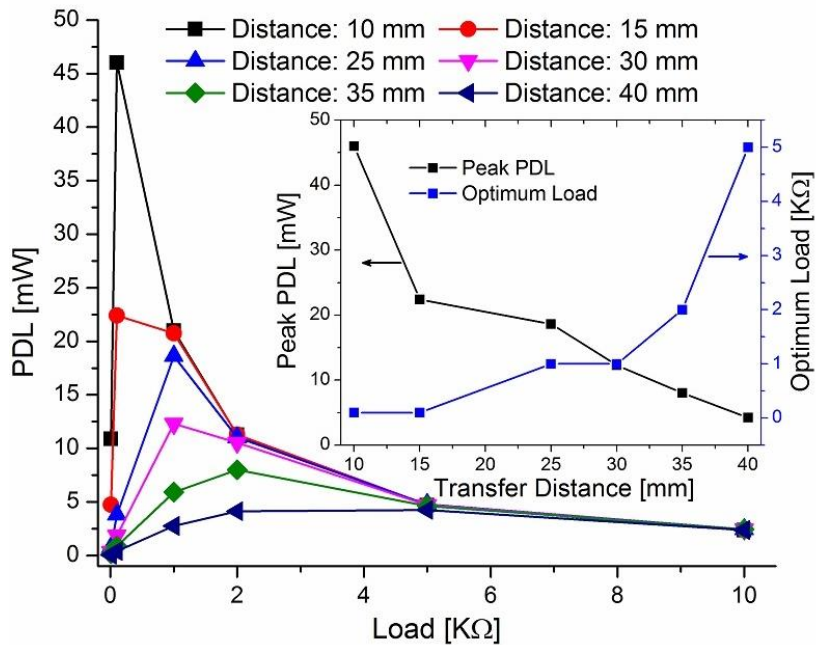


Figure 4.13 The power delivered to different loads over different distances [J5].

4.3.2 Liquid drug delivery performance evaluation

This subsection evaluates the electrolytic pump's delivery performance with the control circuit. The R-WPT system, control circuit and electrolytic pump were set up in an

experimental apparatus as depicted in Figure 4.14(a) to investigate the proof of concept drug delivery system. An AC power supply (National Instrument PXI 5402) provides an input voltage of 10 V_{pp} with a frequency of 6.7 MHz to the transmitter coil, which wirelessly transfers power to the receiver coil. The transfer distance and rotation angle can be adjusted by moving the receiver coil which is electrically connected to the control circuit. After AC to DC conversion and voltage regulation, the output of the control circuit provides a constant voltage for the drug delivery device. An adjustable resistor is connected in series with the pump. The assembled electrolytic pump is shown in the inset of Figure 4.14(a), including the Nafion coated platinum/titanium (Pt/Ti) electrodes (Figure 4.14b) and a catalytic reformer (Figure 4.14c), which are both immersed in the electrolyte chamber. The fabrication processes of the electrodes and catalytic reformer were demonstrated in Chapter 2 already.

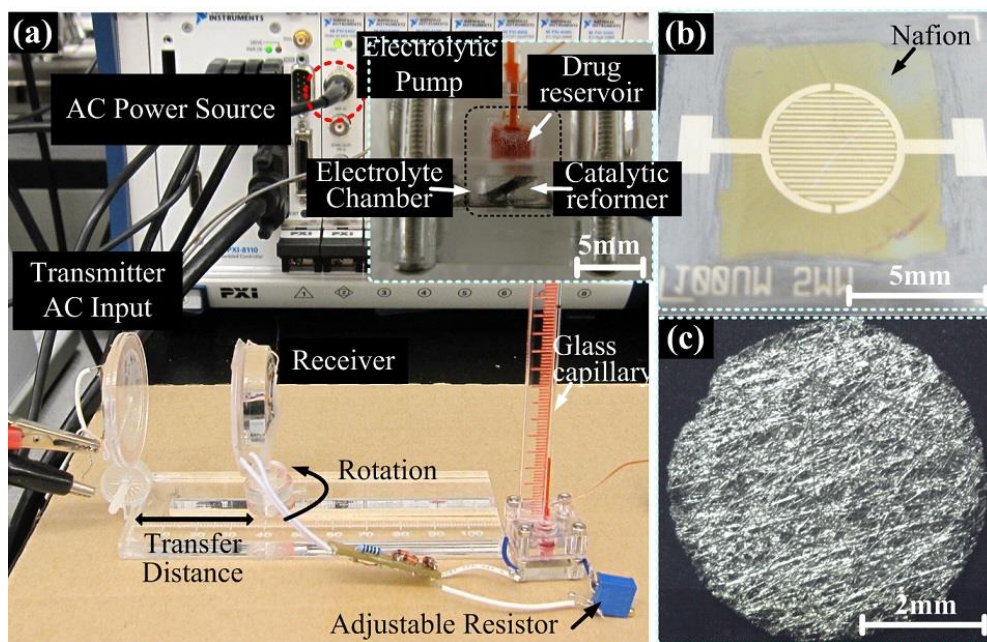


Figure 4.14 Photograph of the experimental apparatus with system components: (a) the wirelessly powered drug delivery system with a glass capillary for output measurements; (b) The interdigitated electrodes with Nafion coating; (c) the catalytic reformer [J5].

Before starting the experiment, we filled the electrolytic chamber with DI water and the reservoir with red dyed water which we used as liquid drug substitute. Once the voltage is received at the electrodes in the electrolytic chamber, the DI water (electrolyte in this work) is electrolyzed into hydrogen (H_2) and oxygen (O_2), and the expanding gas deforms the PDMS membrane. This drives the liquid in the reservoir towards the outlet, where it climbs up along the glass capillary, which enables reading the volume of the pumped fluid. Dividing the pumped volume by the time required for pumping yields the flow rate. As shown in Figure 4.15, increasing the resistance of the connected load, results in a reduced flow rate, which is due to the reduced power received at the load and pump as explained in Figures 4.12 and 4.13.

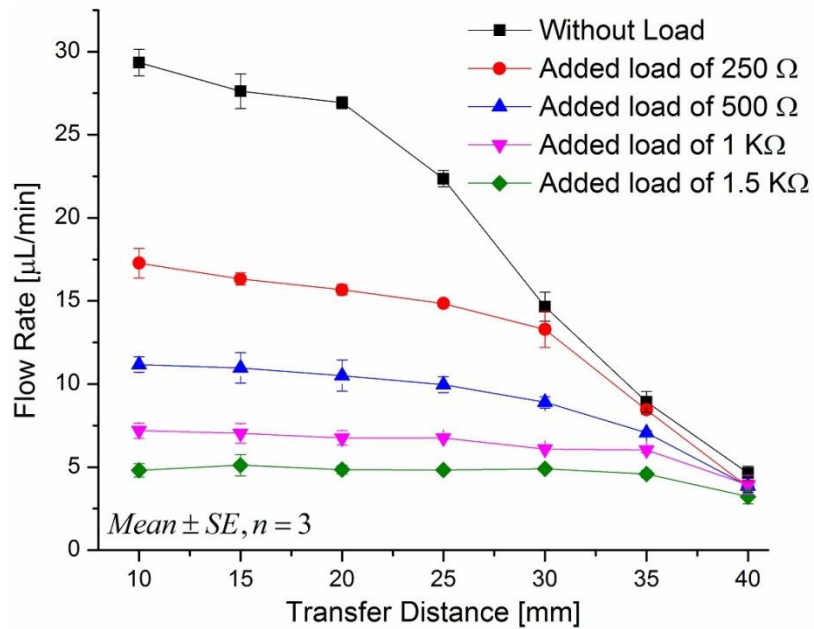


Figure 4.15 The flow rate of the electrolytic pump versus the transfer distance for different load resistance values [J5].

On the other hand, an increased resistance allows a constant flow rate to be maintained over a

longer separation distance, improving the effective distance range. For example, the pump connected with a load of $500\ \Omega$ can provide an almost constant flow rate of $11\ \mu\text{L}/\text{min}$ within the effective range of 10 mm to 15 mm, while when increasing the resistance to $1.5\ \text{K}\Omega$, the effective distance improves to up to 35 mm within which nominal flow rate of $5\ \mu\text{L}/\text{min}$ can be maintained. This is because the voltage applied at the pump is kept constant over this effective operation distance, as demonstrated in Figure 4.12. This result suggests that the flow rate can be “programmed” by choosing a specific load resistor prior to implanting the device.

Another concern for such a system is the heat generation caused by power dissipation. As mentioned, an extended transfer distance or an increased resistance of the load can lower the PDL, causing a reduced current cross the resistor at receiver side. The power loss of the Zener diode is calculated by multiplying current by the Zener voltage; therefore, it drops with an increase of the distance or the resistance. For example, when the pump provides a flow rate of about $5\ \mu\text{L}/\text{min}$ with a resistance of $1.5\ \text{K}\Omega$, the current it induced is approximate 1.7 mA. So the calculated power dissipations for the Zener diode and the resistor are 8.5 mW, 4.34 mW, respectively.

Next, we cyclically operated the pump three times in three different conditions: first, the distance between the transmitter coil and receiver coil is 10 mm, and the two coils are co-axially aligned; second, the distance is 25 mm, and receiver coil is rotated by 30° versus the transmitter coil; third, the distance is 35 mm, and the receiver coil is rotated by 30° versus the transmitter coil. From Figure 4.16, we can see that the pump with a load of $250\ \Omega$ is sensitive

to the movements between transmitter coil and receiver coil because the actuation time required for pumping the same volume depends significantly on the different conditions. A constant flow rate cannot be maintained within these movement ranges. On the other hand, when a load of 1.5 k Ω is used, the pump maintains an almost constant flow rate of approximate 5 $\mu\text{L}/\text{min}$ within the distance of up to 35 mm and rotation angle of 30°. Thus, the effective movement range has increased in this case, though at a cost of reduced flow rate. These results reveal that our remotely powered and controlled circuit model is capable of achieving a predictable flow rate after implantation despite the variation in implantation depth and angular mismatch to the transmission coil that would be expected in non-laboratory setting.

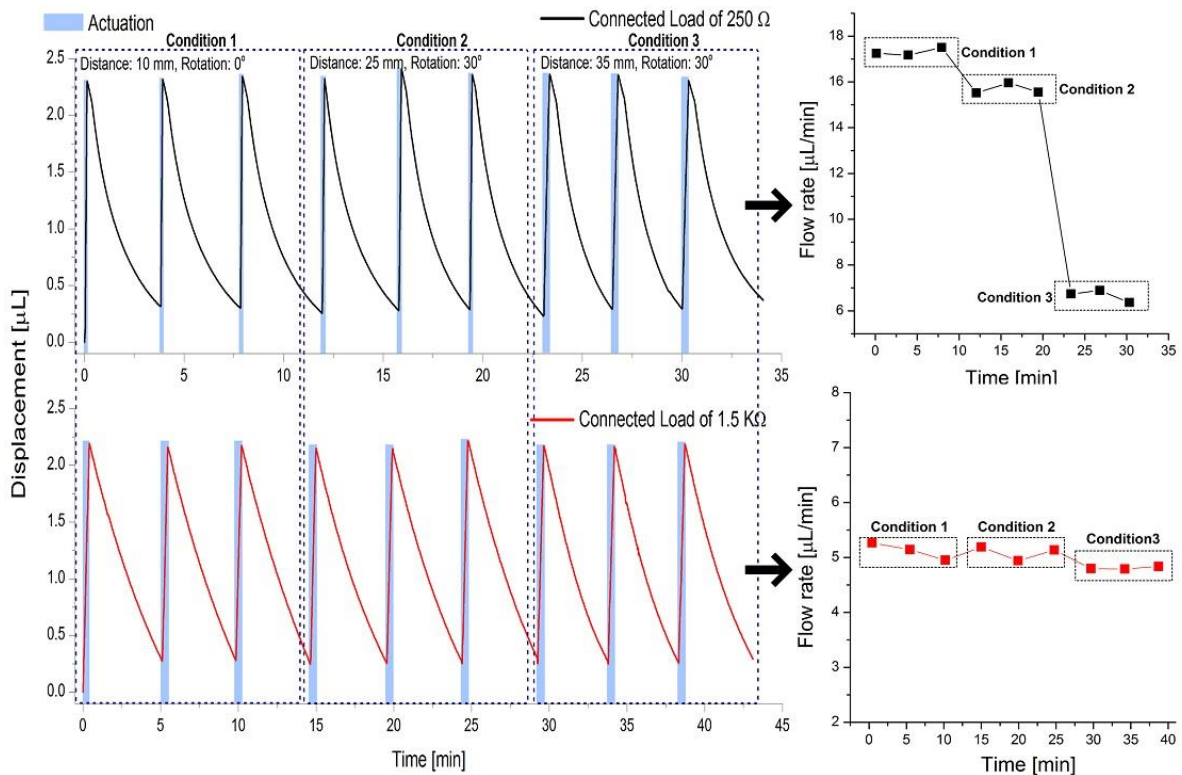


Figure 4.16 Periodic pumping pulses of the pump working at different conditions (distance and rotation), showing the impact of the load resistance on the flow rate [J5].

Within the “power off” intervals, the negative displacement of the liquid is caused by the electrolysis-bubble recombination. As the electrolytic reaction is reversible, hydrogen and oxygen are gradually recombined into water when the applied voltage is removed, which was demonstrated in Chapter 2. For the reported studies about electrolytic actuator-based drug delivery systems using liquid drug in reservoir (LDR) approach [22-24], the back flow of fluid caused by the electrolysis-bubble recombination is undesirable, since it dilutes the drug liquid, resulting in unknown dose released over time. Therefore, a variety of valves have been developed to minimize the impact of this issue [24, 49]. However, when used in combination with a SDR approach, the reverse flow is required to replenish the drug reservoir, a fast recombination rate becomes an advantage because it improves the range of possible drug doses in a given treatment time.

4.3.3 Cyclically operated solid drug delivery system

For the applications of hydrophobic drugs, for example, docetaxel (solubility of 2.5 $\mu\text{g/L}$ in water), the LDR approach cannot provide an effective solution for implantable drug delivery due to the large volume required store useful quantities of active ingredient. An alternative approach is to store the drug in its solid-form. In case of the SDR approach, small amounts of the stored solid drug are repeatedly dissolved into body fluid [30], maintaining a reproducible concentration of drug solution over an extended period of time (several months or years). The design of our electrolytic pump with the added catalytic reformer provides a suitable platform for such cyclic operation. Herein, we use solvent blue 38 as substitute for solid drug owing to its low solubility in water and its solid-form can be maintained in the reservoir for a large number of operation cycles.

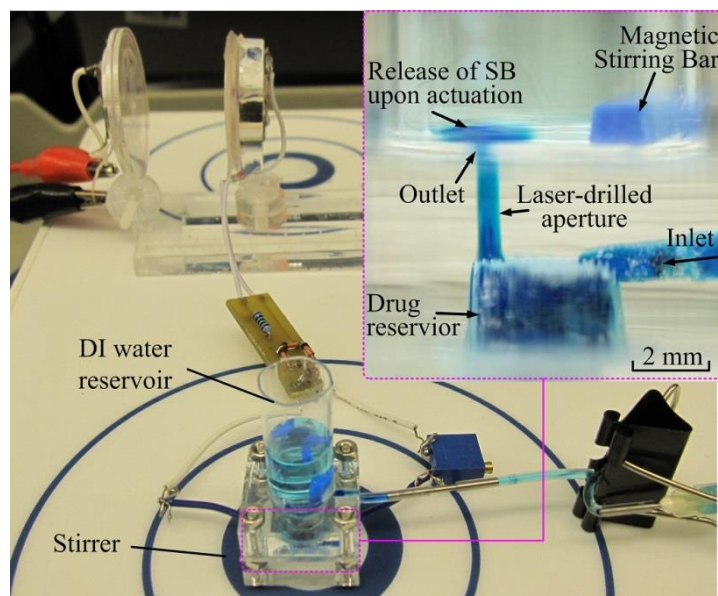


Figure 4.17 Experimental apparatus for solid drug delivery, depicting the release of solvent blue 38 into the external liquid upon the electrolytic actuation [J5].

The experimental apparatus depicted in Figure 4.17 was set up to evaluate the SDR device's dose release performance. Solvent blue 38 is placed on top of the PDMS diaphragm in powder-form, and then the electrolytic pump is assembled. DI water is slowly injected into the drug reservoir through a laser-drilled inlet (see the inset of Figure 4.17) which is clamped once the reservoir is fully filled. Another reservoir filled with DI water is placed at the outlet of the pump to which the dissolved drug solution is delivered (see the inset of Figure 4.17). The device is put on a stirrer (Advanced Multiposition Stirrer, Henry Troemner LLC, USA), and a magnetic stirring bar immersed in the external reservoir helps disperse the delivered solution in the external liquid uniformly. The concentration change of the external liquid is detected by microliter spectrophotometry (Picodrop Ltd., UK) at the end of each delivery, so that the dose released upon each actuation is measured. We used a load of 1.5 k Ω connected to the electrolytic pump, to obtain a constant amount of drug released in the different

movement conditions.

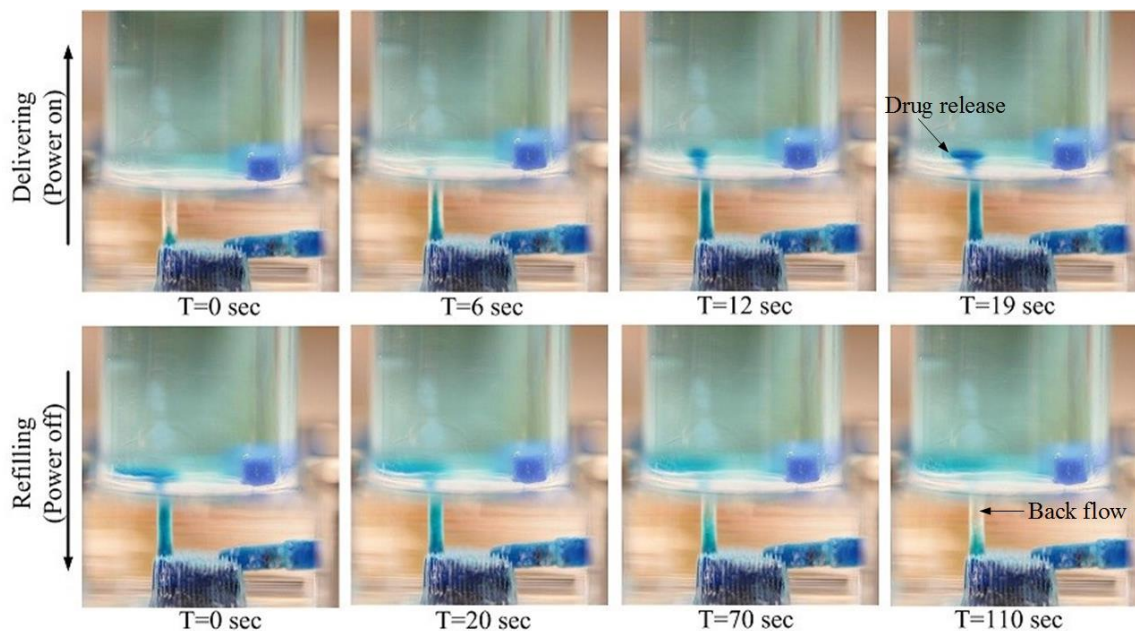


Figure 4.18 Microscope images of one cycle of drug delivery process under “power on and off” operation, illustrating the reversibility of the fluid upon the PDMS membrane’s deflection [J5].

Firstly, the setup was used to verify the two events in the cyclical operation of the SDR system: 1) pumping the dissolved drug solution during the “power on” period; 2) automatically refilling the drug reservoir within the “power off” period. The experiment was conducted, with an input voltage of 10 Vpp, and a separation distance between the transmitter coil and receiver coil, which were co-axially aligned at 10 mm. The series of images in Figure 4.18 shows one cycle of “power on and off”, verifying these two events involved in a cyclically operated SDR drug delivery process: the electrolytic pump is wirelessly powered, and driving the drug solution out of the reservoir; refilling is caused by electrolysis-bubble recombination, which draws liquid back into the reservoir to mix with the remaining drug solution. Solid drug dissolves into mixture until the reservoir once again

reaches the solubility limit of the drug.

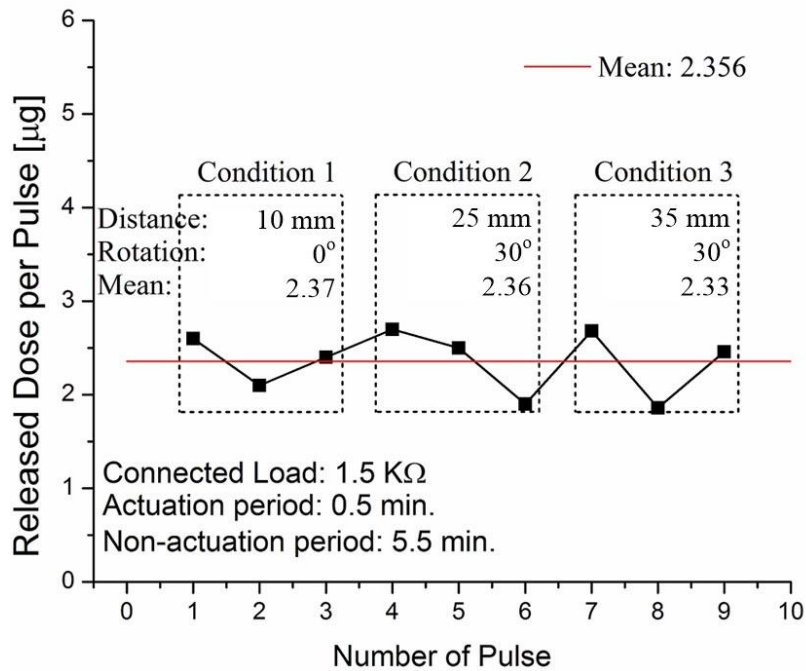


Figure 4.19 The dose of released drug per actuation for different distances between the transmitter and receiver coils as well as different rotation angles [J5].

To test the stability of the delivered dosage using the constant voltage control circuit, the experiment was conducted with an input voltage of 10 V_{pp} and different separation distances and alignments between the transmitter coil and receiver coil. For this experiment dose control was completely open loop, controlled only by the duration input signal which was kept constant for all instances of distance and angle. The system was operated under the same conditions as stated in Figure 4.16. In each condition, the device was cyclically operated “power on and off” for 3 times, with a “power on” time of 0.5 minute and a “power off” time of 5.5 minutes, which is sufficient for fully recombining the electrolysis-bubbles as demonstrated in Chapter 2. The measured dose released at each delivery cycle is shown in

Figure 4.19. As expected, the dose in each condition keeps almost constant with an average value of 2.36 $\mu\text{g}/\text{cycle}$, due to a stable flow rate achieved within the effective range of distance and orientation. This also indicates a stable drug concentration, which is due to the concentration of the pumped drug solution remaining close to the drug's maximum solubility. The experiment result reveals that an average dose of 2.36 $\mu\text{g}/\text{cycle}$ can be maintained within the maximum transfer distance of 35 mm and rotation angle of 30° for the chosen parameters. Within the effective range, our R-WPT system with an addition of a constant voltage control circuit can remotely power the electrolysis based drug delivery device and provide a well-defined release rate, thereby controlling the drug dose without feedback from the device based only on the actuation period.

4.4 Summary

This chapter presents a proof of concept electrolytic pump drug delivery system that is remotely powered and controlled by a combination of a highly efficient resonant wireless power transfer system and a constant voltage control circuit. This combination allows consistent open-loop control of the dosage based on actuation time alone, even with inconsistent placement of the transmission coil with respect to the receiving coil of the device, as expected in real life application. The feasibility of such a device for “on demand” control the dosing and release rate from an implantable drug delivery system is addressed. Our circuit design regulates the voltage applied to the electrolytic pump regardless of the distance and rotation between the transmitter and receiver coils within the effective movement range, leading to a well-defined flow rate released in the LDR device. The effective movement range can be easily modified via the input voltage at transmitter side or

via an electric load resistor at the receiver side. Similarly, the flow rate can be adjusted to meet different clinical needs by connecting different load resistors to the receiver side. The SDR approach is also evaluated for our system, and for the chosen experimental parameters, a constant dose of 2.36 μg at each delivery cycle is maintained within the effective movement range of 35 mm and 30°.

Chapter 5 Conclusion

5.1 Discussion and summary

Implantable drug delivery technologies have several critical advantages over conventional drug delivery methods, such as high efficiency delivery, long term use, compliance with patients' demands, and lack of frequent surgical or invasive requirements. For a mature design of an implantable drug delivery system, the major concerns include voltage requirement, power consumption, operational lifetime, stability of actuation force, accuracy and controllability of released dose. In this dissertation, we created a proof-of-concept drug delivery system involving an easily operated electrolytic pump, an efficient cyclical delivery mechanism, an optimized R-WPT circuit and an accurate dose control approach.

The actuator is a critical component for drug delivery device. Most reported studies using electrolytic pump based drug delivery, adopt a LDR. In that case, the bubble recombination is detrimental to the control of the system and requires strict control to avoid back flow. Our electrolytic pump using the SDR approach requires back flow to refill the reservoir between doses, which turns the problematic bubble recombination into a positive feature. Our system allows long-term therapeutic applications and avoids drug refill related surgeries, it is especially applicable for the drugs with low aqueous solubility, because the solid drug storage method provides a significantly greater storage of drugs and needs fewer refills than LDR systems of equivalent volumes. For example, the density is 25% to store 3 mg of drug in this work, optimization of the chamber size to dose volume ratio could be performed to allow for significantly higher drug storage densities. For those special diseases that needs less

daily drug dose, such as posterior uveitis, a fluocinonolone acetonide implant can be used, which releases the drug at a rate of 0.6 $\mu\text{g}/\text{day}$ for treatment [202]. The daily dose of approximately 0.001 μg to 10 μg of taxane compounds was administered for treating eye disease [203]. Even 3 mg of drug storage can provide 10 μg of daily dose over 300 days or 0.6 μg of daily dose over 5000 days. The frequency of replacement of our device is far less than the previously reported new liquid drug refilled frequency of 33 days to 3 months [23], which makes it ideal for long-term applications.

A single dose of drug solution is delivered when the power is applied on the pump, once the power is removed, the electrolysis-bubbles start to recombine, the pressure decrease in the electrolyte chamber, results in drawing human liquid back into the reservoir to dissolve some of the remaining solid drug. This “automatic refilling” forms a reproducible drug concentration ready for the next dose. By cyclically turning the power on and off, the drug doses can be repeatedly delivered. The released dose is controlled by the number of the actuation cycles, applied power strength, and actuation duration. A catalytic reformer was designed, contributing to the shorter delivery cycle by increasing the bubble recombination rate, which in turn increases the possible dose release range within a given treatment period. Our electrolytic pump using the Pt coated carbon fiber meshes was evaluated by the cumulative release profile of solvent blue 38 that is used as a drug substitute in cyclic operations. The experimental results demonstrate a controllable drug release rate of $11.44 \pm 0.56 \mu\text{g}/\text{min}$ per actuation for multiple pulses using a nominal applied power of 4 mW.

In order to prevent undesired drug diffusion during the off state of the device, a thermo-

responsive valve was implemented to control the exit port of the drug delivery device. The entire drug delivery system is “remotely” operated by an AC electromagnetic field (40.5 mT, 450 kHz) that provides the power for the pump and the valve. The valve is made of a magnetic composite consisting of the PNIPAM hydrogel and iron powder. When the electromagnetic field is on, the heat generated in the iron powder via magnetic losses causes the PNIPAM to shrink, opening the valve. When the electromagnetic field is off, the PNIPAM swells, sealing the outlet. Due to the electrolysis-bubble recombination, the fresh fluid from outside the pump refills the drug reservoir until the valve is fully sealed. The recombination can be accelerated by the catalytic reformer, allowing more fluid to flow back to the drug reservoir and dissolve the drug. By repeatedly turning on and off the magnetic field, the drug solution can be delivered cyclically, which was demonstrated experimentally.

The selection of the desired release profile for a particular treatment will ultimately determine the optimal magnetically triggered drug delivery design to use, because the power received for activating the pump can be adjusted by increasing or decreasing the size of the inductive coil, and the opening time of the PNIPAM valve also can be controlled by the amount of the iron powder or electromagnetic field strength. Moreover, PNIPAM has a LCST of about 32°C, its modified copolymers would be selected for the implantable drug delivery as these polymers have the LCST close to the physiological temperature (37°C) [28]. Besides temperature, pH value that varies in different tissues and cellular compartments is another factor influencing the shrinking and swelling behaviors of PNIPAM hydrogel for implantable applications. More detailed verification for the PNIPAM’s performance in body’s temperature and pH ranges needs to be performed in future implantable drug delivery studies.

Besides the electromagnetic induction, WPT technology also exhibits a potential for powering the implantable devices. The electrolytic pump requires low power and voltage to work, which makes integration with WPT possible. In this dissertation, a R-WPT system was set up, using 3 inductive coils and capacitors to form a circuit model with the same resonance frequency of 6.76 MHz. A novel design of winding two Litz coils together into a pancake configuration on a single layer, not only reduced the thickness, but also achieved a high Q -factor and PTE after optimized the geometry of the coils. As the received power is sensitive to the relative movements between the transmitter and receiver, a voltage control circuit is further added in order to maintain a constant voltage output for the electrolytic actuator within the effective range, which contributes to a predictable dose. This dose control approach also can provide different release rates (or dose) by electrically connecting different resistances at the implantable side. Our experiments verify that our system is capable of providing a constant dose of 2.36 $\mu\text{g/pulse}$ over an operation distance of 35 mm and rotation angle of up to 30° . Finally, the technologies demonstrated in this dissertation provide feasible platforms for “on demand” drug delivery with dose control and long term application.

5.2 Contributions for Ph.D Program (2012 May-2016 June)

Journals

- [J1]. **Ying Yi**, Ulrich Buttner, A. C. A. Arpys, Conchouso David and Ian Foulds. (2015). A pulsed mode electrolytic drug delivery device, *Journal of Micromechanics and Microengineering*, 25(10), 105011.
- [J2]. **Ying Yi**, Ulrich Buttner, and Ian Foulds. (2015). A Cyclically Actuated Electrolytic Drug Delivery Device, *Lab on a chip*, 15(17), 3540-3548.

- [J3]. **Ying Yi**, Amir Zaher, Omar Yassine, Jurgen Kosel and Ian Foulds. (2015). A remotely operated drug delivery system with an electrolytic pump and a thermo-responsive valve, *Biomicrofluidics*, 9(5), 052608.
- [J4]. **Ying Yi**, Ulrich Buttner, Yiqiang Fan and Ian Foulds. (2015). Design and Optimization of a 3-Coil Resonance-based Wireless Power Transfer System for Biomedical Implants, *International Journal of Circuit Theory and Applications*, 43(10), 1379–1390.
- [J5]. **Ying Yi**, Jurgen Kosel and Ian Foulds. (2016). A remotely powered electrolytic actuator with dose control for implantable drug delivery. Submitted to *IEEE Transactions on Biomedical Circuits and Systems*.
- [J6]. Yiqiang Fan, Huawei Li, **Ying Yi**, and Ian Foulds. (2014). PMMA to Polystyrene bonding for polymer based microfluidic systems, *Microsystem Technologies*, 20(1), 59-64.
- [J7]. Yiqiang Fan, Huawei Li, **Ying Yi**, and Ian Foulds. (2013). Laser micromachined wax-covered plastic paper as both sputter deposition shadow masks and deep-ultraviolet patterning masks for polymethylmethacrylate-based microfluidic systems, *Journal of Micro-Nanolithography, MEMS, and MOEMS*, 12(4), 049701.

Conference proceeding

- [C1]. **Ying Yi**, Ulrich Buttner and Ian Foulds. (2013). Towards an implantable pulsed mode electrolytic drug delivery system, *μTAS*, 527-529.
- [C2]. **Ying Yi**, Amir Zaher, Ulrich Buttner, Omar Yassine, Jurgen Kosel and Ian Foulds. (2015). Electromagnetically powered electrolytic pump and thermo-responsive valve for drug delivery, *IEEE-NEMS*, 5-8. **(Best Paper in Micro/Nano Fluidics Award)**
- [C3]. David Conchouso, A. Arevalo, David Castro, **Ying Yi**, and Ian Foulds. (2015). Simulation of Constant-Volume Droplet Generators for Parallelization Purposes, *COMSOL*, 1-4.

- [C4]. Arpys Arevalo, David Conchouso, David Castro, Marlon Diaz, **Ying Yi**, and Ian Foulds. (2015). Simulation of Buckled Cantilever Plate with Thermal Bimorph Actuators, *COMSOL*, 1-7.
- [C5]. **Ying Yi**, Ulrich Buttner, A. A. A. Carreno and Ian Foulds. (2014). An Improved Electrolytic Pump for Potential Drug Delivery Applications, *BIODEVICES*, 295-298.
- [C6]. Huawei Li, Yiqiang Fan, **Ying Yi** and Ian Foulds. (2013). Surface Tension-Induced High Aspect-Ratio PDMS Micropillars With Concave And Convex Lens Tips, *IEEE-NEMS*, 187-190.
- [C7]. Yiqiang Fan, Huawei Li, **Ying Yi** and Ian Foulds. (2013). Low-Cost Rapid Prototyping of Flexible Plastic Paper Based Microfluidic Devices, *IEEE-NEMS*, 175-178.
- [C8]. **Ying Yi**, Ulrich Buttner, Yiqiang Fan and Ian Foulds. (2013). 3-Coil Resonance-based Wireless Power Transfer System for Implantable Electronic, *IEEE-WPT*, 230-233.

US patent

- [P1]. Ian Foulds, Ulrich Buttner, **Ying Yi**, “Drug Delivery Device Including Electrolytic Pump.” (US 2016/0089490 A1).

Invited conference talk

- [T1]. Conference: Advances in Microfluidics & Nanofluidics (AMN), Taiwan, 2014.
Talk title: A remotely operated drug delivery system with an electrolytic pump and magnetically triggered thermo-sensitive valve.
Speaker: **Ying Yi**.

5.3 Future directions

The design, fabrication and integration of the components for implantable drug delivery systems were investigated in this dissertation, providing a feasible candidate and a simple

operation for long-term usage and dose control. However, this work still needs to be improved in the future. The future development direction includes the following:

- The pharmaceutical optimization of solid drug for SDR systems.

As SDR system requires reverse fluid to replenish the drug reservoir, the solid drug's solubility and dissolving time need to be carefully considered for practical applications. The drug with a high solubility will be consumed within only a few refilling cycles and dose control will revert back to an LDR system, while a super low solubility may not provide sufficient dose. Dissolving time also affects the stable dose release performance, pharmaceutical compound must be adjusted in order to obtain a faster drug dissolving time than electrolysis-bubble recombination rate, otherwise, the drug concentration in the reservoir varies at each refilling, that makes the dose released uncontrolled. Moreover, suspension of undissolved drug powder in the solution must be avoided, which gives a strict requirement for pharmaceutical industry.

- The miniaturization of the system.

As shown in the experimental apparatus, the PNIPAM valve and the electrolytic pump are not tightly assembled. In the future works, an optimized valve model should be designed in order to make a compact integration with the pump's outlet, so the fluid outside the valve can be drawn back to the drug reservoir. Moreover, a highly integrated chip that performs same functions of the LC circuit and the constant voltage control circuit needs to be developed, as it can strongly miniaturize the size of our drug delivery system.

- “smart and highly integrated microsystem” based drug delivery.

This kind of system indicates the future development direction, it is able to: (1) monitor the physiological conditions inside the patient’s body and respond to them by means of chemical transducers or biosensor; (2) deliver the appropriate amount of drugs by controlling the micro-actuators according to the signal detected. Data transmission needs wireless communication technology, which may require a sophisticated design and fabrication. Following the works in this dissertation, an easily operated approach that is capable of timely monitoring and controlling the released dose or flow rate is briefly introduced here. Embedding piezoresistive materials (for example, carbon nanotube or graphene) into the PDMS membrane can act as a physical sensor. Once the membrane is deformed, its impedance changes accordingly. Impedance match theory indicates that a resistance change at the receiver side can contribute to a current change at the transmitter side. In other words, if the relationship between the resistance change of the membrane and its deformation is confirmed, the pumped volume can be expressed via the current change at the external device. This “on demand” drug delivery system would not only precisely control the dose to meet the patients’ particular therapeutic requirements, but also provides feedback to avoid over-dosing or overdriving the actuator past its maximum safe limit.

5.4 Final conclusion

Improving on the reported studies on electrolytic actuator based drug delivery systems, this dissertation further combines an SDR approach with a cyclical actuation mode, which is intended to provide a solution for high density drug storage and turn problematic bubble

recombination into a positive feature. The PNIPAM hydrogel valve allows reverse flow to replenish the drug reservoir within a limited closing time and properly seals the outlet of the device to prevent drug diffusion over a long period. The valve shares the same remote power source of the actuator, which is able to contribute to a more compact design for future drug delivery systems. The catalytic reformer is created to accelerate the bubble recombination, as a result, it not only increases the range of possible doses of the drug within a given operation time, but also ensures more back flow to refill the drug reservoir within the valve's closing time. The R-WPT that acts as an effective external power stimulus extends the implantable device's lifetime, avoiding surgical operations for power source replacement. The addition of the constant voltage control circuit makes the release rate and dose known to patients without any complicated closed-loop sensor, as long as the distance and rotation between the transmitter and receiver coils are within an effective movement range. This greatly increases the flexibility in the positioning of the powering coils and facilitates the practical operations. This proof of concept work paves the way towards a "smart and highly integrated" drug delivery system in the future.

Bibliography

- [1] S. Z. Razzacki, P. K. Thwar, M. Yang, V. M. Ugaz, and M. A. Burns, "Integrated microsystems for controlled drug delivery," *Advanced drug delivery reviews*, vol. 56, pp. 185-198, 2004.
- [2] D. C. Metrikin and R. Anand, "Intravitreal drug administration with depot devices," *Current opinion in ophthalmology*, vol. 5, pp. 21-29, 1994.
- [3] E. Meng and T. Hoang, "MEMS-enabled implantable drug infusion pumps for laboratory animal research, preclinical, and clinical applications," *Advanced drug delivery reviews*, vol. 64, pp. 1628-1638, 2012.
- [4] Y. Li, H. L. H. Duc, B. Tyler, T. Williams, M. Tupper, R. Langer, *et al.*, "In vivo delivery of BCNU from a MEMS device to a tumor model," *Journal of controlled release*, vol. 106, pp. 138-145, 2005.
- [5] H. F. Edelhauser, C. L. Rowe-Rendleman, M. R. Robinson, D. G. Dawson, G. J. Chader, H. E. Grossniklaus, *et al.*, "Ophthalmic drug delivery systems for the treatment of retinal diseases: basic research to clinical applications," *Investigative ophthalmology & visual science*, vol. 51, pp. 5403-5420, 2010.
- [6] J. H. Prescott, S. Lipka, S. Baldwin, N. F. Sheppard, J. M. Maloney, J. Coppeta, *et al.*, "Chronic, programmed polypeptide delivery from an implanted, multireservoir microchip device," *Nature biotechnology*, vol. 24, pp. 437-438, 2006.
- [7] D. A. Lavan, T. McGuire, and R. Langer, "Small-scale systems for in vivo drug delivery," *Nature biotechnology*, vol. 21, pp. 1184-1191, 2003.
- [8] A. Göpferich, "Mechanisms of polymer degradation and erosion," *Biomaterials*, vol. 17, pp. 103-114, 1996.
- [9] R. Yoshida, "Design of functional polymer gels and their application to biomimetic

- materials," *Current Organic Chemistry*, vol. 9, pp. 1617-1641, 2005.
- [10] K. E. Uhrich, S. M. Cannizzaro, R. S. Langer, and K. M. Shakesheff, "Polymeric systems for controlled drug release," *Chemical reviews*, vol. 99, pp. 3181-3198, 1999.
- [11] W. Wei, L. Yuan, G. Hu, L. Y. Wang, J. Wu, X. Hu, *et al.*, "Monodisperse chitosan microspheres with interesting structures for protein drug delivery," *Advanced Materials*, vol. 20, pp. 2292-2296, 2008.
- [12] Y. Itoh, M. Matsusaki, T. Kida, and M. Akashi, "Locally controlled release of basic fibroblast growth factor from multilayered capsules," *Biomacromolecules*, vol. 9, pp. 2202-2206, 2008.
- [13] H. Chen, R. C. MacDonald, S. Li, N. L. Krett, S. T. Rosen, and T. V. O'Halloran, "Lipid encapsulation of arsenic trioxide attenuates cytotoxicity and allows for controlled anticancer drug release," *Journal of the American Chemical Society*, vol. 128, pp. 13348-13349, 2006.
- [14] B. G. De Geest, R. E. Vandenbroucke, A. M. Guenther, G. B. Sukhorukov, W. E. Hennink, N. N. Sanders, *et al.*, "Intracellularly degradable polyelectrolyte microcapsules," *Advanced materials*, vol. 18, pp. 1005-1009, 2006.
- [15] P. D. Thornton, R. J. Mart, and R. V. Ulijn, "Enzyme-Responsive Polymer Hydrogel Particles for Controlled Release," *Advanced Materials*, vol. 19, pp. 1252-1256, 2007.
- [16] N. S. Satarkar and J. Z. Hilt, "Magnetic hydrogel nanocomposites for remote controlled pulsatile drug release," *Journal of Controlled Release*, vol. 130, pp. 246-251, 2008.
- [17] S. Herrlich, S. Spieth, S. Messner, and R. Zengerle, "Osmotic micropumps for drug delivery," *Advanced drug delivery reviews*, vol. 64, pp. 1617-1627, 2012.
- [18] K. Cai, Z. Luo, Y. Hu, X. Chen, Y. Liao, L. Yang, *et al.*, "Magnetically triggered

- reversible controlled drug delivery from microfabricated polymeric multireservoir devices," *Advanced Materials*, vol. 21, pp. 4045-4049, 2009.
- [19] D. J. Laser and J. G. Santiago, "A review of micropumps," *Journal of micromechanics and microengineering*, vol. 14, p. R35, 2004.
- [20] W. M. Saltzman and W. L. Olbricht, "Building drug delivery into tissue engineering design," *Nature Reviews Drug Discovery*, vol. 1, pp. 177-186, 2002.
- [21] B. Ziaie, A. Baldi, M. Lei, Y. Gu, and R. A. Siegel, "Hard and soft micromachining for BioMEMS: review of techniques and examples of applications in microfluidics and drug delivery," *Advanced drug delivery reviews*, vol. 56, pp. 145-172, 2004.
- [22] P.-Y. Li, R. Sheybani, C. A. Gutierrez, J. T. Kuo, and E. Meng, "A parylene bellows electrochemical actuator," *Microelectromechanical Systems, Journal of*, vol. 19, pp. 215-228, 2010.
- [23] P.-Y. Li, J. Shih, R. Lo, S. Saati, R. Agrawal, M. S. Humayun, *et al.*, "An electrochemical intraocular drug delivery device," *Sensors and Actuators A: Physical*, vol. 143, pp. 41-48, 2008.
- [24] H. Gensler, R. Sheybani, P.-Y. Li, R. L. Mann, and E. Meng, "An implantable MEMS micropump system for drug delivery in small animals," *Biomedical microdevices*, vol. 14, pp. 483-496, 2012.
- [25] R. Lo, P.-Y. Li, S. Saati, R. N. Agrawal, M. S. Humayun, and E. Meng, "A passive MEMS drug delivery pump for treatment of ocular diseases," *Biomedical microdevices*, vol. 11, pp. 959-970, 2009.
- [26] P.-Y. Li, T. K. Givrad, R. Sheybani, D. P. Holschneider, J.-M. I. Maarek, and E. Meng, "A low power, on demand electrothermal valve for wireless drug delivery applications," *Lab on a Chip*, vol. 10, pp. 101-110, 2010.

- [27] S. Ghosh, C. Yang, T. Cai, Z. Hu, and A. Neogi, "Oscillating magnetic field-actuated microvalves for micro-and nanofluidics," *Journal of Physics D: Applied Physics*, vol. 42, p. 135501, 2009.
- [28] T.-Y. Liu, S.-H. Hu, D.-M. Liu, S.-Y. Chen, and I.-W. Chen, "Biomedical nanoparticle carriers with combined thermal and magnetic responses," *Nano Today*, vol. 4, pp. 52-65, 2009.
- [29] B. R. Saunders and B. Vincent, "Microgel particles as model colloids: theory, properties and applications," *Advances in colloid and interface science*, vol. 80, pp. 1-25, 1999.
- [30] F. N. Pirmoradi, J. K. Jackson, H. M. Burt, and M. Chiao, "On-demand controlled release of docetaxel from a battery-less MEMS drug delivery device," *Lab on a Chip*, vol. 11, pp. 2744-2752, 2011.
- [31] A. C. R. Grayson, R. S. Shawgo, A. M. Johnson, N. T. Flynn, Y. Li, M. J. Cima, *et al.*, "A BioMEMS review: MEMS technology for physiologically integrated devices," *Proceedings of the IEEE*, vol. 92, pp. 6-21, 2004.
- [32] M. Ngoepe, Y. E. Choonara, C. Tyagi, L. K. Tomar, L. C. Du Toit, P. Kumar, *et al.*, "Integration of biosensors and drug delivery technologies for early detection and chronic management of illness," *Sensors*, vol. 13, pp. 7680-7713, 2013.
- [33] S. Rahimi, E. H. Sarraf, G. K. Wong, and K. Takahata, "Implantable drug delivery device using frequency-controlled wireless hydrogel microvalves," *Biomedical microdevices*, vol. 13, pp. 267-277, 2011.
- [34] T. Tang, S. Smith, B. Flynn, J. Stevenson, A. Gundlach, H. Reekie, *et al.*, "Implementation of wireless power transfer and communications for an implantable ocular drug delivery system," *Nanobiotechnology, IET*, vol. 2, pp. 72-79, 2008.
- [35] K. Stangel, S. Kolnsberg, D. Hammerschmidt, B. Hosticka, H. Trieu, and W. Mokwa,

- "A programmable intraocular CMOS pressure sensor system implant," *Solid-State Circuits, IEEE Journal of*, vol. 36, pp. 1094-1100, 2001.
- [36] B. Ziaie, "Implantable Wireless Microsystems," in *BioMEMS and Biomedical Nanotechnology*, ed: Springer, 2006, pp. 205-221.
- [37] R. Sheybani, A. Cobo, and E. Meng, "Wireless programmable electrochemical drug delivery micropump with fully integrated electrochemical dosing sensors," *Biomedical microdevices*, vol. 17, pp. 1-13, 2015.
- [38] H. K. A. Tsai, E. A. Moschou, S. Daunert, M. Madou, and L. Kulinsky, "Integrating Biosensors and Drug Delivery: A Step Closer Toward Scalable Responsive Drug - Delivery Systems," *Advanced Materials*, vol. 21, pp. 656-660, 2009.
- [39] M. Privman, T. K. Tam, V. Bocharova, J. Halánek, J. Wang, and E. Katz, "Responsive interface switchable by logically processed physiological signals: Toward "smart" actuators for signal amplification and drug delivery," *ACS applied materials & interfaces*, vol. 3, pp. 1620-1623, 2011.
- [40] T. Florian, G. Frank, F. Hagen, and M. Eike, "A highly integrated dosing system for drug delivery applications," In *17th International Conference on Miniaturized Systems for Chemistry and Life Sciences (μ TAS)*, pp. 826-828, 2013.
- [41] T. Hoare, J. Santamaria, G. F. Goya, S. Irusta, D. Lin, S. Lau, *et al.*, "A magnetically triggered composite membrane for on-demand drug delivery," *Nano letters*, vol. 9, pp. 3651-3657, 2009.
- [42] J. Miyakoshi, M. Yoshida, K. Shibuya, and M. Hiraoka, "Exposure to strong magnetic fields at power frequency potentiates X-ray-induced DNA strand breaks," *Journal of radiation research*, vol. 41, pp. 293-302, 2000.
- [43] H. Lai and N. P. Singh, "Magnetic-field-induced DNA strand breaks in brain cells of the rat," *Environmental Health Perspectives*, vol. 112, p. 687, 2004.

- [44] A. K. RamRakhyani, S. Mirabbasi, and M. Chiao, "Design and optimization of resonance-based efficient wireless power delivery systems for biomedical implants," *Biomedical Circuits and Systems, IEEE Transactions on*, vol. 5, pp. 48-63, 2011.
- [45] B. Tang, G. Cheng, J.-C. Gu, and C.-H. Xu, "Development of solid self-emulsifying drug delivery systems: preparation techniques and dosage forms," *Drug discovery today*, vol. 13, pp. 606-612, 2008.
- [46] R. Lo, P.-Y. Li, S. Saati, R. Agrawal, M. S. Humayun, and E. Meng, "A refillable microfabricated drug delivery device for treatment of ocular diseases," *Lab on a Chip*, vol. 8, pp. 1027-1030, 2008.
- [47] H. D. Williams, N. L. Trevaskis, S. A. Charman, R. M. Shanker, W. N. Charman, C. W. Pouton, *et al.*, "Strategies to address low drug solubility in discovery and development," *Pharmacological reviews*, vol. 65, pp. 315-499, 2013.
- [48] R. Sheybani and E. Meng, "High-efficiency MEMS electrochemical actuators and electrochemical impedance spectroscopy characterization," *Microelectromechanical Systems, Journal of*, vol. 21, pp. 1197-1208, 2012.
- [49] R. Lo and E. Meng, "A modular heat-shrink-packaged check valve with high pressure shutoff," *Microelectromechanical Systems, Journal of*, vol. 20, pp. 1163-1173, 2011.
- [50] H.-P. Lee and W. Ryu, "Wet microcontact printing (μ CP) for micro-reservoir drug delivery systems," *Biofabrication*, vol. 5, p. 025011, 2013.
- [51] Y. E. Choonara, V. Pillay, M. P. Danckwerts, T. R. Carmichael, and L. C. Du Toit, "A review of implantable intravitreal drug delivery technologies for the treatment of posterior segment eye diseases," *Journal of pharmaceutical sciences*, vol. 99, pp. 2219-2239, 2010.
- [52] C. L. Stevenson, J. T. Santini, and R. Langer, "Reservoir-based drug delivery systems utilizing microtechnology," *Advanced drug delivery reviews*, vol. 64, pp. 1590-1602,

- 2012.
- [53] G. E. Sanborn, R. Anand, R. E. Torti, S. D. Nightingale, S. X. Cal, B. Yates, *et al.*, "Sustained-release ganciclovir therapy for treatment of cytomegalovirus retinitis: use of an intravitreal device," *Archives of ophthalmology*, vol. 110, pp. 188-195, 1992.
- [54] T. J. Smith, P. A. Pearson, D. L. Blandford, J. D. Brown, K. A. Goins, J. L. Hollins, *et al.*, "Intravitreal sustained-release ganciclovir," *Archives of ophthalmology*, vol. 110, pp. 255-258, 1992.
- [55] P. Mruthyunjaya, D. Khalatbari, P. Yang, S. Stinnett, R. Tano, P. Ashton, *et al.*, "Efficacy of low-release-rate fluocinolone acetonide intravitreal implants to treat experimental uveitis," *Archives of Ophthalmology*, vol. 124, pp. 1012-1018, 2006.
- [56] G. Y. Kim, B. M. Tyler, M. M. Tupper, J. M. Karp, R. S. Langer, H. Brem, *et al.*, "Resorbable polymer microchips releasing BCNU inhibit tumor growth in the rat 9L flank model," *Journal of Controlled Release*, vol. 123, pp. 172-178, 2007.
- [57] W. Ryu, Z. Huang, F. B. Prinz, S. B. Goodman, and R. Fasching, "Biodegradable micro-osmotic pump for long-term and controlled release of basic fibroblast growth factor," *Journal of Controlled Release*, vol. 124, pp. 98-105, 2007.
- [58] T. Goettsche, A. Schumacher, J. Kohnle, S. Messner, and R. Zengerle, "Highly integrated oral drug delivery system with valve based on electro-active-polymer," in *Micro Electro Mechanical Systems, 2007. MEMS. IEEE 20th International Conference on*, 2007, pp. 461-464.
- [59] M. Staples, K. Daniel, M. J. Cima, and R. Langer, "Application of micro-and nano-electromechanical devices to drug delivery," *Pharmaceutical research*, vol. 23, pp. 847-863, 2006.
- [60] R. A. Receveur, F. W. Lindemans, and N. F. de Rooij, "Microsystem technologies for implantable applications," *Journal of Micromechanics and Microengineering*, vol. 17,

- p. R50, 2007.
- [61] D. Reynaerts, J. Peirs, and H. Van Brussel, "An implantable drug-delivery system based on shape memory alloy micro-actuation," *Sensors and Actuators A: Physical*, vol. 61, pp. 455-462, 1997.
- [62] J. T. Santini, M. J. Cima, and R. Langer, "A controlled-release microchip," *Nature*, vol. 397, pp. 335-338, 1999.
- [63] Y. Li, R. S. Shawgo, B. Tyler, P. T. Henderson, J. S. Vogel, A. Rosenberg, *et al.*, "In vivo release from a drug delivery MEMS device," *Journal of Controlled Release*, vol. 100, pp. 211-219, 2004.
- [64] F. N. Pirmoradi, J. K. Jackson, H. M. Burt, and M. Chiao, "A magnetically controlled MEMS device for drug delivery: design, fabrication, and testing," *Lab on a Chip*, vol. 11, pp. 3072-3080, 2011.
- [65] F. N. Pirmoradi, K. Ou, J. K. Jackson, K. Letchford, J. Cui, K. T. Wolf, *et al.*, "Controlled delivery of antiangiogenic drug to human eye tissue using a MEMS device," in *Micro Electro Mechanical Systems (MEMS), 2013 IEEE 26th International Conference on*, 2013, pp. 1-4.
- [66] A. Nisar, N. Afzulpurkar, B. Mahaisavariya, and A. Tuantranont, "MEMS-based micropumps in drug delivery and biomedical applications," *Sensors and Actuators B: Chemical*, vol. 130, pp. 917-942, 2008.
- [67] N.-C. Tsai and C.-Y. Sue, "Review of MEMS-based drug delivery and dosing systems," *Sensors and Actuators A: Physical*, vol. 134, pp. 555-564, 2007.
- [68] R. Zengerle, A. Richter, and H. Sandmaier, "A micro membrane pump with electrostatic actuation," in *Micro Electro Mechanical Systems, 1992, MEMS'92, Proceedings. An Investigation of Micro Structures, Sensors, Actuators, Machines and Robot. IEEE*, 1992, pp. 19-24.

- [69] C. Cabuz, W. R. Herb, E. I. Cabuz, and S. T. Lu, "The dual diaphragm pump," in *Micro Electro Mechanical Systems, 2001. MEMS 2001. The 14th IEEE International Conference on*, 2001, pp. 519-522.
- [70] M. M. Teymoori and E. Abbaspour-Sani, "Design and simulation of a novel electrostatic peristaltic micromachined pump for drug delivery applications," *Sensors and Actuators A: Physical*, vol. 117, pp. 222-229, 2005.
- [71] A. Machauf, Y. Nemirovsky, and U. Dinnar, "A membrane micropump electrostatically actuated across the working fluid," *Journal of Micromechanics and Microengineering*, vol. 15, p. 2309, 2005.
- [72] H. Kim, A. A. Astle, K. Najafi, L. P. Bernal, and P. D. Washabaugh, "An integrated electrostatic peristaltic 18-stage gas micropump with active microvalves," *Microelectromechanical Systems, Journal of*, vol. 24, pp. 192-206, 2015.
- [73] W. Spencer, W. T. Corbett, L. Dominguez, and B. D. Shafer, "An electronically controlled piezoelectric insulin pump and valves," *Sonics and Ultrasonics, IEEE Transactions on*, vol. 25, pp. 153-156, 1978.
- [74] M. Koch, N. Harris, A. G. Evans, N. M. White, and A. Brunnschweiler, "A novel micromachined pump based on thick film piezoelectric actuation," *Sensors and Actuators A: Physical*, vol. 70, pp. 98-103, 1998.
- [75] K. Junwu, Y. Zhigang, P. Taijiang, C. Guangming, and W. Boda, "Design and test of a high-performance piezoelectric micropump for drug delivery," *Sensors and Actuators A: Physical*, vol. 121, pp. 156-161, 2005.
- [76] G.-H. Feng and E. S. Kim, "Piezoelectrically actuated dome-shaped diaphragm micropump," *Microelectromechanical Systems, Journal of*, vol. 14, pp. 192-199, 2005.
- [77] B. Ma, S. Liu, Z. Gan, G. Liu, X. Cai, H. Zhang, *et al.*, "A PZT insulin pump

- integrated with a silicon microneedle array for transdermal drug delivery," *Microfluidics and Nanofluidics*, vol. 2, pp. 417-423, 2006.
- [78] A. Geipel, A. Doll, F. Goldschmidtböing, P. Jantscheff, N. Esser, U. Massing, *et al.*, "Pressure-independent micropump with piezoelectric valves for low flow drug delivery systems," in *Micro Electro Mechanical Systems, 2006. MEMS 2006 Istanbul. 19th IEEE International Conference on*, 2006, pp. 786-789.
- [79] A. Doll, M. Heinrichs, F. Goldschmidtboeing, H.-J. Schrag, U. Hopt, and P. Woias, "A high performance bidirectional micropump for a novel artificial sphincter system," *Sensors and Actuators A: Physical*, vol. 130, pp. 445-453, 2006.
- [80] Y.-C. Hsu, S.-J. Lin, and C.-C. Hou, "Development of peristaltic antithrombogenic micropumps for in vitro and ex vivo blood transportation tests," *Microsystem Technologies*, vol. 14, pp. 31-41, 2008.
- [81] L. Cao, S. Mantell, and D. Polla, "Design and simulation of an implantable medical drug delivery system using microelectromechanical systems technology," *Sensors and Actuators A: Physical*, vol. 94, pp. 117-125, 2001.
- [82] S. Böhm, W. Olthuis, and P. Bergveld, "A plastic micropump constructed with conventional techniques and materials," *Sensors and Actuators A: Physical*, vol. 77, pp. 223-228, 1999.
- [83] S. Santra, P. Holloway, and C. D. Batich, "Fabrication and testing of a magnetically actuated micropump," *Sensors and Actuators B: Chemical*, vol. 87, pp. 358-364, 2002.
- [84] C. Yamahata, C. Lotto, E. Al-Assaf, and M. Gijs, "A PMMA valveless micropump using electromagnetic actuation," *Microfluidics and Nanofluidics*, vol. 1, pp. 197-207, 2005.
- [85] T. Pan, S. J. McDonald, E. M. Kai, and B. Ziaie, "A magnetically driven PDMS

- micropump with ball check-valves," *Journal of Micromechanics and Microengineering*, vol. 15, p. 1021, 2005.
- [86] H.-L. Yin, Y.-C. Huang, W. Fang, and J. Hsieh, "A novel electromagnetic elastomer membrane actuator with a semi-embedded coil," *Sensors and Actuators A: Physical*, vol. 139, pp. 194-202, 2007.
- [87] O. C. Jeong and S. S. Yang, "Fabrication and test of a thermopneumatic micropump with a corrugated p+ diaphragm," *Sensors and Actuators A: Physical*, vol. 83, pp. 249-255, 2000.
- [88] S. Zimmermann, J. Frank, D. Liepmann, and A. P. Pisano, "A planar micropump utilizing thermopneumatic actuation and in-plane flap valves," in *Micro Electro Mechanical Systems, 2004. 17th IEEE International Conference on.(MEMS)*, 2004, pp. 462-465.
- [89] S. R. Hwang, W. Y. Sim, D. H. Jeon, G. Y. Kim, S. S. Yang, and J. J. Pak, "Fabrication and test of a submicroliter-level thermopneumatic micropump for transdermal drug delivery," in *Microtechnology in Medicine and Biology, 2005. 3rd IEEE/EMBS Special Topic Conference on*, 2005, pp. 143-145.
- [90] O. C. Jeong, S. W. Park, S. S. Yang, and J. J. Pak, "Fabrication of a peristaltic PDMS micropump," *Sensors and Actuators A: Physical*, vol. 123, pp. 453-458, 2005.
- [91] J.-H. Kim, K.-H. Na, C. Kang, and Y.-S. Kim, "A disposable thermopneumatic-actuated micropump stacked with PDMS layers and ITO-coated glass," *Sensors and Actuators A: Physical*, vol. 120, pp. 365-369, 2005.
- [92] W. Benard, H. Kahn, A. Heuer, and M. Huff, "A titanium-nickel shape-memory alloy actuated micropump," in *Solid State Sensors and Actuators, 1997. TRANSDUCERS'97 Chicago., 1997 International Conference on*, 1997, pp. 361-364.
- [93] D. Xu, L. Wang, G. Ding, Y. Zhou, A. Yu, and B. Cai, "Characteristics and fabrication

- of NiTi/Si diaphragm micropump," *Sensors and Actuators A: Physical*, vol. 93, pp. 87-92, 2001.
- [94] E. Makino, T. Mitsuya, and T. Shibata, "Fabrication of TiNi shape memory micropump," *Sensors and Actuators A: Physical*, vol. 88, pp. 256-262, 2001.
- [95] S. Guo and T. Fukuda, "SMA actuator-based novel type of micropump for biomedical application," in *Robotics and Automation, 2004. Proceedings. ICRA'04. 2004 IEEE International Conference on*, 2004, pp. 1616-1621.
- [96] S. Zeng, C.-H. Chen, J. C. Mikkelsen, and J. G. Santiago, "Fabrication and characterization of electroosmotic micropumps," *Sensors and Actuators B: Chemical*, vol. 79, pp. 107-114, 2001.
- [97] P. Wang, Z. Chen, and H.-C. Chang, "A new electro-osmotic pump based on silica monoliths," *Sensors and Actuators B: Chemical*, vol. 113, pp. 500-509, 2006.
- [98] K.-S. Yun, I.-J. Cho, J.-U. Bu, C.-J. Kim, and E. Yoon, "A surface-tension driven micropump for low-voltage and low-power operations," *Microelectromechanical Systems, Journal of*, vol. 11, pp. 454-461, 2002.
- [99] J. Jang and S. S. Lee, "Theoretical and experimental study of MHD (magnetohydrodynamic) micropump," *Sensors and Actuators A: Physical*, vol. 80, pp. 84-89, 2000.
- [100] L. Huang, W. Wang, M. Murphy, K. Lian, and Z.-G. Ling, "LIGA fabrication and test of a DC type magnetohydrodynamic (MHD) micropump," *Microsystem technologies*, vol. 6, pp. 235-240, 2000.
- [101] A. V. Lemoff and A. P. Lee, "An AC magnetohydrodynamic micropump," *Sensors and Actuators B: Chemical*, vol. 63, pp. 178-185, 2000.
- [102] A. Homsy, S. Koster, J. C. Eijkel, A. van den Berg, F. Lucklum, E. Verpoorte, *et al.*,

- "A high current density DC magnetohydrodynamic (MHD) micropump," *Lab on a Chip*, vol. 5, pp. 466-471, 2005.
- [103] Y.-C. Su, L. Lin, and A. P. Pisano, "A water-powered osmotic microactuator," *Microelectromechanical Systems, Journal of*, vol. 11, pp. 736-742, 2002.
- [104] Y.-C. Su and L. Lin, "A water-powered micro drug delivery system," *Microelectromechanical Systems, Journal of*, vol. 13, pp. 75-82, 2004.
- [105] D. A. Ateya, A. A. Shah, and S. Z. Hua, "An electrolytically actuated micropump," *Review of scientific instruments*, vol. 75, pp. 915-920, 2004.
- [106] S.-H. Chiu and C.-H. Liu, "An air-bubble-actuated micropump for on-chip blood transportation," *Lab on a Chip*, vol. 9, pp. 1524-1533, 2009.
- [107] S. C. Terry, J. H. Jerman, and J. B. Angell, "A gas chromatographic air analyzer fabricated on a silicon wafer," *Electron Devices, IEEE Transactions on*, vol. 26, pp. 1880-1886, 1979.
- [108] K. W. Oh and C. H. Ahn, "A review of microvalves," *Journal of micromechanics and microengineering*, vol. 16, p. R13, 2006.
- [109] E. Yang, S. Han, and S. Yang, "Fabrication and testing of a pair of passive bivalvular microvalves composed of p⁺ silicon diaphragms," *Sensors and Actuators A: Physical*, vol. 57, pp. 75-78, 1996.
- [110] D. Bien, S. Mitchell, and H. Gamble, "Fabrication and characterization of a micromachined passive valve," *Journal of micromechanics and microengineering*, vol. 13, p. 557, 2003.
- [111] M. Hu, H. Du, S.-F. Ling, Y. Fu, Q. Chen, L. Chow, *et al.*, "A silicon-on-insulator based micro check valve," *Journal of micromechanics and microengineering*, vol. 14, p. 382, 2003.

- [112] D. Accoto, M. Carrozza, and P. Dario, "Modelling of micropumps using unimorph piezoelectric actuator and ball valves," *Journal of Micromechanics and Microengineering*, vol. 10, p. 277, 2000.
- [113] C. Yamahata, F. Lacharme, Y. Burri, and M. A. Gijs, "A ball valve micropump in glass fabricated by powder blasting," *Sensors and Actuators B: Chemical*, vol. 110, pp. 1-7, 2005.
- [114] E. F. Hasselbrink, T. J. Shepodd, and J. E. Rehm, "High-pressure microfluidic control in lab-on-a-chip devices using mobile polymer monoliths," *Analytical Chemistry*, vol. 74, pp. 4913-4918, 2002.
- [115] D. S. Reichmuth, T. J. Shepodd, and B. J. Kirby, "On-chip high-pressure picoliter injector for pressure-driven flow through porous media," *Analytical chemistry*, vol. 76, pp. 5063-5068, 2004.
- [116] J.-W. Choi, K. W. Oh, A. Han, C. A. Wijayawardhana, C. Lannes, S. Bhansali, *et al.*, "Development and characterization of microfluidic devices and systems for magnetic bead-based biochemical detection," *Biomedical Microdevices*, vol. 3, pp. 191-200, 2001.
- [117] B. Bae, N. Kim, H. Kee, S.-H. Kim, Y. Lee, S. Lee, *et al.*, "Feasibility test of an electromagnetically driven valve actuator for glaucoma treatment," *Microelectromechanical Systems, Journal of*, vol. 11, pp. 344-354, 2002.
- [118] C. Fu, Z. Rummeler, and W. Schomburg, "Magnetically driven micro ball valves fabricated by multilayer adhesive film bonding," *Journal of Micromechanics and microengineering*, vol. 13, p. S96, 2003.
- [119] C. Goll, W. Bacher, B. Büstgens, D. Maas, R. Ruprecht, and W. Schomburg, "An electrostatically actuated polymer microvalve equipped with a movable membrane electrode," *Journal of Micromechanics and Microengineering*, vol. 7, p. 224, 1997.

- [120] W. van der Wijngaart, H. Ask, P. Enoksson, and G. Stemme, "A high-stroke, high-pressure electrostatic actuator for valve applications," *Sensors and Actuators A: Physical*, vol. 100, pp. 264-271, 2002.
- [121] X. e. Yang, A. Hölke, S. A. Jacobson, J. H. Lang, M. A. Schmidt, and S. D. Umans, "An electrostatic, on/off microvalve designed for gas fuel delivery for the MIT microengine," *Microelectromechanical Systems, Journal of*, vol. 13, pp. 660-668, 2004.
- [122] H. Li, D. Roberts, J. Steyn, K. Turner, O. Yaglioglu, N. Hagood, *et al.*, "Fabrication of a high frequency piezoelectric microvalve," *Sensors and Actuators A: Physical*, vol. 111, pp. 51-56, 2004.
- [123] T. Goettsche, J. Kohnle, M. Willmann, H. Ernst, S. Spieth, R. Tischler, *et al.*, "Novel approaches to particle tolerant valves for use in drug delivery systems," *Sensors and Actuators A: Physical*, vol. 118, pp. 70-77, 2005.
- [124] M. Kohl, K. Skrobanek, and S. Miyazaki, "Development of stress-optimised shape memory microvalves," *Sensors and Actuators A: Physical*, vol. 72, pp. 243-250, 1999.
- [125] C. A. Rich and K. D. Wise, "A high-flow thermopneumatic microvalve with improved efficiency and integrated state sensing," *Microelectromechanical Systems, Journal of*, vol. 12, pp. 201-208, 2003.
- [126] C. Goll, W. Bacher, B. Büstgens, D. Maas, W. Menz, and W. Schomburg, "Microvalves with bistable buckled polymer diaphragms," *Journal of Micromechanics and Microengineering*, vol. 6, p. 77, 1996.
- [127] W. Schomburg and C. Goll, "Design optimization of bistable microdiaphragm valves," *Sensors and Actuators A: Physical*, vol. 64, pp. 259-264, 1998.
- [128] K. Yoshida, M. Kikuchi, J.-H. Park, and S. Yokota, "Fabrication of micro electro-

- rheological valves (ER valves) by micromachining and experiments," *Sensors and Actuators A: Physical*, vol. 95, pp. 227-233, 2002.
- [129] C. Neagu, J. Gardeniers, M. Elwenspoek, and J. Kelly, "An electrochemical active valve," *Electrochimica Acta*, vol. 42, pp. 3367-3373, 1997.
- [130] H. Suzuki and R. Yoneyama, "Integrated microfluidic system with electrochemically actuated on-chip pumps and valves," *Sensors and Actuators B: Chemical*, vol. 96, pp. 38-45, 2003.
- [131] T. Miyata, N. Asami, and T. Uragami, "A reversibly antigen-responsive hydrogel," *Nature*, vol. 399, pp. 766-769, 1999.
- [132] D. J. Beebe, J. S. Moore, J. M. Bauer, Q. Yu, R. H. Liu, C. Devadoss, *et al.*, "Functional hydrogel structures for autonomous flow control inside microfluidic channels," *Nature*, vol. 404, pp. 588-590, 2000.
- [133] R. H. Liu, Q. Yu, and D. J. Beebe, "Fabrication and characterization of hydrogel-based microvalves," *Microelectromechanical Systems, Journal of*, vol. 11, pp. 45-53, 2002.
- [134] A. Richter, S. Howitz, D. Kuckling, and K.-F. Arndt, "Influence of volume phase transition phenomena on the behavior of hydrogel-based valves," *Sensors and Actuators B: Chemical*, vol. 99, pp. 451-458, 2004.
- [135] K. Tashiro, S. Ikeda, T. Sekiguchi, S. Shoji, H. Makazu, T. Funatsu, *et al.*, "A particles and biomolecules sorting micro flow system using thermal gelation of methyl cellulose solution," in *Micro Total Analysis Systems 2001*, 2001, pp. 471-473.
- [136] Y. Liu, C. B. Rauch, R. L. Stevens, R. Lenigk, J. Yang, D. B. Rhine, *et al.*, "DNA amplification and hybridization assays in integrated plastic monolithic devices," *Analytical Chemistry*, vol. 74, pp. 3063-3070, 2002.

- [137] E. T. Carlen and C. H. Mastrangelo, "Surface micromachined paraffin-actuated microvalve," *Microelectromechanical Systems, Journal of*, vol. 11, pp. 408-420, 2002.
- [138] L. Klintberg, M. Karlsson, L. Stenmark, and G. Thornell, "A thermally activated paraffin-based actuator for gas-flow control in a satellite electrical propulsion system," *Sensors and Actuators A: Physical*, vol. 105, pp. 237-246, 2003.
- [139] R. Pal, M. Yang, B. N. Johnson, D. T. Burke, and M. A. Burns, "Phase change microvalve for integrated devices," *Analytical chemistry*, vol. 76, pp. 3740-3748, 2004.
- [140] R. H. Liu, J. Bonanno, J. Yang, R. Lenigk, and P. Grodzinski, "Single-use, thermally actuated paraffin valves for microfluidic applications," *Sensors and Actuators B: Chemical*, vol. 98, pp. 328-336, 2004.
- [141] L. Gui and J. Liu, "Ice valve for a mini/micro flow channel," *Journal of Micromechanics and Microengineering*, vol. 14, p. 242, 2004.
- [142] M. Matsuguchi, N. Harada, and S. Omori, "Poly (N-isopropylacrylamide) nanoparticles for QCM-based gas sensing of HCl," *Sensors and Actuators B: Chemical*, vol. 190, pp. 446-450, 2014.
- [143] R. E. Rivero, M. A. Molina, C. R. Rivarola, and C. A. Barbero, "Pressure and microwave sensors/actuators based on smart hydrogel/conductive polymer nanocomposite," *Sensors and Actuators B: Chemical*, vol. 190, pp. 270-278, 2014.
- [144] A. M. Mihut, A. P. Dabkowska, J. J. Crassous, P. Schurtenberger, and T. Nylander, "Tunable Adsorption of Soft Colloids on Model Biomembranes," *ACS nano*, vol. 7, pp. 10752-10763, 2013.
- [145] C. D. Sorrell, M. C. Carter, and M. J. Serpe, "Color Tunable Poly (N-Isopropylacrylamide)-co-Acrylic Acid Microgel-Au Hybrid Assemblies," *Advanced*

- Functional Materials*, vol. 21, pp. 425-433, 2011.
- [146] T. Karir, H. D. Sarma, G. Samuel, P. A. Hassan, D. Padmanabhan, and M. Venkatesh, "Preparation and evaluation of radioiodinated thermoresponsive polymer based on poly (N - isopropyl acrylamide) for radiotherapy," *Journal of Applied Polymer Science*, vol. 130, pp. 860-868, 2013.
- [147] C. D. Jones, M. J. Serpe, L. Schroeder, and L. A. Lyon, "Microlens formation in microgel/gold colloid composite materials via photothermal patterning," *Journal of the American Chemical Society*, vol. 125, pp. 5292-5293, 2003.
- [148] M. E. Nash, D. Healy, W. M. Carroll, C. Elvira, and Y. A. Rochev, "Cell and cell sheet recovery from pNIPAm coatings; motivation and history to present day approaches," *Journal of Materials Chemistry*, vol. 22, pp. 19376-19389, 2012.
- [149] M. Peroglio, D. Eglin, L. M. Benneker, M. Alini, and S. Grad, "Thermoreversible hyaluronan-based hydrogel supports in vitro and ex vivo disc-like differentiation of human mesenchymal stem cells," *The Spine Journal*, vol. 13, pp. 1627-1639, 2013.
- [150] D. Liu, T. Wang, X. Liu, and Z. Tong, "Cell Proliferation and cell sheet detachment from the positively and negatively charged nanocomposite hydrogels," *Biopolymers*, vol. 101, pp. 58-65, 2014.
- [151] Y. Pan, H. Bao, N. G. Sahoo, T. Wu, and L. Li, "Water-Soluble Poly (N-isopropylacrylamide)-Graphene Sheets Synthesized via Click Chemistry for Drug Delivery," *Advanced Functional Materials*, vol. 21, pp. 2754-2763, 2011.
- [152] G.-H. Hsiue, S.-h. Hsu, C.-C. Yang, S.-H. Lee, and I.-K. Yang, "Preparation of controlled release ophthalmic drops, for glaucoma therapy using thermosensitive poly-N-isopropylacrylamide," *Biomaterials*, vol. 23, pp. 457-462, 2002.
- [153] G.-H. Hsiue, R.-W. Chang, C.-H. Wang, and S.-H. Lee, "Development of in situ thermosensitive drug vehicles for glaucoma therapy," *Biomaterials*, vol. 24, pp. 2423-

- 2430, 2003.
- [154] C. de las Heras Alarcón, S. Pennadam, and C. Alexander, "Stimuli responsive polymers for biomedical applications," *Chemical Society Reviews*, vol. 34, pp. 276-285, 2005.
- [155] M. W. Baker and R. Sarpeshkar, "Feedback analysis and design of RF power links for low-power bionic systems," *Biomedical Circuits and Systems, IEEE Transactions on*, vol. 1, pp. 28-38, 2007.
- [156] A. P. Sample, D. A. Meyer, and J. R. Smith, "Analysis, experimental results, and range adaptation of magnetically coupled resonators for wireless power transfer," *Industrial Electronics, IEEE Transactions on*, vol. 58, pp. 544-554, 2011.
- [157] L. Rindorf, L. Lading, and O. Breinbjerg, "Resonantly coupled antennas for passive sensors," in *Sensors, 2008 IEEE*, 2008, pp. 1611-1614.
- [158] M. Catrysse, B. Hermans, and R. Puers, "An inductive power system with integrated bi-directional data-transmission," *Sensors and Actuators A: Physical*, vol. 115, pp. 221-229, 2004.
- [159] K. Jung, Y. H. Kim, J.-H. Kim, and Y. J. Kim, "Wireless power transmission for implantable devices using inductive component of closed magnetic circuit," *Electronics Letters*, vol. 45, pp. 21-22, 2009.
- [160] A. Kurs, A. Karalis, R. Moffatt, J. D. Joannopoulos, P. Fisher, and M. Soljačić, "Wireless power transfer via strongly coupled magnetic resonances," *science*, vol. 317, pp. 83-86, 2007.
- [161] A. Karalis, J. D. Joannopoulos, and M. Soljačić, "Efficient wireless non-radiative mid-range energy transfer," *Annals of Physics*, vol. 323, pp. 34-48, 2008.
- [162] R.-F. Xue, K.-W. Cheng, and M. Je, "High-efficiency wireless power transfer for

- biomedical implants by optimal resonant load transformation," *Circuits and Systems I: Regular Papers, IEEE Transactions on*, vol. 60, pp. 867-874, 2013.
- [163] Z. Yang, W. Liu, and E. Basham, "Inductor modeling in wireless links for implantable electronics," *Magnetics, IEEE Transactions on*, vol. 43, pp. 3851-3860, 2007.
- [164] M. Kiani, U.-M. Jow, and M. Ghovanloo, "Design and optimization of a 3-coil inductive link for efficient wireless power transmission," *Biomedical Circuits and Systems, IEEE Transactions on*, vol. 5, pp. 579-591, 2011.
- [165] U.-M. Jow and M. Ghovanloo, "Design and optimization of printed spiral coils for efficient transcutaneous inductive power transmission," *Biomedical Circuits and Systems, IEEE Transactions on*, vol. 1, pp. 193-202, 2007.
- [166] S. Vaddiraju, I. Tomazos, D. J. Burgess, F. C. Jain, and F. Papadimitrakopoulos, "Emerging synergy between nanotechnology and implantable biosensors: a review," *Biosensors and Bioelectronics*, vol. 25, pp. 1553-1565, 2010.
- [167] N. Wisniewski, F. Moussy, and W. Reichert, "Characterization of implantable biosensor membrane biofouling," *Fresenius' journal of analytical chemistry*, vol. 366, pp. 611-621, 2000.
- [168] N. Wisniewski, B. Klitzman, B. Miller, and W. Reichert, "Decreased analyte transport through implanted membranes: differentiation of biofouling from tissue effects," *Journal of biomedical materials research*, vol. 57, pp. 513-521, 2001.
- [169] R. Gifford, J. J. Kehoe, S. L. Barnes, B. A. Kornilayev, M. A. Alterman, and G. S. Wilson, "Protein interactions with subcutaneously implanted biosensors," *Biomaterials*, vol. 27, pp. 2587-2598, 2006.
- [170] Y. Onuki, U. Bhardwaj, F. Papadimitrakopoulos, and D. J. Burgess, "A review of the biocompatibility of implantable devices: current challenges to overcome foreign body response," *Journal of diabetes science and technology*, vol. 2, pp. 1003-1015, 2008.

- [171] M. Frost and M. E. Meyerhoff, "In vivo chemical sensors: tackling biocompatibility," *Analytical chemistry*, vol. 78, pp. 7370-7377, 2006.
- [172] U. Bhardwaj, F. Papadimitrakopoulos, and D. J. Burgess, "A review of the development of a vehicle for localized and controlled drug delivery for implantable biosensors," *Journal of diabetes science and technology*, vol. 2, pp. 1016-1029, 2008.
- [173] T. Hickey, D. Kreutzer, D. Burgess, and F. Moussy, "Dexamethasone/PLGA microspheres for continuous delivery of an anti-inflammatory drug for implantable medical devices," *Biomaterials*, vol. 23, pp. 1649-1656, 2002.
- [174] T. Hickey, D. Kreutzer, D. Burgess, and F. Moussy, "In vivo evaluation of a dexamethasone/PLGA microsphere system designed to suppress the inflammatory tissue response to implantable medical devices," *Journal of biomedical materials research*, vol. 61, pp. 180-187, 2002.
- [175] U. Bhardwaj, R. Sura, F. Papadimitrakopoulos, and D. J. Burgess, "Controlling acute inflammation with fast releasing dexamethasone-PLGA microsphere/PVA hydrogel composites for implantable devices," *Journal of diabetes science and technology*, vol. 1, pp. 8-17, 2007.
- [176] L. Norton, H. Koschwanetz, N. Wisniewski, B. Klitzman, and W. Reichert, "Vascular endothelial growth factor and dexamethasone release from nonfouling sensor coatings affect the foreign body response," *Journal of biomedical materials research Part A*, vol. 81, pp. 858-869, 2007.
- [177] S. D. Patil, F. Papadimitrakopoulos, and D. J. Burgess, "Concurrent delivery of dexamethasone and VEGF for localized inflammation control and angiogenesis," *Journal of Controlled Release*, vol. 117, pp. 68-79, 2007.
- [178] M. C. Frost, S. M. Rudich, H. Zhang, M. A. Maraschio, and M. E. Meyerhoff, "In vivo biocompatibility and analytical performance of intravascular amperometric

- oxygen sensors prepared with improved nitric oxide-releasing silicone rubber coating," *Analytical chemistry*, vol. 74, pp. 5942-5947, 2002.
- [179] F. Moussy, D. J. Harrison, D. W. O'Brien, and R. V. Rajotte, "Performance of subcutaneously implanted needle-type glucose sensors employing a novel trilayer coating," *Analytical Chemistry*, vol. 65, pp. 2072-2077, 1993.
- [180] I. Galeska, D. Chattopadhyay, F. Moussy, and F. Papadimitrakopoulos, "Calcification-resistant Nafion/Fe³⁺ assemblies for implantable biosensors," *Biomacromolecules*, vol. 1, pp. 202-207, 2000.
- [181] S. S. Praveen, R. Hanumantha, J. M. Belovich, and B. L. Davis, "Novel hyaluronic acid coating for potential use in glucose sensor design," *Diabetes technology & therapeutics*, vol. 5, pp. 393-399, 2003.
- [182] R. Tipnis, S. Vaddiraju, F. Jain, D. J. Burgess, and F. Papadimitrakopoulos, "Layer-by-layer assembled semipermeable membrane for amperometric glucose sensors," *Journal of diabetes science and technology*, vol. 1, pp. 193-200, 2007.
- [183] Y. Yang, S. Zhang, M. Kingston, G. Jones, G. Wright, and S. Spencer, "Glucose sensor with improved haemocompatibility," *Biosensors and Bioelectronics*, vol. 15, pp. 221-227, 2000.
- [184] K. Rege, N. R. Raravikar, D.-Y. Kim, L. S. Schadler, P. M. Ajayan, and J. S. Dordick, "Enzyme-polymer-single walled carbon nanotube composites as biocatalytic films," *Nano Letters*, vol. 3, pp. 829-832, 2003.
- [185] P. Asuri, S. S. Karajanagi, R. S. Kane, and J. S. Dordick, "Polymer-nanotube-enzyme composites as active antifouling films," *Small*, vol. 3, pp. 50-53, 2007.
- [186] H. R. Luckarift, M. B. Dickerson, K. H. Sandhage, and J. C. Spain, "Rapid, Room-Temperature Synthesis of Antibacterial Bionanocomposites of Lysozyme with Amorphous Silica or Titania," *Small*, vol. 2, pp. 640-643, 2006.

- [187] E. Gultepe, D. Nagesha, S. Sridhar, and M. Amiji, "Nanoporous inorganic membranes or coatings for sustained drug delivery in implantable devices," *Advanced drug delivery reviews*, vol. 62, pp. 305-315, 2010.
- [188] G. Voskerician, M. S. Shive, R. S. Shawgo, H. Von Recum, J. M. Anderson, M. J. Cima, *et al.*, "Biocompatibility and biofouling of MEMS drug delivery devices," *Biomaterials*, vol. 24, pp. 1959-1967, 2003.
- [189] K. Scholten and E. Meng, "Materials for microfabricated implantable devices: a review," *Lab on a Chip*, vol. 15, pp. 4256-4272, 2015.
- [190] C. Belmont and H. Girault, "Coplanar interdigitated band electrodes for synthesis Part I: Ohmic loss evaluation," *Journal of applied electrochemistry*, vol. 24, pp. 475-480, 1994.
- [191] E. Meng, P.-Y. Li, and Y.-C. Tai, "A biocompatible Parylene thermal flow sensing array," *Sensors and Actuators A: Physical*, vol. 144, pp. 18-28, 2008.
- [192] Z. Dai and H. Möhwald, "Highly Stable and Biocompatible Nafion-Based Capsules with Controlled Permeability for Low-Molecular-Weight Species," *Chemistry-A European Journal*, vol. 8, pp. 4751-4755, 2002.
- [193] M. Schalenbach, T. Hoefner, P. Paciok, M. Carmo, W. Lueke, and D. Stolten, "Gas Permeation through Nafion. Part 1: Measurements," *The Journal of Physical Chemistry C*, vol. 119, pp. 25145-25155, 2015.
- [194] M. Schalenbach, M. A. Hoeh, J. T. Gostick, W. Lueke, and D. Stolten, "Gas Permeation through Nafion. Part 2: Resistor Network Model," *The Journal of Physical Chemistry C*, vol. 119, pp. 25156-25169, 2015.
- [195] J. Maruyama, M. Inaba, K. Katakura, Z. Ogumi, and Z.-i. Takehara, "Influence of Nafion® film on the kinetics of anodic hydrogen oxidation," *Journal of Electroanalytical Chemistry*, vol. 447, pp. 201-209, 1998.

- [196] H. Kim, M.-S. Kang, D. H. Lee, J. Won, J. Kim, and Y. S. Kang, "Proton exchange membranes with high cell performance based on Nafion/poly (p-phenylene vinylene) composite polymer electrolyte," *Journal of Membrane Science*, vol. 304, pp. 60-64, 2007.
- [197] J. Xie, Y. Miao, J. Shih, Q. He, J. Liu, Y.-C. Tai, *et al.*, "An electrochemical pumping system for on-chip gradient generation," *Analytical Chemistry*, vol. 76, pp. 3756-3763, 2004.
- [198] R. W. Coughlin and M. Farooque, "Hydrogen production from coal, water and electrons," 1979.
- [199] P. Dubey, A. Sinha, S. Talapatra, N. Koratkar, P. Ajayan, and O. Srivastava, "Hydrogen generation by water electrolysis using carbon nanotube anode," *international journal of hydrogen energy*, vol. 35, pp. 3945-3950, 2010.
- [200] B. C. Ewan and O. D. Adeniyi, "A demonstration of carbon-assisted water electrolysis," *Energies*, vol. 6, pp. 1657-1668, 2013.
- [201] C. R. Ethier, M. Johnson, and J. Ruberti, "Ocular biomechanics and biotransport," *Annu. Rev. Biomed. Eng.*, vol. 6, pp. 249-273, 2004.
- [202] G. J. Jaffe, R. M. McCallum, B. Branchaud, C. Skalak, Z. Butuner, and P. Ashton, "Long-term follow-up results of a pilot trial of a fluocinolone acetonide implant to treat posterior uveitis," *Ophthalmology*, vol. 112, pp. 1192-1198. e1, 2005.
- [203] J. R. Gebhard and D. Patel, "Taxane compounds for treating eye disease," ed: Google Patents, 2009.
- [204] Y. Hirokawa and T. Tanaka, "Volume phase transition in a nonionic gel," *The Journal of chemical physics*, vol. 81, pp. 6379-6380, 1984.
- [205] J. W. Kim, A. S. Utada, A. Fernández - Nieves, Z. Hu, and D. A. Weitz, "Fabrication

- of monodisperse gel shells and functional microgels in microfluidic devices," *Angewandte Chemie*, vol. 119, pp. 1851-1854, 2007.
- [206] J. B. Goodenough, "Summary of losses in magnetic materials," *IEEE Transactions on magnetics*, vol. 38, pp. 3398-3408, 2002.
- [207] R. Wojda and M. K. Kazimierczuk, "Winding resistance of litz-wire and multi-strand inductors," *Power Electronics, IET*, vol. 5, pp. 257-268, 2012.
- [208] M. Bartoli, N. Noferi, A. Reatti, and M. K. Kazimierczuk, "Modeling litz-wire winding losses in high-frequency power inductors," in *Power Electronics Specialists Conference, 1996. PESC'96 Record., 27th Annual IEEE, 1996*, pp. 1690-1696.
- [209] G. Grandi, M. K. Kazimierczuk, A. Massarini, and U. Reggiani, "Stray capacitances of single-layer solenoid air-core inductors," *Industry Applications, IEEE Transactions on*, vol. 35, pp. 1162-1168, 1999.
- [210] Q. Yu and T. W. Holmes, "A study on stray capacitance modeling of inductors by using the finite element method," *Electromagnetic Compatibility, IEEE Transactions on*, vol. 43, pp. 88-93, 2001.
- [211] A. Massarini, M. Kazimierczuk, and G. Grandi, "Lumped parameter models for single-and multiple-layer inductors," in *Power Electronics Specialists Conference, 1996. PESC'96 Record., 27th Annual IEEE, 1996*, pp. 295-301.
- [212] C. M. Zierhofer and E. S. Hochmair, "Geometric approach for coupling enhancement of magnetically coupled coils," *Biomedical Engineering, IEEE Transactions on*, vol. 43, pp. 708-714, 1996.
- [213] A. Massarini and M. K. Kazimierczuk, "Self-capacitance of inductors," *Power Electronics, IEEE Transactions on*, vol. 12, pp. 671-676, 1997.
- [214] N. d. N. Donaldson and T. Perkins, "Analysis of resonant coupled coils in the design

- of radio frequency transcutaneous links," *Medical and Biological Engineering and computing*, vol. 21, pp. 612-627, 1983.
- [215] K. Finkelzeller, "The RFID handbook," ed: John Wiley & Sons, 2003.
- [216] D. J. H. Tng, P. Song, R. Hu, C. Yang, and K. T. Yong, "High reliability nanosandwiched Pt/Ti multilayer electrode actuators for on-chip biomedical applications," *Analyst*, vol. 139, pp. 407-415, 2014.
- [217] H. F. A. Verhaart, R. M. De Jonge, and S. J. D. Van Stralen, "Growth rate of a gas bubble during electrolysis in supersaturated liquid," *Int. J. Heat Mass Transf.*, vol. 23, no. 3, pp. 293–299, Mar. 1980.
- [218] S. Shibata, "Supersaturation of oxygen in acidic solution in the vicinity of an oxygen-evolving platinum anode," *Electrochim. Acta*, vol. 23, no. 7, pp. 619–623, Jul. 1978.
- [219] C.W. M. P. Sillen, E. Barendrecht, L. J. J. Janssen, and S. J. D. van Stralen, "Gas bubble behaviour during water electrolysis," *Int. J. Hydrogen Energy*, vol. 7, no. 7, pp. 577–587, 1982.